Acta Numerica (2025), pp. 385–489
doi:10.1017/S0962492924000072

Time parallelization for hyperbolic and parabolic problems

Martin J. Gander
Department of Mathematics,
University of Geneva, CP64, 1211 Geneva 4, Switzerland
E-mail: martin.gander@unige.ch

Shu-Lin Wu*
School of Mathematics and Statistics,
Northeast Normal University, Changchun 130024, China
E-mail: wushulin84@hotmail.com

Tao Zhou
Institute of Computational Mathematics and
Scientific/Engineering Computing, Academy of Mathematics and Systems Science,
Chinese Academy of Sciences, China
E-mail: tzhou@lsec.cc.ac.cn

Time parallelization, also known as PinT (parallel-in-time), is a new research direction for the development of algorithms used for solving very large-scale evolution problems on highly parallel computing architectures. Despite the fact that interesting theoretical work on PinT appeared as early as 1964, it was not until 2004, when processor clock speeds reached their physical limit, that research in PinT took off. A distinctive characteristic of parallelization in time is that information flow only goes forward in time, meaning that time evolution processes seem necessarily to be sequential. Nevertheless, many algorithms have been developed for PinT computations over the past two decades, and they are often grouped into four basic classes according to how the techniques work and are used: shooting-type methods; waveform relaxation methods based on domain decomposition; multigrid methods in space–time; and direct time parallel methods. However, over the past few years, it has been recognized that highly successful PinT algorithms for parabolic problems struggle when applied to hyperbolic problems. We will therefore focus on this important aspect, first by providing a summary of the fundamental differences between parabolic and hyperbolic problems for time parallelization. We then group PinT algorithms into two basic groups. The first group contains four effective

* Corresponding author

PinT techniques for hyperbolic problems: Schwarz waveform relaxation (SWR) with its relation to tent pitching; parallel integral deferred correction; ParaExp; and ParaDiag. While the methods in the first group also work well for parabolic problems, we then present PinT methods specifically designed for parabolic problems in the second group: Parareal; the parallel full approximation scheme in space–time (PFASST); multigrid reduction in time (MGRiT); and space–time multigrid (STMG). We complement our analysis with numerical illustrations using four time-dependent PDEs: the heat equation; the advection–diffusion equation; Burgers' equation; and the second-order wave equation.

2020 Mathematics Subject Classification: Primary 65M55, 65M12, 65M15, 65Y05
Secondary 65M06, 65L10

CONTENTS

1 Introduction 386
2 Model problems linking the parabolic and hyperbolic world 388
3 Effective PinT methods for hyperbolic problems 396
4 PinT methods designed for parabolic problems 443
5 Conclusions 481
References 481

1. Introduction

Time parallelization has been a very active field of research over the past two decades. The reason for this is that hardware development has reached its physical limit for clock speed, and faster computation is only possible using ever more cores. We see this development even in small-scale computing devices, such as smartphones, that have become multicore, and high-performance computers now have millions of cores. Time parallelization methods, also referred to as parallel-in-time (PinT) methods, are methods that allow us to use more cores for evolution than if we were only to parallelize in space. Sixty years ago, in a visionary paper, Nievergelt (1964, p. 733) proposed such an approach, concluding with:

> The integration methods introduced in this paper are to be regarded as tentative examples of a much wider class of numerical procedures in which parallelism is introduced at the expense of redundancy of computation. As such, their merits lie not so much in their usefulness as numerical algorithms as in their potential as prototypes of better methods based on the same principle. It is believed that more general and improved versions of these methods will be of great importance when computers capable of executing many computations in parallel become available.

Several new methods like these were then developed over the decades that followed Nievergelt, until PinT methods were brought to the forefront of research with

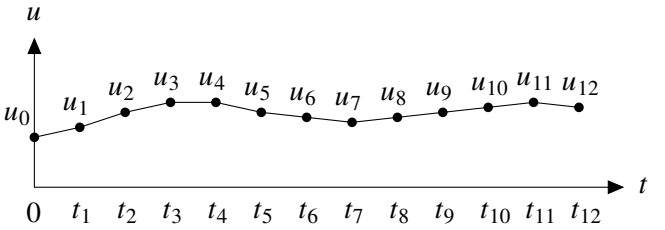

Figure 1.1. Sequential nature of time integration using forward Euler.

the advent of the Parareal algorithm (Lions, Maday and Turinici 2001); see the historical review by Gander (2015), the review focusing on PinT applications by Ong and Schröder (2020), and also the recent research monograph by Gander and Lunet (2024).

Parallelization in time for evolution problems may, at first glance, seem impossible due to the causality principle: solutions at later times are determined by solutions at earlier times, and not vice versa. Evolution problems thus have an inherent sequential nature. This becomes clear when we consider a simple ordinary differential equation as our evolution problem, along with its forward Euler discretization,

$$\partial_t u = f(u), \quad u(0) = u_0, \quad u_{n+1} = u_n + \Delta t f(u_n). \tag{1.1}$$

The recurrence formula of forward Euler clearly shows that we must know u_n before we can compute u_{n+1}, as illustrated in Figure 1.1. It is not clear, for example, if we can do useful computational work for the approximations u_{10} to u_{12} before knowing the approximation u_9.

Nevertheless, many new PinT methods have been developed since 2001, and they are often classified into the following four groups based on the algorithmic techniques used. See Gander (2015) and the recent research monograph by Gander and Lunet (2024); we give more complete references later in the article.

(1) Methods based on *multiple shooting* going back to the work of Nievergelt (1964), Bellen and Zennaro (1989) and Chartier and Philippe (1993), leading to Saha, Stadel and Tremaine (1997) and culminating in the *Parareal* algorithm (Lions *et al.* 2001) and many variants.

(2) Methods based on *domain decomposition* (Schwarz 1870) and *waveform relaxation* (Lelarasmee, Ruehli and Sangiovanni-Vincentelli 1982) that were combined in Bjørhus (1995), resulting in *Schwarz waveform relaxation* (SWR) (Gander, Halpern and Nataf 1999).

(3) Methods based on *multigrid* going back to the parabolic multigrid method (Hackbusch 1984), and developed into fully parallel *space–time multigrid* (STMG) methods (Gander and Neumüller 2016).

(4) *Direct time-parallel methods*, which started with parallel time-stepping techniques (Miranker and Liniger 1967) and led to the modern *revisionist integral deferred correction* (RIDC) method (Christlieb, Macdonald and Ong 2010). Currently very successful methods in this class are *ParaExp* (Gander and Güttel 2013), and parallelization by diagonalization (Maday and Rønquist 2008), which led to *ParaDiag* (Gander *et al.* 2021*c*).

The first three groups contain iterative methods whereas the last one contains non-iterative methods, but the boundaries in this classification are not strict. A good example is that of the ParaDiag methods, which were at first exclusively direct solvers based on the diagonalization of the time-stepping matrix, but then iterative variants rapidly appeared, within WR methods from the second group (Gander and Wu 2019) or within Parareal from the first group (Gander and Wu 2020). Approximate ParaDiag methods were also used as stationary iterations or preconditioners for Krylov methods, applied directly to the all-at-once system derived from the space–time discretization in the third group (McDonald, Pestana and Wathen 2018, Liu and Wu 2020). Parareal from the first group can also be interpreted as a multigrid method from the third group with aggressive coarsening (Gander and Vandewalle 2007), and in turn MGRiT as a Parareal algorithm with overlap (Gander, Kwok and Zhang 2018*b*).

Here, however, we would like to adopt a different approach to classifying PinT methods, specifically based on the types of problems that they can effectively solve:

(1) effective PinT methods for hyperbolic problems,

(2) PinT methods designed for parabolic problems.

To achieve this, in Section 2 we explain intuitively why there must be a fundamental distinction in PinT methods when solving hyperbolic or parabolic problems, and we introduce model problems that will later serve to illustrate this for PinT methods. Then, in Section 3, we describe effective PinT methods for hyperbolic problems, which generally work even better for parabolic problems, and in Section 4 we present PinT methods designed for parabolic problems, which generally struggle when applied to hyperbolic problems. We will draw conclusions in Section 5. The MATLAB codes for the numerical results in Sections 2–4 can be obtained from https://github.com/wushulin/ActaPinT.

2. Model problems linking the parabolic and hyperbolic world

Our test problems will often be partial differential equations (PDEs) that allow us to link the parabolic and hyperbolic worlds. A typical example is the linear advection–diffusion equation we will first see in Section 2.2, which contains both parabolic and hyperbolic components. We will also frequently use the system of

ordinary differential equations (ODEs)

$$\begin{aligned} \boldsymbol{u}'(t) &= A\boldsymbol{u}(t) + \boldsymbol{g}(t), \quad t \in (0,T], \\ \boldsymbol{u}(0) &= \boldsymbol{u}_0, \end{aligned} \tag{2.1}$$

where $A \in \mathbb{R}^{N_x \times N_x}$ is the discrete matrix arising from semi-discretizing the PDE in space, because many time-parallel methods (except the domain decomposition based methods) are described and analysed for ODEs. An important nonlinear PDE variant of advection–diffusion is the so-called Burgers' equation, which we will first see in Section 2.3. Similarly to the linear case, in order to discuss time-parallel methods in the nonlinear setting we will use the nonlinear system of ODEs

$$\begin{aligned} \boldsymbol{u}'(t) &= f(\boldsymbol{u}(t), t), \quad t \in (0,T], \\ \boldsymbol{u}(0) &= \boldsymbol{u}_0, \end{aligned} \tag{2.2}$$

where $f : \mathbb{R}^{N_x} \times \mathbb{R} \to \mathbb{R}^{N_x}$ depends on its first variable in a nonlinear manner, such as $f(\boldsymbol{u}(t), t) = A\boldsymbol{u}(t) + B\boldsymbol{u}^2(t) + \boldsymbol{g}(t)$ for Burgers' equation.

However, we also introduce simpler equations that are of either parabolic or hyperbolic nature, such as the heat equation and the second-order wave equation. To avoid complicated notation, we will only consider model problems in one spatial dimension on the unit interval $\Omega = (0, 1)$. This is not really a restriction, since the applicability and convergence properties of PinT methods do not generally depend on the space dimension.

2.1. Heat equation

Our parabolic model problem will be the one-dimensional heat equation

$$\partial_t u(x,t) = \partial_{xx} u(x,t) + g(x,t) \quad \text{in } \Omega \times (0,T], \tag{2.3}$$

with initial value $u(x, 0) = u_0(x)$, and either homogeneous Dirichlet or Neumann boundary conditions. An example solution with $u_0(x) = 0$ and a forcing function that heats at four different time instances $t_1 = 0.1, t_2 = 0.6, t_3 = 1.35$ and $t_4 = 1.85$ in the middle of the space domain $\Omega = (0, 1)$,

$$g(x,t) = 10 \sum_{j=1}^{4} \exp(-\sigma[(t - t_j)^2 + (x - 0.5)^2]), \tag{2.4}$$

is shown for $\sigma = 200$ in Figure 2.1(a–c), for homogeneous Dirichlet, Neumann and periodic boundary conditions. We observe that with Dirichlet conditions the solution does not propagate far in time, and thus we can compute, for example, the solution for $t \in (1.7, 2.2)$ for the fourth source term independently from the solution at earlier times! This is a prime example where, despite the causality principle, we can perform useful computations for later time instances before knowing the earlier ones. This concept can be naturally understood from daily life experience: it is straightforward to predict the temperature in your living room in winter a week

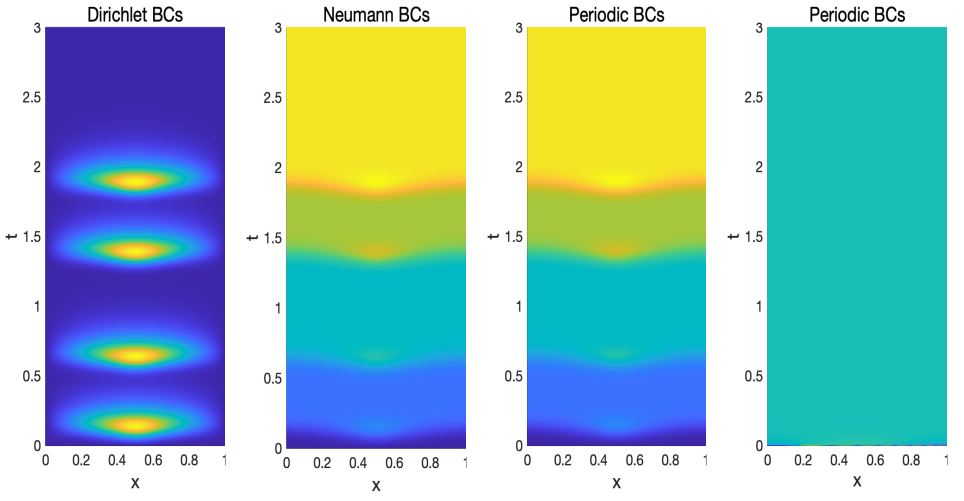

Figure 2.1. Heat equation with homogeneous Dirichlet (a), Neumann (b) and periodic boundary conditions (c), using the source term (2.4) and zero initial condition $u_0(x) = 0$. In (d) we still use periodic boundary conditions but a zero source term, with initial condition $u_0(x) = \sin^2(8\pi(1-x)^2)$.

or a month in advance; you simply need to know if the heater will be on and the windows closed.

However, this changes significantly in our simple model problem when Neumann conditions are applied, as shown in Figure 2.1(b). Here the solution for $t \in (1.7, 2.2)$ is influenced by the first, second and third source terms at earlier times, since heat is now accumulating, nicely illustrating the causality principle. This scenario corresponds to a perfectly insulated room where heat cannot escape, and in this situation it is crucial to know how frequently or for how long the heating was on, since this heat will stay forever in the perfectly insulated room. Note, however, that in practice it is difficult to have a perfectly insulated room, and heat will always eventually escape, which one would model with a Robin boundary condition.

The situation in Figure 2.1(c) with periodic boundary conditions is similar to the case with Neumann boundary conditions in Figure 2.1(b); the solution for $t \in (1.7, 2.2)$ is also influenced by the first, second and third source terms at earlier times, and with periodic conditions, heat can never escape.

In Figure 2.1(d) we show a solution with zero source term and periodic boundary conditions, but now imposing an initial condition with a precise, oscillating signal, namely $u_0(x) = \sin^2(8\pi(1-x)^2)$. We see that the only information left from this signal after a very short time is already a constant, about the same constant as from the first two source terms in Figure 2.1(b,c).

In spite of the causality principle, time parallelization and thus PinT computations for a heat equation, and also more general parabolic problems, should thus be rather easily possible in the case of Dirichlet boundary conditions, since then the solutions are completely local in time (Gander, Ohlberger and Rave 2024), as is the case in space with solvation models in computational chemistry; see Ciaramella and Gander (2017, 2018*a*,*b*). With Neumann or periodic boundary conditions, it should still be possible to do PinT computations, provided we can propagate low-frequency solution components, like the constant in our example, effectively over long times, for example using a coarse grid.

2.2. *Advection–diffusion equation*

We now consider the advection–diffusion equation with homogeneous Dirichlet and periodic boundary conditions[1] on the unit domain $\Omega = (0, 1)$,

$$\partial_t u(x,t) + \partial_x u(x,t) - \nu \partial_{xx} u(x,t) = g(x,t) \quad \text{in } \Omega \times (0,T], \tag{2.5}$$

with initial condition $u(x,0) = u_0(x)$, where $\nu > 0$ is the diffusion parameter. In Figure 2.2(a–d) we show the solution obtained with zero Dirichlet boundary conditions, and in Figure 2.2(e–h) the solution obtained with periodic boundary conditions. In (a–c) and (e–g) we use a zero initial condition, $u_0(x) = 0$, and the same source term (2.4) used for the heat equation for three different values of the diffusion parameter, $\nu = 1$, 10^{-2} and 5×10^{-4}. We see that when ν is large, then the diffusion part dominates and the solution has similar properties to the solution of the heat equation. If ν is small, however, i.e. the advection part plays a dominant role, then the solution is transported from left to right over a much longer time, as we see in Figure 2.2(b,c). In (d) and (h) we use a zero source term but a non-zero initial condition $u_0(x) = \sin^2(8\pi(1-x)^2)$ and again the small diffusion parameter 5×10^{-4}. We see that now all the fine features present in the high-frequency components of the initial condition are transported far in time. Nevertheless, for both ν large and ν small, we can still compute the solution for $t \in (1.25, 2.5)$ before we obtain the solution earlier in time, because all solution components are eventually diffused or leave the domain.

For periodic boundary conditions, however, we see in Figure 2.2(e–h) that the advection–diffusion equation transports information over long times: in (e) with large diffusion this information is only low-frequency, a constant, as for the heat equation, and PinT computations are still possible if we have a way of transporting coarse solution components far in time, for example using a coarse grid. In (f) and (g), however, we see that when the diffusion parameter becomes small, ever finer information is transported very far in time, and for successful PinT computation there must be a mechanism to propagate this information effectively far in time. Panel (h), without source and just a non-zero initial condition, shows that for small diffusion, a lot of fine, high-frequency information propagates very far in time, and

[1] We would not learn anything new with Neumann conditions.

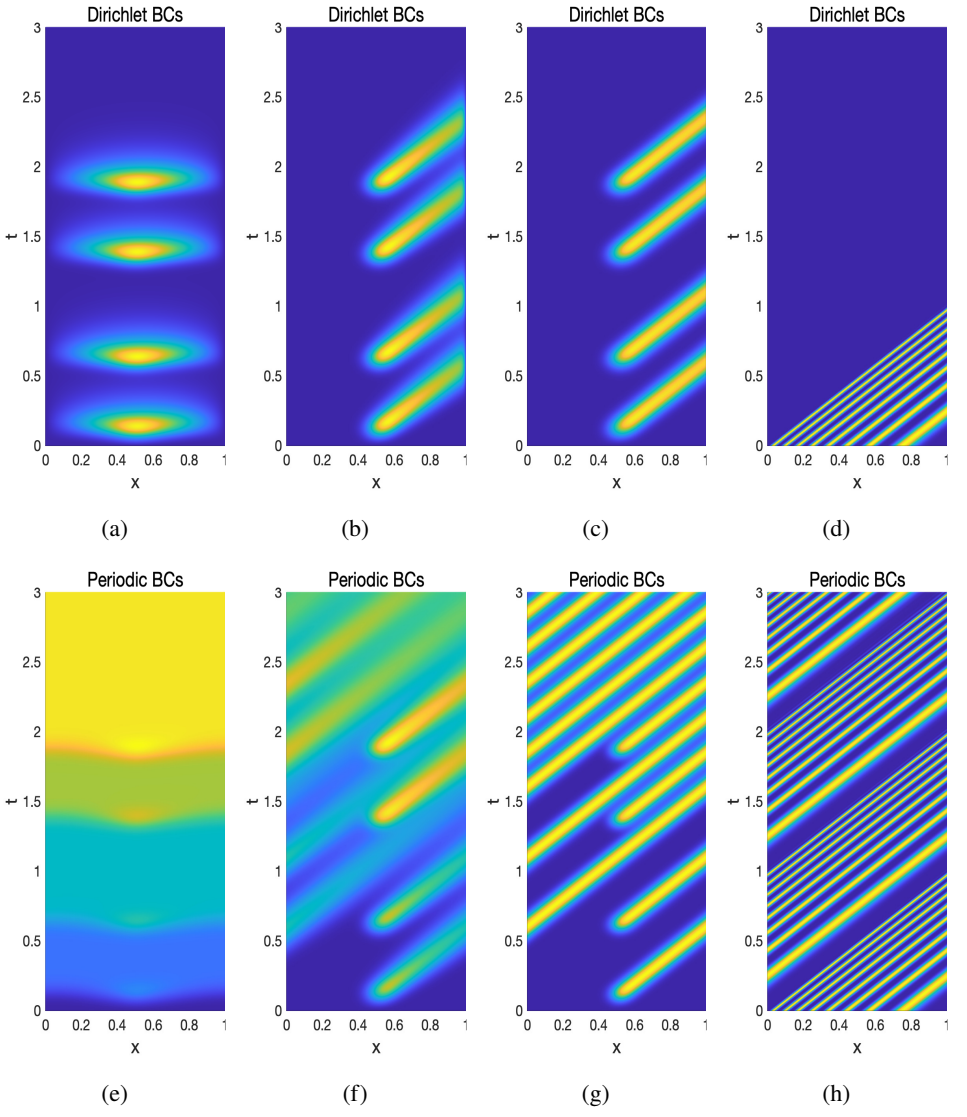

Figure 2.2. Advection–diffusion equation with zero Dirichlet boundary conditions (a–d) and periodic boundary conditions (e–h). In panels (a–c) and (e–g) we use a zero initial condition, $u_0(x) = 0$, and the same source term as in Figure 2.1 for the heat equation, and an ever smaller diffusion parameter $\nu = 1$, 10^{-2} and 5×10^{-4}. Panels (d) and (h) show the solution for zero source term and initial condition $u_0(x) = \sin^2(8\pi(1-x)^2)$ with small diffusion $\nu = 5 \times 10^{-4}$.

we can no longer precompute the solution later in time without knowing the solution earlier in time when the diffusion parameter becomes small. It is therefore difficult to do PinT computations, especially when $\nu \to 0$, in the hyperbolic limit. This is fundamentally different from the heat equation case, and only becomes manifest with periodic boundary conditions and small diffusion, an important point when testing the performance of PinT methods on advection-dominated problems.

2.3. *Burgers' equation*

To illustrate the difference between the various PinT methods in a nonlinear setting, we will use Burgers' equation,

$$\begin{aligned} \partial_t u(x,t) - \nu \partial_{xx} u(x,t) + \frac{1}{2}\partial_x(u^2(x,t)) &= g(x,t) \quad \text{in } \Omega \times (0,T], \\ u(x,0) &= u_0(x) \quad \text{in } \Omega, \end{aligned} \tag{2.6}$$

with $\nu > 0$. In Figure 2.3(a–d) we show the solution obtained with zero Dirichlet boundary conditions, and in Figure 2.3(e–h) the solution obtained with periodic boundary conditions. In (a–c) and (e–g) we use a zero initial condition, $u_0(x) = 0$, and the same source term (2.4) used for the heat and advection–diffusion equation, also for three different values of the diffusion parameter, $\nu = 1$, 10^{-2} and 5×10^{-4}. We see that when ν is large, then the diffusion part dominates and the solution has similar properties to the solution of the heat equation. If ν is small and the nonlinear advection part starts playing a dominant role, then the solution is transported from left to right over a much longer time, as we see in Figure 2.2(b,c), as for advection–diffusion. However, we see a further very important new phenomenon in the nonlinear case: the solution shape changes as well, and even with the smooth source term, very sharp edges are forming in the solution, so-called shock waves, containing very high-frequency components that travel far in space and time. In (d) and (h) we use a zero source term but a non-zero initial condition $u_0(x) = \sin^2(8\pi(1-x)^2)$ as for advection–diffusion earlier, and again the small diffusion parameter 5×10^{-4}. We also see, from the already fine features present in the high-frequency components of the initial condition, that even sharper edges are formed in shock waves, and all are transported far in time. Nevertheless, for both ν large and ν small, we can still compute the solution for $t \in (1.25, 2.5)$ before we obtain the solution earlier in time, because all solution components are eventually diffused or leave the domain, as in the advection–diffusion case in Figure 2.2(a–d).

In contrast, for periodic boundary conditions, we see in Figure 2.3(e–h) that our observations from Figure 2.2(e–h) for the advection–diffusion equation are further accentuated, as soon as the diffusion parameter becomes small: ever finer information is generated and transported very far in time, through shock waves that are forming. For successful PinT computation, such high-frequency shock waves must be transported by a mechanism that propagates them effectively far in space and time, which is very difficult using a coarse grid, for example. Panel (h), without source and just a non-zero initial condition, shows the same effect for an

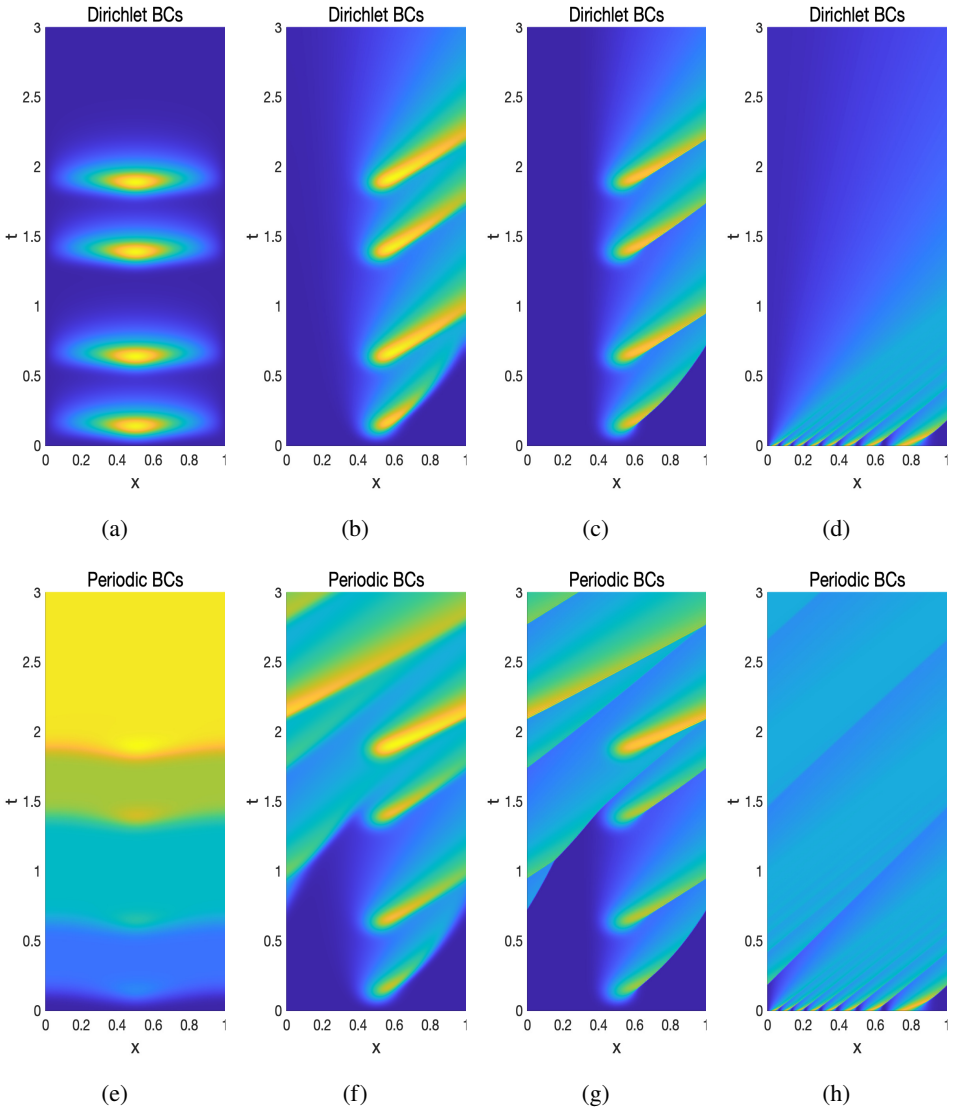

Figure 2.3. Burgers' equation with zero Dirichlet boundary conditions (a–d) and periodic boundary conditions (e–h). In panels (a–c) and (e–g) we use a zero initial condition, $u_0(x) = 0$, and the same source term as in Figure 2.1 for the heat equation, and an ever smaller diffusion parameter $\nu = 1, 10^{-2}$ and 5×10^{-4}. Panels (d) and (h) show the solution for zero source term and initial condition $u_0(x) = \sin^2(8\pi(1-x)^2)$ with small diffusion $\nu = 5 \times 10^{-4}$.

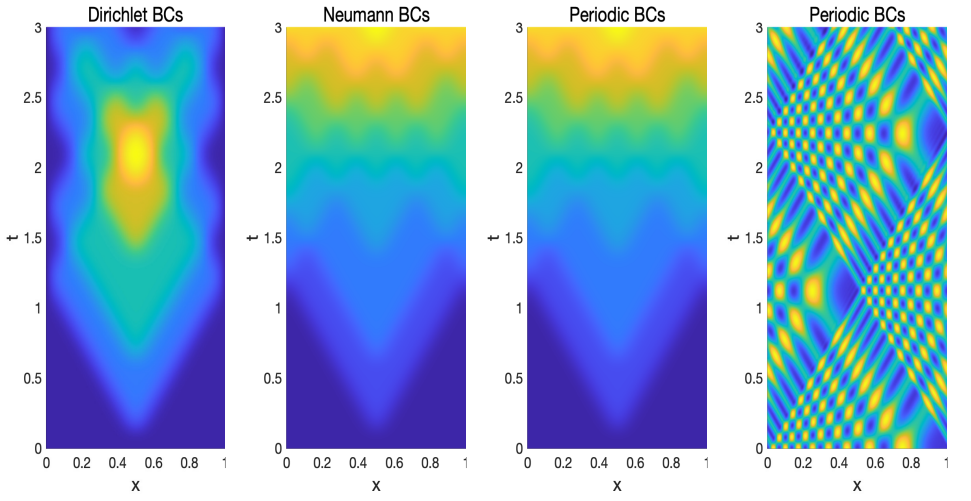

Figure 2.4. Solution of the second-order wave equation, with $c^2 = 0.2$, zero initial condition $u_0(x) = 0$ and the same source term as in Figure 2.1 for (a) Dirichlet, (b) Neumann and (c) periodic boundary conditions, and (d) the solution with zero source term and non-zero initial condition $u_0(x) = \sin^2(8\pi(1-x)^2)$.

initial condition transported over very long time: we can no longer precompute the solution later in time without knowing the solution earlier in time when the diffusion parameter becomes small. It is therefore even harder to do PinT computations in such nonlinear problems when $\nu \to 0$, in the hyperbolic limit, where shock waves are natural in the solutions and all frequency components travel very far in space and time. Note that again we need periodic boundary conditions and small diffusion to encounter these difficulties, an important point when testing the performance of PinT methods on such problems. In the next subsection we will see that for hyperbolic problems these difficulties already appear, no matter what boundary conditions are used.

2.4. *Second-order wave equation*

For hyperbolic problems, we will use the second-order wave equation as our model problem,

$$\begin{aligned} \partial_{tt} u(x,t) &= c^2 \partial_{xx} u(x,t) + g(x,t) && \text{in } (0,1)\times(0,T], \\ u(x,0) &= u_0(x) && \text{in } (0,1), \\ \partial_t u(x,0) &= 0 && \text{in } (0,1), \end{aligned} \tag{2.7}$$

with a constant wave speed $c > 0$. In Figure 2.4(a–c) we show the solution of the wave equation with the same source term (2.4) we used before, with Dirichlet,

Neumann and periodic boundary conditions. In all cases, we observe that for the wave equation, the solution depends in a complex and detailed manner over a long time on the various source terms in space and time. In Figure 2.4(d) we show the solution of the wave equation with zero source term but using the initial condition $u_0(x) = \sin^2(8\pi(1-x)^2)$ and zero first derivative in time. We see that the solution of this hyperbolic problem depends in a very detailed manner on all frequency components present in the initial condition, and this would be the same for the other boundary conditions as well. This is typical for hyperbolic problems and all boundary conditions; we only need periodic boundary conditions in the advection–diffusion and Burgers' equation case to make this difficulty appear for small ν, because the advection term is first-order and the transport has a direction. For the wave equation and other hyperbolic problems, this detailed and long time propagation in several directions with reflections is already present for Dirichlet and Neumann boundary conditions. It is this propagation of fine information over a long time in hyperbolic problems that makes time parallelization more challenging than for parabolic problems, and requires different PinT techniques to address it.

3. Effective PinT methods for hyperbolic problems

We have seen in Section 2 that parabolic problems have solutions that are rather local in time (see Figure 2.1), where with Dirichlet conditions all information is forgotten very rapidly over time, and with Neumann and periodic boundary conditions only the lowest-frequency component, namely the constant, remains over a long time. This changes when transport terms are present and become dominant (see Figures 2.2 and 2.3) and in the hyperbolic limit, and for hyperbolic problems in general, all frequency components can travel arbitrarily far in space and time; see Figure 2.4 for the second-order wave equation. PinT methods must take this into account to be effective. It is interesting that many methods designed specifically for hyperbolic problems also work well (or even better) for parabolic problems. An exception is that of the mapped tent pitching methods introduced at the end of Section 3.2, which use the finite speed of propagation in hyperbolic problems in their construction. On the other hand, PinT methods designed for parabolic problems (see Section 4) do not generally perform well for hyperbolic problems.

3.1. Historical development

We present four PinT methods that have proved effective for hyperbolic problems. For each method we show the main theoretical properties and demonstrate these properties using the four PDEs introduced in Section 2.

The first methods are rooted in solving overlapping or non-overlapping space–time-continuous subproblems, an approach initially proposed for parabolic problems in Gander (1999) and independently introduced in Giladi and Keller (2002).

This strategy incorporates elements of both domain decomposition (DD) methods, a long-established technique for parallel PDE solving going back to Schwarz (1870), and waveform relaxation (WR) methods, which originated in circuit simulations (Lelarasmee *et al.* 1982). These methods were developed and analysed both for parabolic and hyperbolic problems in Gander (1997), and the name Schwarz waveform relaxation (SWR) methods was coined in Gander *et al.* (1999). Further results for nonlinear parabolic problems can be found in Gander (1999) and Gander and Rohde (2005). Optimized Schwarz waveform relaxation (OSWR) methods using more effective transmission conditions were developed for parabolic problems in Gander and Halpern (2007), Bennequin, Gander and Halpern (2009) and Bennequin, Gander, Gouarin and Halpern (2016), and for hyperbolic problems in Gander, Halpern and Nataf (2003) and Gander and Halpern (2004); see also Gander, Lunowa and Rohde (2023*c*) for nonlinear advection–diffusion equations. The recently developed unmapped tent pitching (UTP) technique (Ciaramella, Gander and Mazzieri 2023) is based on SWR. There are also Dirichlet–Neumann and Neumann–Neumann waveform relaxation variants; see Gander, Kwok and Mandal (2016*b*, 2021*b*).

The third method is based on the time parallelization of the integral deferred correction (IDC) technique. IDC for evolution problems was first introduced in Böhmer and Stetter (1984), and was later identified in Dutt, Greengard and Rokhlin (2000) as a specialized time-integrator, which theoretically has the capability to generate numerical solutions of arbitrarily high order by accurately treating the associated integral. Revisionist integral deferred correction (RIDC) is one such technique (Christlieb *et al.* 2010) that can be used parallel in time, and there is another recent parallel version (PIDC) from Guibert and Tromeur-Dervout (2007), which we will introduce in detail in Section 3.3.

The fourth time-parallel method that we will introduce in Section 3.4 is the ParaExp method, proposed a decade ago by Gander and Güttel (2013), which relies on a new strategy of separately handling the initial value and source term; see also Merkel, Niyonzima and Schöps (2017) and Kooij, Botchev and Geurts (2017), and Gander, Güttel and Petcu (2018*a*) for a nonlinear variant.

Finally, in Section 3.5, we will present the ParaDiag family of methods. Time-parallel methods based on diagonalization were first proposed in Maday and Rønquist (2008) as direct time-parallel solvers, without iteration, and they were studied in more detail in Gander, Halpern, Ryan and Tran (2016*a*) for parabolic problems, with a nonlinear variant in Gander and Halpern (2017), and in Gander, Halpern, Rannou and Ryan (2019) for hyperbolic problems. Iterative variants then appeared rapidly, within WR methods (Gander and Wu 2019) or within Parareal (Gander and Wu 2020). Approximate ParaDiag methods were also used in McDonald *et al.* (2018) and Liu and Wu (2020) as preconditioners for Krylov methods, applied directly to the all-at-once system. A comprehensive study of ParaDiag methods appeared in Gander *et al.* (2019). Since then, ParaDiag methods have gained widespread traction in the PinT field, with new techniques enhancing these

methods; see e.g. Kressner, Massei and Zhu (2023) for a direct ParaDiag technique using interpolation, and Gander and Palitta (2024) for a new ParaDiag variant combining the Sherman–Morrison–Woodbury formula and Krylov techniques.

3.2. Schwarz waveform relaxation (SWR) methods

SWR combines the strengths of the classical Schwarz DD method and WR, while overcoming some of their inherent limitations. In the context of evolution PDEs, the Schwarz DD method typically involves a uniform implicit time discretization, followed by the application of the DD technique to solve the resulting elliptic problems at each time-step sequentially; see e.g. Cai (1991), Meurant (1991) and Cai (1994). The DD iterations need to converge at each time-step before proceeding to the next, across all subdomains, and we have to use the same time discretization across subdomains, which undermines a key advantage of DD methods, namely to tailor numerical treatments to each subdomain individually.

On the other hand, the classical WR method begins with a system of ODEs, often obtained from a spatial discretization of an evolution PDE, which is then solved using a dynamic iteration similar to the Picard iteration but using an appropriate system partitioning. For instance, in the case of the linear system of ODEs (2.1), the WR iteration can be expressed as

$$\frac{\mathrm{d}\boldsymbol{u}^k(t)}{\mathrm{d}t} - M\boldsymbol{u}^k(t) = N\boldsymbol{u}^{k-1}(t) + f(t), \quad t \in (0,T),$$

where $k \geq 1$ denotes the iteration index, $\boldsymbol{u}^k(0) = \boldsymbol{u}_0$ for all $k \geq 0$, and (M,N) represents a consistent splitting of A such that $A = M+N$. For Jacobi (diagonal) or Gauss–Seidel (triangular) type splittings, solving for $\boldsymbol{u}^k(t)$ boils down to solving a series of scalar ODEs. In the Jacobi case, all these ODEs can be solved in parallel, making this into a PinT method in the sense that the future of all unknowns is approximated before the future of connected unknowns is already known. Similarly in the Gauss–Seidel case, one can obtain such parallelism using red–black or other colourings. Even more parallelism can be introduced using the cyclic reduction technique; see Worley (1991), Horton, Vandewalle and Worley (1995) and Simoens and Vandewalle (2000). However, a significant challenge of WR lies in finding an effective system splitting to ensure rapid convergence. As remarked by Nevanlinna (1989, pp. 329, 331):

> In practice, one is interested in knowing what subdivisions yield fast convergence for the iterations . . . The splitting into subsystems is assumed to be given. How to split in such a way that the coupling remains weak is an important question.

A bad splitting can lead to arbitrarily slow convergence or even divergence, rendering WR impractical.

SWR circumvents these limitations by initially decoupling the spatial domain (rather than performing a spatial discretization first) and then independently solving the space–time-continuous PDEs on these subdomains, similar to the WR approach.

This approach allows for the use of tailored space and time discretizations for each subdomain problem; but more importantly, knowing that the space–time subdomain problems are coupled for a particular PDE, one can design transmission conditions which decouple the problems such that the methods converge very rapidly, completely addressing the difficulty identified by Nevanlinna above. This leads to the class of optimized Schwarz waveform relaxation (OSWR) methods, which have been studied for many different types of PDEs; see e.g. Martin (2009) for the shallow water equations, Courvoisier and Gander (2013) for the time domain Maxwell equations, Halpern and Szeftel (2010), Besse and Xing (2017) and Antoine and Lorin (2017) for Schrödinger equations, Audusse, Dreyfuss and Merlet (2010) for the primitive equations of the ocean, Antoine and Lorin (2016) for quantum wave problems, Wu (2017) for fractional diffusion problems, Thery, Pelletier, Lemarié and Blayo (2022) for the coupled Ekman boundary layer problem, and also the many references therein. OSWR methods have distinct convergence characteristics for first-order parabolic problems (such as the advection–diffusion equation (2.5) and the nonlinear Burgers' equation (2.6)) compared to second-order hyperbolic problems such as the wave equation (2.7). In the following, we present these two types of problems separately.

3.2.1. First-order parabolic problems

For the advection–diffusion equation (2.5) with homogeneous Dirichlet boundary conditions, $u(0,t) = u(L,t) = 0$, and an initial condition, $u(x,0) = u_0(x)$, the OSWR method with the two overlapping subdomains $\Omega_1 := (0, \beta L)$ and $\Omega_2 := (\alpha L, L)$, $\alpha < \beta$, and Robin transmission conditions is given by

$$\begin{cases} \partial_t u_1^k(x,t) + \mathcal{L} u_1^k(x,t) = 0 \quad (x,t) \in \Omega_1 \times (0,T], \\ u_1^k(0,t) = 0, \\ \dfrac{1}{p}\partial_x u_1^k(\beta L,t) + u_1^k(\beta L,t) = \dfrac{1}{p}\partial_x u_2^{k-1}(\beta L,t) + u_2^{k-1}(\beta L,t), \\ \partial_t u_2^k(x,t) + \mathcal{L} u_2^k(x,t) = 0 \quad (x,t) \in \Omega_2 \times (0,T], \\ \dfrac{1}{p}\partial_x u_2^k(\alpha L,t) - u_2^k(\alpha L,t) = \dfrac{1}{p}\partial_x u_1^{k-1}(\alpha L,t) - u_1^{k-1}(\alpha L,t), \\ u_2^k(L,t) = 0, \end{cases} \tag{3.1}$$

with $\mathcal{L} = \partial_x - \nu\partial_{xx}$, and initial conditions $u_1^k(x,0) = u_0(x)$ for $x \in \Omega_1$ and $u_2^k(x,0) = u_0(x)$ for $x \in \Omega_2$. Here, $k \geq 1$ represents the iteration index, $\{u_1^0(\alpha L,t), u^0(\beta L,t)\}$ are initial guesses for $t \in (0,T]$ and $0 < \alpha \leq \beta < 1$, and $(\beta - \alpha)L$ denotes the overlap size. We use Robin transmission conditions (TCs) in (3.1) with parameter $p > 0$ at $x = \alpha L$ and $x = \beta L$ to transmit information between the subdomains, and the classical Dirichlet TCs correspond to the limit $p \to \infty$, i.e. $u_1^k(\beta L,t) = u_2^{k-1}(\beta L,t)$ and $u_2^k(\alpha L,t) = u_1^{k-1}(\alpha L,t)$. It is straightforward to generalize this two-subdomain case in (3.1) to a multi-subdomain scenario, and the OSWR method

for nonlinear problems is obtained by simply replacing the linear operator $\mathcal{L}$ with the corresponding nonlinear one in (3.1).

For the OSWR iteration given in (3.1), the optimized choice of the parameter p and the corresponding convergence factor were analysed by Gander and Halpern (2007) under the simplified assumption that the space domain is unbounded.

Theorem 3.1 (Gander and Halpern 2007). For OSWR (3.1) with $\mathcal{L} = \partial_x - \nu\partial_{xx}$ and an overlap size of $l > 0$, the optimized choice for the Robin parameter, denoted by p^*, is given by $p^* = \tilde{p}^* s/\nu$, where $\tilde{p}^*$ is the unique solution of the nonlinear equation

$$R_0(y_0, \tilde{p}^*, y_0) = R_0(\bar{y}(y_0, \tilde{p}^*), \tilde{p}^*, y_0), \tag{3.2a}$$

provided that $y_0 := l/\nu < y_c$, where y_c is a constant equal to $1.618386576\ldots$, and

$$R_0(y, \tilde{p}, y_0) = \frac{(y-\tilde{p})^2 + y^2 - y_0^2}{(y+\tilde{p})^2 + y^2 - y_0^2} \mathrm{e}^{-y},$$

$$\bar{y}(y_0, \tilde{p}) = \sqrt{\frac{y_0^2 + 2\tilde{p} + \sqrt{\tilde{p}(-\tilde{p}^3 - 4\tilde{p}^2 + (4 + 2y_0^2)\tilde{p} + 8y_0^2)}}{2}}.$$

The function $R_0(y, \tilde{p}, y_0)$ is the convergence factor of the OSWR iteration, obtained in Fourier space, where y corresponds to a single Fourier mode $\omega \in [\pi/T, \pi/\Delta t]$, i.e. $y = l\omega/\nu$.

If, on the other hand, $y_0 \geq y_c$, then $\tilde{p}^*$ is the unique solution of

$$y_0 = \tilde{p}^* \sqrt{\frac{\tilde{p}^*}{4 + \tilde{p}^*}}. \tag{3.2b}$$

With the optimized Robin parameter p^*, the convergence factor ρ over all relevant Fourier modes can be bounded as

$$\rho := \max_{y \in [y_{\min}, y_{\max}]} R_0(y, \tilde{p}^*, y_0) \leq R_0(\bar{y}(y_0, \tilde{p}^*), \tilde{p}^*, y_0), \tag{3.2c}$$

where

$$y_{\min} = \frac{l\pi}{\nu T} \quad \text{and} \quad y_{\max} = \frac{l\pi}{\nu \Delta t}.$$

As we mentioned above, classical SWR with Dirichlet TCs corresponds to the case $p = \infty$ in (3.1). By setting $p = \infty$ in the function R_0, we obtain

$$\rho \leq \mathrm{e}^{-y_{\min}} = \exp\left(-\frac{l\pi}{\nu T}\right), \tag{3.3}$$

which was analysed in Gander and Halpern (2007, Section 3).

We now show a numerical experiment to illustrate OSWR. We discretize the advection–diffusion operator $\mathcal{L}$ using a centred finite difference method that is backward Euler in time. Let $L = 8.2$, $T = 5$, $\Delta t = 0.01$, $\Delta x = 0.02$ and $l = 2\Delta x$. The initial value for the advection–diffusion equation is $u_0(x) = \mathrm{e}^{-10(x-L/2)^2}$.

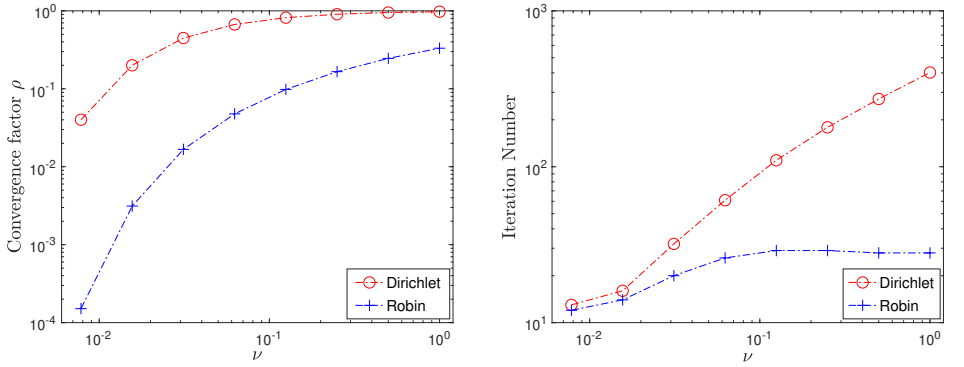

(a) (b)

Figure 3.1. (a) The theoretical convergence factor of the OSWR method when applied to the advection–diffusion equation (2.5) decreases when the diffusive parameter ν decreases. (b) The iteration, measured in a four-subdomain numerical experiment with tolerance of 10^{-8}, supports this prediction very well.

In Figure 3.1(a) we show the theoretical convergence factor of the SWR method with Dirichlet and optimized Robin TCs as a function of the diffusion parameter ν. We see that the convergence factor becomes small when the advection term becomes dominant, and the method converges ever more rapidly. To test this numerically, we decompose the spatial domain $(0, L)$ into four subdomains and solve the advection–diffusion equation using the OSWR method for several values of the parameter ν. The method starts from a random initial guess, and we stop the iteration when the error between the iterate and the converged solution is less than 10^{-8}. The iteration number for Dirichlet and optimized Robin TCs is shown in Figure 3.1(b), and we see that indeed fewer iterations are required when ν is small, as predicted by the theoretical results in Figure 3.1(a).

For a given ν, however, the discretized OSWR method with four subdomains may not converge as rapidly as predicted by the theoretical convergence factor ρ obtained for a two-subdomain decomposition at the continuous level on an unbounded domain. For instance, when $\nu = 0.1$, the iteration numbers shown in Figure 3.1 are 92 for Dirichlet TCs and 28 for Robin TCs, but iteration numbers predicted by ρ are 32 for Dirichlet TCs and 4 for Robin TCs, which are significantly smaller. The reason for this discrepancy is that the convergence factor ρ in Theorem 3.1 is analysed for the two-subdomain case at the space–time-continuous level on an unbounded domain, and we tested the discretized SWR method in the four-subdomain case on a bounded domain. Convergence analyses of SWR with Dirichlet TCs in the multi-subdomain case can be found in Gander and Stuart (1998) and Wu, Huang and Huang (2012). However, a comprehensive convergence analysis for Robin TCs in the multi-subdomain case is still lacking. For Robin TCs, the convergence of SWR in the two-subdomain case at the semi-discrete level can be found in Wu

and Al-Khaleel (2014); see also the detailed studies in Gander, Halpern, Hubert and Krell (2020, 2021*a*) for the steady-state case between continuous and discrete analyses on bounded and unbounded domains.

In addition to Dirichlet and Robin TCs, there are efforts to further accelerate OSWR using Ventcel TCs (Bennequin *et al.* 2016). Essentially, these TCs serve as local approximations of the *optimal* TCs analysed in Fourier (or Laplace) space in Gander and Halpern (2007, Section 3), namely

$$\partial_x - \frac{1}{2\nu}\mathcal{F}^{-1}(1+\sqrt{1+\mathrm{i}4\nu\omega}),$$

where $\mathrm{i}=\sqrt{-1}$ and $\mathcal{F}^{-1}$ denotes the inverse Fourier transform with ω representing the Fourier mode. In an asymptotic sense, i.e. $l = C_1\Delta x$, $\Delta t = C_1\Delta x^{\beta}$, and with Δx being small, the convergence factor ρ satisfies $\rho = 1 - O(\Delta x^{\gamma})$, where $\gamma > 0$ is a quantity that depends on β; see Gander and Halpern (2007) and Bennequin *et al.* (2009, 2016). Convolution TCs analysed in Wu and Xu (2017) result in a mesh-independent constant convergence factor $\rho = 1 - C$, where $C \in (0,1)$. This is particularly useful for handling evolution PDEs with non-local terms, such as Volterra partial integro-differential equations.

3.2.2. *Second-order hyperbolic problems*

Unlike for first-order parabolic problems, for second-order hyperbolic problems (e.g. the wave equation (2.7)), the SWR method converges in a finite number of iterations, even when using simple Dirichlet transmission conditions. Applying SWR to the wave equation for a two-subdomain decomposition leads to the algorithm

$$\begin{cases} \partial_{tt}u_1^k(x,t) = c^2\partial_{xx}u_1^k(x,t) + g(x,t) & (x,t)\in\Omega_1\times(0,T], \\ u_1^k(x,0) = u_0(x),\ \partial_t u_1^k(x,0) = \tilde{u}_0(x) & x\in(0,\beta L), \\ u_1^k(0,t) = 0,\ u_1^k(\beta L,t) = u_2^{k-1}(\beta L,t) & t\in(0,T), \end{cases} \\ \begin{cases} \partial_{tt}u_2^k(x,t) = c^2\partial_{xx}u_2^k(x,t) + g(x,t) & (x,t)\in\Omega_2\times(0,T], \\ u_2^k(x,0) = u_0(x),\ \partial_t u_2^k(x,0) = \tilde{u}_0(x) & x\in(\alpha L,L), \\ u_2^k(\alpha L,t) = u_1^{k-1}(\alpha L,t),\ u_2^k(L,t) = 0 & t\in(0,T), \end{cases} \tag{3.4}$$

where $c > 0$ and $0 < \alpha < \beta < 1$.

Theorem 3.2 (Gander 1997, Theorem 6.3.3). For the SWR method (3.4), the errors at the interfaces $x = \alpha L$ and $x = \beta L$ become zero after k iterations, i.e. $u_1^k(\alpha L,t) - u(\alpha L,t) = 0$ and $u_2^k(\beta L,t) - u(\beta L,t) = 0$, provided that

$$k > \frac{Tc}{\beta-\alpha}.$$

The reason for this convergence result lies in the finite speed of propagation inherent to hyperbolic problems. By exploiting this property, similar results can be

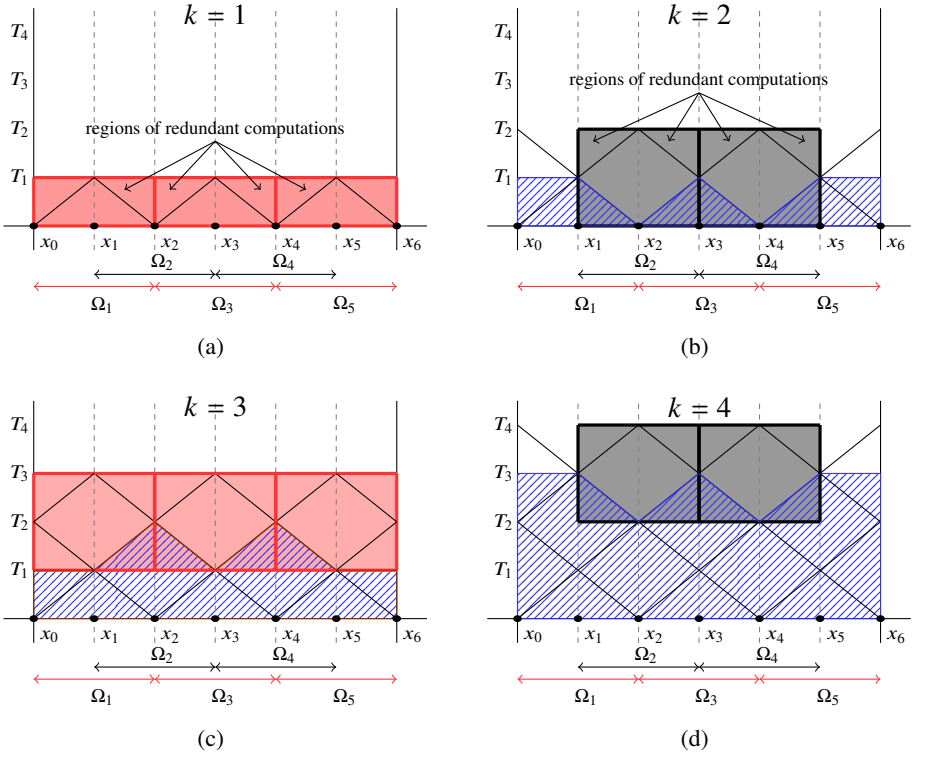

Figure 3.2. Illustration of red–black SWR with generous overlap.

achieved in the case of many subdomains, as well as for more general decompositions in higher dimensions (Gander and Halpern 2004) and for other hyperbolic equations; see e.g. Gander and Rohde (2005) for one-dimensional nonlinear conservation laws.

Theorem 3.2 shows a very important property of SWR applied to hyperbolic problems, already indicated in Gander *et al.* (2003, Figure 3.1): the subdomains are computing the exact solution in the cone within the subdomain which is only influenced by the initial condition, and not by the transmission conditions where possibly incorrect data is still coming from the neighbouring subdomains. Using this property, one can choose the space–time subdomains in SWR applied to hyperbolic problems in order to avoid iterations and advance directly with space–time subdomain solves in parallel. To illustrate this, it is best to consider again the one-dimensional wave equation (2.7) and a *red–black* domain decomposition with generous overlap, as was done in Ciaramella *et al.* (2023); see Figure 3.2. In panel (a) we solve the wave equation in parallel within the three red subdomains in space–time, i.e. in $\Omega_j \times (0, T_1)$ for $j = 1, 3, 5$. We use arbitrary interface data at $x = x_2$ and $x = x_4$ because the solution there is not yet known. Due to the finite

speed of propagation, we obtain the exact solution within triangular tents in space–time, bounded by the characteristic lines of the wave equation. These tents are marked in blue in panel (b), and the solution is also correct in two additional small zones on the left and right, since the outer boundary conditions are known. In this first red solve, SWR also computes a not yet correct approximation in the regions above the correct tents, as indicated in (a): SWR performs redundant computations, as advocated by Nievergelt in order to obtain more parallelism. In the next step of this red–black SWR, we compute wave equation solutions in the black subdomains $\Omega_j \times (0, T_2)$ for $j = 2, 4$ in space–time, as indicated in (b). Since we already have the correct solution in the blue region, the exact solution is now obtained in the two rhomboid blue tents indicated in (c), again at the cost of some redundant computations. Next we again solve in the red subdomains, but now further in time in the interval (T_1, T_3). Continuing this red–black SWR algorithm, we obtain the exact solution further and further advanced in time, as indicated in (d).

This red–black SWR algorithm is an effective and simple way to implement one of the most powerful current space–time solvers for hyperbolic problems, namely the mapped tent pitching (MTP) algorithm from Gopalakrishnan, Schöberl and Wintersteiger (2017); see Gopalakrishnan, Hochsteger, Schöberl and Wintersteiger (2020) for its application to time domain Maxwell equations. In MTP, we map the tent shape which we have seen in red–black SWR to space–time cylinders in which the solution is then computed by classical time-stepping, and then the solution is mapped back, thus avoiding redundant computations. However, we have the extra cost of computing the mapping, and also after the mapping the computational domains have the same size as the space–time subdomains in the red–black SWR above, and thus comparable computational cost. In addition, in MTP, order reduction was observed due to the mapping, and specialized time-integrators were developed and need to be used to avoid this. In contrast, in red–black SWR, now also called unmapped tent pitching (UTP), no order reduction occurs, and red–black SWR can be very easily implemented, even for higher spatial dimensions, using restricted additive Schwarz (RAS) techniques from DD directly applied to the all-at-once space–time system; see Gander (2008) for an explanation. In Figure 3.3 we show an example of using red–black SWR or equivalently UTP to solve our wave equation model problem (2.7), whose solution is shown in Figure 2.4(d). We see that without knowing anything about the tent structure, UTP constructs the exact solution in the red and black tents, and advances exactly like MTP. Note that UTP can also be just as easily applied to nonlinear hyperbolic problems, and if we do not know the tent height, it suffices to look at the residual in the computed solution, which naturally indicates the tent height by how far the residual has become zero in time, and we can adapt the time domain length $T_i - T_{i-1}$ accordingly!

Clearly the original MTP is not appropriate for parabolic problems, since for such problems the speed of propagation is infinite, and hence there are no tents in which the solution would be correct. However, SWR and thus UTP can also be very effective for parabolic problems, especially the optimized SWR variants (see e.g.

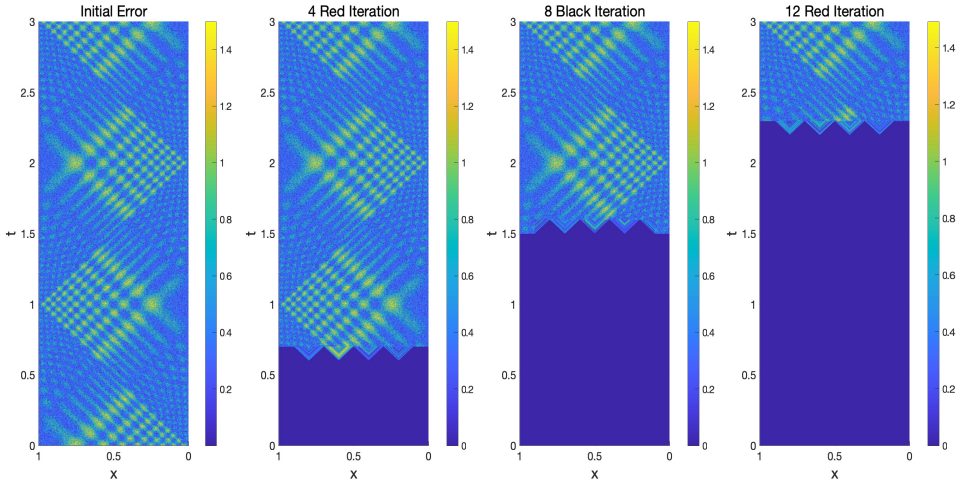

Figure 3.3. Red–black SWR or equivalently UTP applied to the second-order wave equation: (a) initial error with random initial guess, (b) fourth red iteration, (c) eighth black iteration and (d) 12th red iteration.

Gander and Halpern 2007, Bennequin *et al.* 2009), and for slightly diffusive problems such as our advection-dominated diffusion model problem we could consider applying UTP, maybe with one or two additional iterations in each time slab.

3.3. Time-parallel IDC

Integral deferred correction (IDC), introduced by Dutt *et al.* (2000), serves as a technique to obtain high-order numerical solutions through an iterative correction procedure. While the original IDC is sequential in time, there are two more recent techniques to parallelize IDC in time: the pipeline IDC (PIDC) method by Guibert and Tromeur-Dervout (2007) and the revisionist IDC (RIDC) method by Christlieb *et al.* (2010). Both PIDC and RIDC fundamentally differ from the original IDC, but to understand them it is necessary to explain first how IDC works. To this end, we rewrite the nonlinear ODE (2.2) as an integral equation:

$$\boldsymbol{u}(t) = \boldsymbol{u}_0 + \int_0^t f(\boldsymbol{u}(\tau), \tau)\, \mathrm{d}\tau, \quad t \in (0, T]. \tag{3.5}$$

Suppose we already have a rough approximation $\tilde{\boldsymbol{u}}(t)$ of the desired solution $\boldsymbol{u}(t)$, for example by simply setting $\tilde{\boldsymbol{u}}(t) \equiv \boldsymbol{u}_0$ for $t \in [0, T]$ or by solving the ODE with lower accuracy. To improve the approximation $\tilde{\boldsymbol{u}}(t)$, we introduce the error $\boldsymbol{e}(t) := \boldsymbol{u}(t) - \tilde{\boldsymbol{u}}(t)$, and the residual

$$\boldsymbol{r}(t) := \boldsymbol{u}_0 + \int_0^t f(\tilde{\boldsymbol{u}}(\tau), \tau)\, \mathrm{d}\tau - \tilde{\boldsymbol{u}}(t), \quad t \in (0, T]. \tag{3.6}$$

By substituting $\boldsymbol{u}(t) = \boldsymbol{e}(t) + \tilde{\boldsymbol{u}}(t)$ into (3.5) and using (3.6), we can express the error $\boldsymbol{e}(t)$ in terms of the residual $\boldsymbol{r}(t)$:

$$\begin{aligned}\boldsymbol{e}(t) &= \boldsymbol{u}_0 + \int_0^t f(\tilde{\boldsymbol{u}}(\tau) + \boldsymbol{e}(\tau), \tau)\,\mathrm{d}\tau - \tilde{\boldsymbol{u}}(t) \\ &= \boldsymbol{r}(t) + \int_0^t \left[f(\tilde{\boldsymbol{u}}(\tau) + \boldsymbol{e}(\tau), \tau) - f(\tilde{\boldsymbol{u}}(\tau), \tau)\right]\mathrm{d}\tau, \quad t \in (0, T]. \end{aligned} \tag{3.7}$$

Taking a derivative, this is equivalent to the differential equation

$$\boldsymbol{e}'(t) - \boldsymbol{r}'(t) = f(\tilde{\boldsymbol{u}}(t) + \boldsymbol{e}(t), t) - f(\tilde{\boldsymbol{u}}(t), t), \quad t \in (0, T]. \tag{3.8}$$

Let the current approximate solution $\tilde{\boldsymbol{u}}$ be known at specific time points

$$0 = t_0 < t_1 < t_2 < \cdots < t_M = T, \quad \{\boldsymbol{u}_m^k\} := \tilde{\boldsymbol{u}}(t_m).$$

The procedure to obtain the next approximate solution $\{\boldsymbol{u}_m^{k+1}\}$ involves discretizing (3.8) and using a quadrature rule to approximate $\boldsymbol{r}(t)$ at the discrete time nodes. Applying the linear-θ method (with $\theta \in [0, 1]$) to (3.8) yields

$$\begin{aligned}\boldsymbol{e}_{m+1} - \boldsymbol{e}_m = \boldsymbol{r}_{m+1} - \boldsymbol{r}_m &+ \Delta t_m(1-\theta)\left[f\left(\boldsymbol{u}_m^{k+1}, t_m\right) - f\left(\boldsymbol{u}_m^k, t_m\right)\right] \\ &+ \Delta t_m \theta\left[f\left(\boldsymbol{u}_{m+1}^{k+1}, t_{m+1}\right) - f\left(\boldsymbol{u}_{m+1}^k, t_{m+1}\right)\right], \end{aligned} \tag{3.9}$$

where $m = 0, 1, \ldots, M-1$ and $\Delta t_m = t_{m+1} - t_m$. From (3.6),

$$\boldsymbol{r}_{m+1} - \boldsymbol{r}_m = \int_{t_m}^{t_{m+1}} f(\boldsymbol{u}^k(\tau), \tau)\,\mathrm{d}\tau - \left(\boldsymbol{u}_{m+1}^k - \boldsymbol{u}_m^k\right).$$

Substituting this into (3.9) and then using $\boldsymbol{u}_m^{k+1} = \boldsymbol{u}_m^k + \boldsymbol{e}_m^k$, we obtain

$$\begin{aligned}\boldsymbol{u}_{m+1}^{k+1} = \boldsymbol{u}_m^{k+1} &+ \Delta t_m(1-\theta)\left[f\left(\boldsymbol{u}_m^{k+1}, t_m\right) - f\left(\boldsymbol{u}_m^k, t_m\right)\right] \\ &+ \Delta t_m \theta\left[f\left(\boldsymbol{u}_{m+1}^{k+1}, t_{m+1}\right) - f\left(\boldsymbol{u}_{m+1}^k, t_{m+1}\right)\right] + \int_{t_m}^{t_{m+1}} f(\boldsymbol{u}^k(\tau), \tau)\,\mathrm{d}\tau, \end{aligned}$$

where the integral is computed using a quadrature rule:

$$\int_{t_m}^{t_{m+1}} f(\boldsymbol{u}^k(\tau), \tau)\,\mathrm{d}\tau \approx \sum_{j=1}^{M} \omega_{m,j} f\left(\boldsymbol{u}_j^k, t_j\right). \tag{3.10a}$$

The quadrature weights are determined by integrating the Lagrange polynomials,

$$\omega_{m,j} = \int_{t_m}^{t_{m+1}} \left(\prod_{i=1, i\neq j}^{M} \frac{\tau - t_i}{t_s - t_i}\right)\mathrm{d}\tau. \tag{3.10b}$$

In summary, with the discrete time points $\{t_m\}_{m=0}^{M}$ spanning the time interval $[0,T]$, IDC generates the approximate solution as

$$\begin{aligned}\boldsymbol{u}_{m+1}^{k+1} = \boldsymbol{u}_m^{k+1} + \Delta t_m(1-\theta)\big[f\big(\boldsymbol{u}_m^{k+1},t_m\big) - f\big(\boldsymbol{u}_m^{k},t_m\big)\big] \\ + \Delta t_m\theta\big[f\big(\boldsymbol{u}_{m+1}^{k+1},t_{m+1}\big) - f\big(\boldsymbol{u}_{m+1}^{k},t_{m+1}\big)\big] + \sum_{j=1}^{M}\omega_{m,j}f\big(\boldsymbol{u}_j^{k},t_j\big), \quad (3.11)\end{aligned}$$

where $k = 0,1,\ldots,k_{\max}-1$, and for each correction index k we sweep from left to right, i.e. $m = 0,1,\ldots,M-1$. The choice of quadrature rule determines the maximum order of accuracy achievable in practice. If we use M uniformly distributed nodes with distance Δt, the maximal order of accuracy is of $O(\Delta t^M)$ and, more specifically, we have the following result.

Theorem 3.3 (Dutt *et al.* 2000). Suppose the time-integrator is of order p, such as $p = 1$ for $\theta = 1$ (backward Euler) and $p = 2$ for $\theta = \frac{1}{2}$ (trapezoidal rule) in (3.11). Then the approximate solution $\{\boldsymbol{u}_m^k\}$ after k corrections is of order $O(\Delta t^{\min\{M,(k+1)p\}})$.

The original IDC method (Dutt *et al.* 2000) used Gauss nodes for the quadrature rule, resulting in a higher maximal order of accuracy. For instance, using Gauss–Lobatto nodes achieves an order of $2J-1$. This IDC variant is called *spectral deferred correction* (SDC) and serves as the key component of the PFASST algorithm, introduced in Section 4.3 below.

For long-time computations, where T is large, creating a uniformly high-order numerical approximation across the entire time interval is challenging, because it is difficult to accurately approximate a function over a large interval with a single high-order polynomial. In such scenarios it is natural to segment the time interval $[0,T]$ into multiple *windows*, denoted by $\{I_n := [T_{n-1},T_n]\}_{n=1}^{N_t}$, with $T_0 = 0$ and $T_{N_t} = T$. Then IDC can be applied to each window individually. Within each time window, a lower-order polynomial often provides precise quadrature, especially when the window size is small. However, this process is entirely sequential, since the computations for the $(n+1)$th window I_{n+1} must await the completion of computations for I_n. This dependence arises because the initial value for I_{n+1} remains unknown until the preceding window's computations are finalized. Additionally, within each time window, we use a basic IDC and the computation proceeds step by step.

3.3.1. Pipeline IDC (PIDC)

The first parallel version of IDC, known as PIDC, was introduced in Guibert and Tromeur-Dervout (2007). PIDC uses a *pipeline* parallelization approach for IDC. It is based on a simple concept applicable to any time evolution computation, already proposed by Womble (1990). Specifically, the computation for the next window $I_{n+1} = [T_n,T_{n+1}]$ can start when a preliminary initial value from the current computation on $I_n = [T_{n-1},T_n]$ at $t = T_n$ becomes available. For instance,

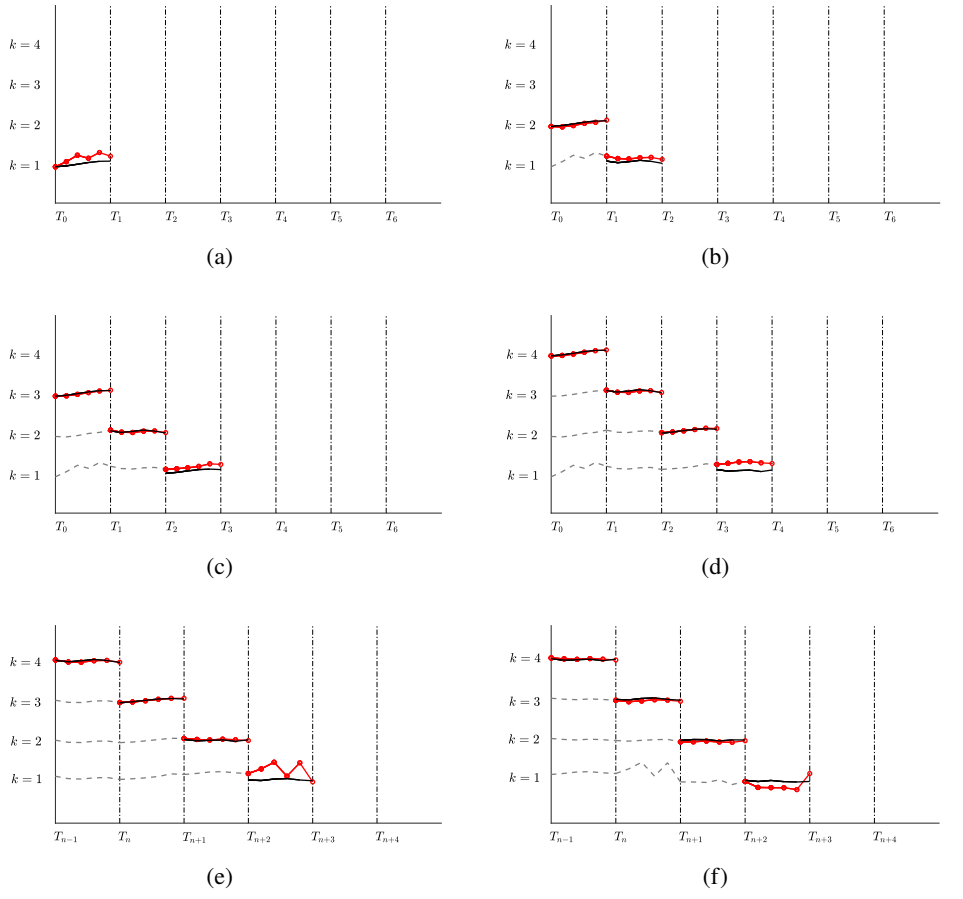

Figure 3.4. In PIDC with $k_{\max} = 4$, the sweeps on the four time windows can run simultaneously (e,f) once the initialization phase in the first four windows (a–d) is completed. The black dashed lines represent sweep histories, while the red solid lines marked with a red circle indicate current sweeps run in parallel. The black solid lines show the exact solution.

following the first sweep on I_n, an approximation $\boldsymbol{u}_{n,M}^1$ at $t = T_n$, i.e. the rightmost solution on window I_n after one sweep, is obtained, and we can compute the first sweep on I_{n+1} using $\boldsymbol{u}_{n,M}^1$ as the initial value at the same time as performing the second sweep on I_n. After this computation, we can already start on I_{n+2} while continuing on I_{n+1} and I_n, computing three sweeps in parallel. In general, for N_t time windows, when conducting the kth sweep on the nth window I_n, we simultaneously perform sweep $k-1$ on I_{n+1}, sweep $k-2$ on I_{n+2}, and so on, up to the first sweep on I_{n+k-1}. This procedure is illustrated in Figure 3.4 with $M = 6$ and $k_{\max} = 4$, where the first four sweeps represent the initial state. Following this stage, sweeps on I_n, I_{n+1}, I_{n+2}, and I_{n+3} are executed in parallel. On I_n

(with $n \geq 1$), because each sweep starts from a rough and changing initial value, there is no guarantee that the accuracy of the generated solution will increase as we proceed with the corrections. We illustrate this point by applying IDC and PIDC to the advection–diffusion equation (2.5) with two values of the diffusion parameter, $\nu = 1$ and $\nu = 10^{-3}$. We consider periodic boundary conditions and discretize with centred finite differences with mesh size $\Delta x = \frac{1}{64}$, which leads to the linear system of ODEs (2.1), i.e. $\boldsymbol{u}'(t) = A\boldsymbol{u}(t)$ with

$$A = \frac{\nu}{\Delta x^2} A_{\mathrm{xx}} - \frac{1}{2\Delta x} A_{\mathrm{x}},$$

where

$$\frac{\nu}{\Delta x^2} A_{\mathrm{xx}} \approx \nu \partial_{xx}, \quad \frac{1}{2\Delta x} A_{\mathrm{x}} \approx \partial_x$$

are the discretization matrices given by

$$A_{\mathrm{xx}} = \begin{bmatrix} -2 & 1 & & & 1 \\ 1 & -2 & 1 & & \\ & \ddots & \ddots & \ddots & \\ & & 1 & -2 & 1 \\ 1 & & & 1 & -2 \end{bmatrix}, \quad A_{\mathrm{x}} = \begin{bmatrix} 0 & 1 & & & -1 \\ -1 & 0 & 1 & & \\ & \ddots & \ddots & \ddots & \\ & & -1 & 0 & 1 \\ 1 & & & -1 & 0 \end{bmatrix}. \tag{3.12}$$

Let $T = 3$ and the window size be $\Delta T = \frac{1}{10}$. Then, using backward Euler as time-integrator, Figure 3.5 shows the maximal relative error for each time window for IDC and PIDC with $M = 5$, namely

$$\mathrm{err}_n^k = \frac{\max_m \|\boldsymbol{u}_{n,m}^{\mathrm{ref}} - \boldsymbol{u}_{n,m}^k\|_\infty}{\max_{n,m} \|\boldsymbol{u}_{n,m}^{\mathrm{ref}}\|_\infty},$$

where the reference solution $\boldsymbol{u}_{n,m}^{\mathrm{ref}}$ is computed by the built-in solver `ODE45` in MATLAB, using for both the relative and absolute tolerance `1e-13`. In each panel, for both IDC and PIDC, we show the initial error and the errors after 1 and 2 sweeps. The initial guess on the $(n+1)$th window $I_{n+1} = [T_n, T_{n+1}]$ is fixed simply as $\boldsymbol{u}_{n+1,m}^0 \equiv \boldsymbol{u}_{n,M}^1$ for $j = 0, 1, \ldots, M$.

The results in Figure 3.5 show that for good performance of IDC and PIDC, the solution of the problem needs to be regular. In the first row, we used the source function $g(x,t)$ from (2.4) with parameter $\sigma = 1000$, which implies a δ-function type source, such that the solution is not regular enough. We see in panel (a) that both IDC and PIDC perform similarly, and after the first correction the errors are not further reduced, the solution is not regular enough for a higher-order approximation to perform well. In panel (b) we see that when the diffusion is becoming small, the improvement of the first IDC iteration is much worse than in (a), and a further iteration does not help much either, and similarly for PIDC. In panel (c) we see that if we use a very regular source, (2.4) with parameter $\sigma = 5$, and thus the solution has enough regularity, both IDC and PIDC now improve for large diffusion in the second iteration as well, and PIDC is comparable to IDC. However, for small

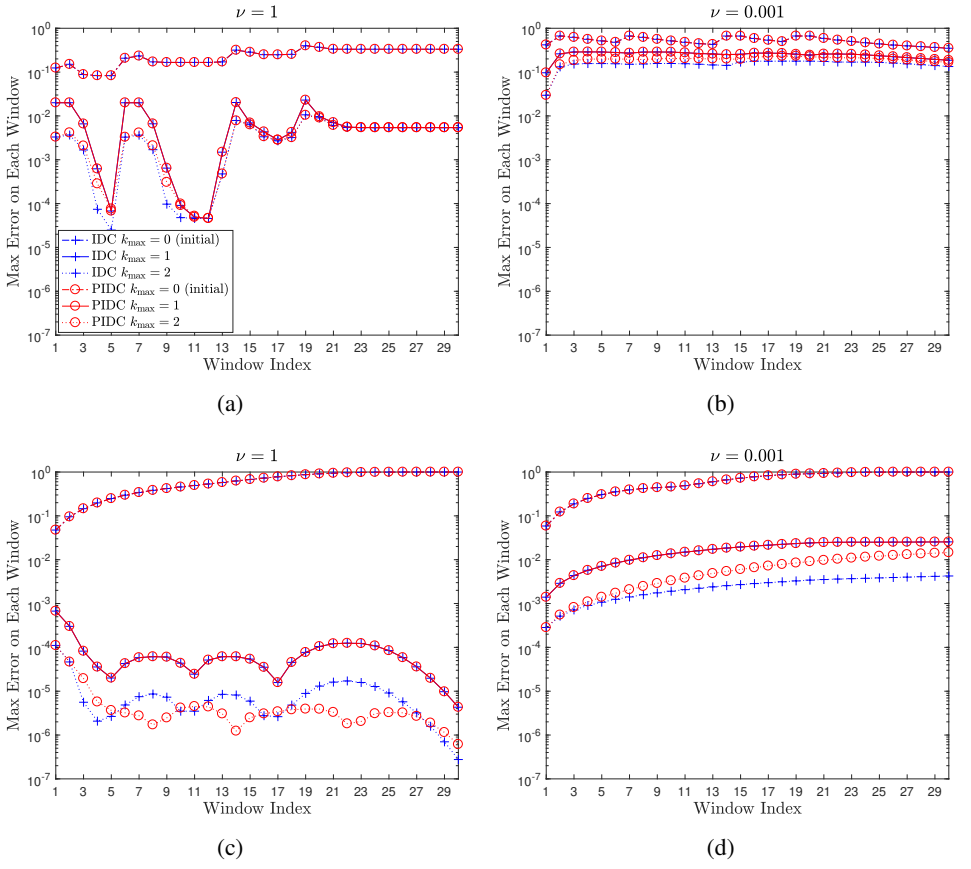

Figure 3.5. Maximum relative error on each time window for original IDC and its parallel version PIDC for the advection–diffusion equation (2.5) with source function $g(x,t)$ in (2.4) with $\sigma = 1000$ (low regularity, a,b) and $\sigma = 5$ (higher regularity, c,d), and large diffusion parameter (a,c) and small diffusion parameter (b,d). The legend in (a) is also valid for the other panels.

diffusion, in panel (d), again performance is not as good, and PIDC clearly performs less well at the second iteration compared to IDC. These results indicate that for hyperbolic problems, if the solution is not regular enough, PIDC will not be very suitable for PinT computations.

3.3.2. Revisionist IDC (RIDC)

The RIDC method proposed by Christlieb *et al.* (2010) uses a sliding IDC interval as the main new idea for more fine-grained parallelization. To do so, consider a quadrature rule with M equidistant nodes. In RIDC, a first processor computes the initial approximation using a low-order time-stepper, as in IDC, but once it arrives at the end of the IDC interval after M steps, it does not stop: it just continues

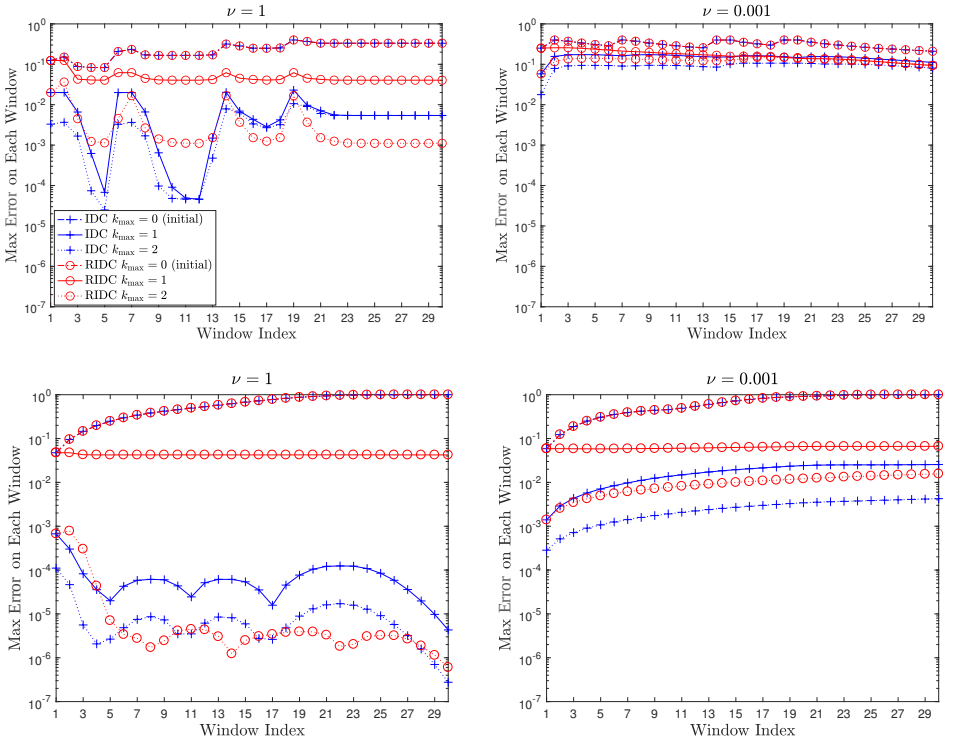

Figure 3.6. Maximum relative error on each time window for original IDC and its parallel version RIDC for the advection–diffusion equation (2.5) with source term $g(x,t)$ in (2.4) and initial condition $u(x,0) = 0$.

progressing in time, computing step $M+1$, $M+2$ and so on. With the first M values of the first processor available, the second processor now has enough information to start the first IDC correction. Once it arrives at the end of the first IDC interval computing the correction for the Mth step, the third processor can start, but the second processor does not stop: it just continues by moving its IDC interval and associated quadrature formula one fine time-step to the right, that is, instead of using the approximations from steps $1, 2, \ldots, M$ of the first processor, it considers the approximations from steps $2, 3, \ldots, M+1$ of the first processor as its IDC interval and quadrature nodes, and uses these to compute its approximation for step $(M+1)$. And then it considers the approximations from steps $3, 4, \ldots, M+2$ of the first processor as its IDC interval, and uses these as quadrature nodes to compute step $M+2$, and so on. Similarly, the third processor will also continue with a sliding IDC interval, and so on. Like PIDC, RIDC needs regularity to be effective, since it is a high-order approximation technique, and thus for hyperbolic problems in the case of low-regularity solutions, RIDC risks not being very effective for PinT computations. This is illustrated in Figure 3.6, where we apply IDC and RIDC to the advection–diffusion equation (2.5) with the same data used for Figure 3.5.

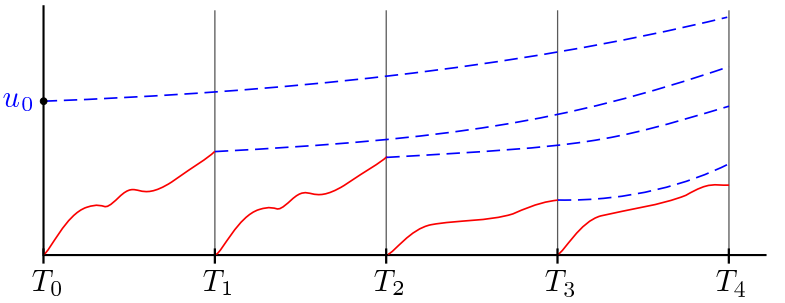

Figure 3.7. Two steps in the ParaExp solver.

3.4. ParaExp

The fourth time-parallel method we want to present is the ParaExp algorithm (Gander and Güttel 2013), which is a direct time-parallel method that solves linear problems such as (2.1), which is the semi-discrete version of PDEs like the advection–diffusion equation (2.5) or the wave equation (2.7); see also Merkel *et al.* (2017) and Kooij *et al.* (2017). ParaExp uses special approximations of the matrix exponential function, and there are also other such techniques, like REXI (Schreiber, Peixoto, Haut and Wingate 2018); see also the early PinT methods based on Laplace transforms REXI (Schreiber *et al.* 2018).

ParaExp is based on a time decomposition, and performs two steps in order to construct the solution. First, on each time interval, the equation is solved in parallel with a source term but zero initial condition (red problems in Figure 3.7),

$$\boldsymbol{v}_n'(t) = A\boldsymbol{v}_n(t) + \boldsymbol{g}(t), \quad t \in (T_{n-1}, T_n], \quad \boldsymbol{v}_n(T_{n-1}) = 0, \tag{3.13}$$

where $n = 1, 2, \ldots, N_t$ and $T_{N_t} = T$. We then solve in parallel the linear equation (2.1) without source terms (blue problems in Figure 3.7), using as initial conditions the results from (3.13),

$$\boldsymbol{w}_n'(t) = A\boldsymbol{w}_n(t), \quad t \in (T_{n-1}, T], \quad \boldsymbol{w}_n(T_{n-1}) = \boldsymbol{v}_{n-1}(T_{n-1}), \tag{3.14}$$

where $n = 1, 2, \ldots, N_t$ and $\boldsymbol{v}_0(T_0) = \boldsymbol{u}_0$. The exact solution $\boldsymbol{u}(t)$ can then be constructed by linearity from the decoupled red and blue solutions,

$$\boldsymbol{u}(t) = \boldsymbol{v}_n(t) + \sum_{j=1}^{n} \boldsymbol{w}_j(t), \quad t \in [T_{n-1}, T_n], \quad n = 1, 2, \ldots, N_t, \tag{3.15}$$

as one can see as follows: for $n = 1$, by adding (3.13) to (3.14) we have

$$(\boldsymbol{v}_1(t) + \boldsymbol{w}_1(t))' = A(\boldsymbol{v}_1(t) + \boldsymbol{w}_1(t)) + \boldsymbol{g}(t), \quad t \in (T_0, T_1], \quad (\boldsymbol{v}_1(0) + \boldsymbol{w}_1(0)) = \boldsymbol{u}_0.$$

This proves (3.15) for $n = 1$. Now, suppose (3.15) holds for n, and we thus have

$$\boldsymbol{u}(T_n) = \boldsymbol{v}_n(T_n) + \sum_{j=1}^{n} \boldsymbol{w}_j(T_n).$$

Then, in the next time interval $[T_n, T_{n+1}]$, since $\boldsymbol{w}_{n+1}(T_n) = \boldsymbol{v}_n(T_n)$, we have

$$\boldsymbol{u}(T_n) = \boldsymbol{w}_{n+1}(T_n) + \sum_{j=1}^{n} \boldsymbol{w}_j(T_n) = \sum_{j=1}^{n+1} \boldsymbol{w}_j(T_n).$$

Now, the function $\boldsymbol{w}(t)$ consisting of the first $n+1$ blue solutions, that is, $\boldsymbol{w}(t) = \sum_{j=1}^{n+1} \boldsymbol{w}_j(t)$ satisfies $\boldsymbol{w}'(t) = A\boldsymbol{w}(t)$ for $t \in (T_n, T_{n+1}]$ and $\boldsymbol{w}(T_n) = \boldsymbol{u}(T_n)$, and hence $\boldsymbol{w}(t)+\boldsymbol{v}_{n+1}(t)$ satisfies the underlying problem (2.1) for $t \in [T_n, T_{n+1}]$, which proves (3.15) for $n+1$.

As illustrated in Figure 3.7, the computation of the red and blue solutions can be done in parallel for all time intervals. But the computation of the blue problems (3.14) over longer and longer time intervals seems at first sight to be as expensive as the original problem (2.1). This is not the case, however, since the blue problems are homogeneous, i.e. without a source term, and their solution is given by a matrix exponential,

$$\boldsymbol{w}_n(t) = \exp((t - T_{n-1})A)\boldsymbol{v}_{n-1}(T_{n-1}), \quad t \in [T_{n-1}, T], \tag{3.16}$$

where the computation time of the product between the matrix exponential and the vector $\boldsymbol{v}_{n-1}(T_{n-1})$ is independent of the value of t. There are many efficient and mature computational tools to approximate such solutions over long times (Higham 2008, Moler and Van Loan 2003), such as rational Krylov methods and Chebyshev expansions, and also the scaling and squaring algorithm with a Padé approximation (i.e. the built-in command '`expmv`' in MATLAB_R2023b or later versions). This latter approach, however, is more suitable for smaller matrices; for large sparse matrices the former approaches should be used. With efficient computations of the matrix exponential, using ParaExp can achieve high parallel efficiencies, up to 80% for the time parallelization of the wave equation (2.7); see Gander and Güttel (2013). ParaExp is therefore an excellent time parallelization method for linear hyperbolic problems.

The ParaExp method described above is restricted to linear problems. An extension to nonlinear problems (2.2) was presented in Gander *et al.* (2018*a*), assuming that there is a linear part of the nonlinear term such as

$$f(\boldsymbol{u}(t), t) = A\boldsymbol{u}(t) + B(\boldsymbol{u}(t)) + \boldsymbol{g}(t). \tag{3.17}$$

Following the idea in the linear case, we decouple the nonlinear problem (3.17) into a linear problem $\boldsymbol{w}'(t) = A\boldsymbol{w}(t)$ with $\boldsymbol{w}(0) = \boldsymbol{u}_0$ and a nonlinear problem $\boldsymbol{v}'(t) = B(\boldsymbol{v}(t) + \boldsymbol{w}(t)) + \boldsymbol{g}(t)$ with zero initial value $\boldsymbol{v}(0) = 0$. The sum $\boldsymbol{u}(t) = \boldsymbol{w}(t) + \boldsymbol{v}(t)$ then still solves (3.17), but the problems on the time intervals are now coupled: in $\{[T_{n-1}, T_n]\}_{n=1}^{N_t}$, the initial value of $\boldsymbol{w}(t)$ at $t = T_{n-1}$ depends on $\boldsymbol{v}(T_{n-1})$. To obtain parallelism in time, we need to iterate by first solving in parallel the linear problems

$$\begin{aligned} (\boldsymbol{w}_n^k)'(t) &= A\boldsymbol{w}_n^k(t), & t &\in [T_{n-1}, T], \\ \boldsymbol{w}_n^k(T_{n-1}) &= \boldsymbol{v}_{n-1}^{k-1}(T_{n-1}), & \boldsymbol{w}_1^k(T_0) &= \boldsymbol{u}_0, \end{aligned}$$

and then solving in parallel the nonlinear problems

$$(\boldsymbol{v}_n^k)'(t) = A\boldsymbol{u}_n^k(t) + B(\boldsymbol{v}_n^k(t) + \sum_{j=1}^{n} \boldsymbol{w}_j^k(t)) + \boldsymbol{g}(t), \quad t \in [T_{n-1}, T_n],$$
$$\boldsymbol{u}_n^k(T_{n-1}) = 0,$$

where $n = 1, 2, \ldots, N_t$. The kth iterate solution is then defined by $\boldsymbol{u}_n^k(t) = \boldsymbol{v}_n^k(t) + \sum_{j=1}^{n} \boldsymbol{w}_j^k(t)$ for $t \in [T_{n-1}, T_n]$.

In the above nonlinear problems, the explicit dependence of B on $\sum_{j=1}^{n} \boldsymbol{w}_j^k(t)$ implies that we have to solve the linear problems on the entire interval $[T_{n-1}, T_n]$. This would be redundant and expensive if A were large. To avoid this, we reformulate the iteration by rewriting $\boldsymbol{v}_n^k(t)$ as $\boldsymbol{v}_n^k(t) = \boldsymbol{u}_n^k(t) - \sum_{j=1}^{n} \boldsymbol{w}_j^k(t)$. In this new nonlinear version of the ParaExp algorithm, we then solve for $n = 1, 2, \ldots, N_t$ sequentially,

$$\begin{aligned} (\boldsymbol{w}_n^k)'(t) &= A\boldsymbol{w}_n^k(t), \quad t \in [T_{n-1}, T], \\ \boldsymbol{w}_n^k(T_{n-1}) &= \boldsymbol{u}_{n-1}^{k-1}(T_{n-1}) - \sum_{j=1}^{n-1} \boldsymbol{w}_j^{k-1}(T_{n-1}), \quad \boldsymbol{w}_1^k(T_0) = \boldsymbol{u}_0, \end{aligned} \tag{3.18}$$

followed by solving in parallel the nonlinear problems

$$\begin{aligned} (\boldsymbol{u}_n^k)'(t) &= A\boldsymbol{u}_n^k(t) + B(\boldsymbol{u}_n^k(t)) + \boldsymbol{g}(t), \quad t \in [T_{n-1}, T_n], \\ \boldsymbol{u}_n^k(T_{n-1}) &= \sum_{j=1}^{n} \boldsymbol{w}_j^k(T_{n-1}), \end{aligned} \tag{3.19}$$

and finally we form the approximate solution at the kth iteration as

$$\boldsymbol{u}^k(t) = \boldsymbol{u}_n^k(t), \quad t \in [T_{n-1}, T_n].$$

The nonlinear ParaExp algorithm (3.18)–(3.19) has a finite step convergence property and a very interesting relation to the Parareal algorithm.

Theorem 3.4 (Gander *et al.* 2018*a*). The iterate $\boldsymbol{u}^k(t)$ at the kth iteration coincides with the exact solution $\boldsymbol{u}(t)$ for $t \in [0, T_k]$, that is, the iterative ParaExp method converges in a finite number of steps. Moreover, at each time point T_n, the iterate $\boldsymbol{u}^k(t)$ also coincides with the solution generated by the Parareal algorithm

$$\boldsymbol{U}_n^k = \mathcal{G}\left(T_{n-1}, T_n, \boldsymbol{U}_{n-1}^k\right) + \mathcal{F}\left(T_{n-1}, T_n, \boldsymbol{U}_{n-1}^{k-1}\right) - \mathcal{G}\left(T_{n-1}, T_n, \boldsymbol{U}_{n-1}^{k-1}\right), \tag{3.20a}$$

i.e. $\boldsymbol{u}_n^k = \boldsymbol{U}_n^k$ for $n = 0, 1, \ldots, N_t$, where the coarse propagator $\mathcal{G}(T_{n-1}, T_n, \boldsymbol{U})$ solves the linear problem

$$\boldsymbol{u}'(t) = A\boldsymbol{u}(t), \quad \boldsymbol{u}(T_{n-1}) = \boldsymbol{U}, \quad t \in [T_{n-1}, T_n], \tag{3.20b}$$

and the fine propagator $\mathcal{F}(T_{n-1}, T_n, \boldsymbol{U})$ solves the nonlinear problem

$$\boldsymbol{u}'(t) = A\boldsymbol{u}(t) + B(\boldsymbol{u}(t)) + \boldsymbol{g}(t), \quad \boldsymbol{u}(T_{n-1}) = \boldsymbol{U}, \quad t \in [T_{n-1}, T_n]. \tag{3.20c}$$

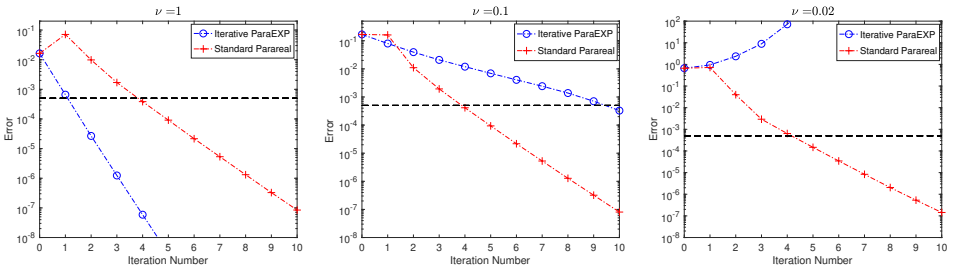

Figure 3.8. Convergence behaviour of ParaExp and standard Parareal for Burgers' equation with diffusion parameter ν changing from large to small. In each panel, the transverse line indicates the order of the truncation error, $\max\{\Delta t, \Delta x^2\}$, where in practice one would stop the iteration.

This is the first time we have seen the *Parareal* algorithm, which we will discuss in detail in Section 4. The Parareal algorithm (3.20a)–(3.20c) is a simplified version since, for the standard version, the coarse propagator $\mathcal{G}$ also solves (3.20c). As will be discussed in Section 4, the standard Parareal algorithm also does not perform well for hyperbolic problems, and thus we cannot expect the simplified version to work well in this case. An illustration of this aspect is shown in Figure 3.8 for (2.2) with

$$f(\boldsymbol{u}(t), t) = A\boldsymbol{u}(t) + B\boldsymbol{u}^2(t), \quad t \in (0, 2), \tag{3.21}$$

arising from semi-discretizing the one-dimensional Burgers' equation with periodic boundary conditions using centred finite differences with mesh size $\Delta x = \frac{1}{100}$, where $A = A_{\mathrm{xx}}$ and $B = -\frac{1}{2}A_{\mathrm{x}}$ with A_{xx} and A_{x} given in (3.12). For both ParaExp and Parareal, we use backward Euler for the fine solver $\mathcal{F}$ with a small step size $\Delta t = 0.01/20$. For Parareal, we use backward Euler for the coarse solver $\mathcal{G}$ as well, but with a larger step size $\Delta T = 0.01$. For ParaExp, we use the built-in solver `expmv` in MATLAB for the coarse propagator.

Clearly, for strongly diffusive problems, i.e. when ν is large, ParaExp converges very fast and the convergence rate is better than for standard Parareal. As ν decreases, standard Parareal converges faster than ParaExp, and particularly for $\nu = 0.02$, the latter diverges as shown in Figure 3.8(b). If we decrease ν further, then standard Parareal will also eventually diverge, and we will delve into this more in Section 4.

3.5. *ParaDiag*

The last technique we would like to explain is the ParaDiag family of methods, which is based on diagonalizing the time-stepping matrix (or its approximation). There are two variants of ParaDiag depending on how we treat the time-stepping matrix.

In the ParaDiag I family, which also represents a direct time-parallel solver like ParaExp, we diagonalize the time-stepping matrix and can then solve each time-step in parallel after diagonalization (Maday and Rønquist 2008). However, the diagonalization in ParaDiag I is only possible when either using variable time-step sizes, or using a different time-integrator for the last step compared to the others, as in boundary value methods. For the case of variable step sizes, a detailed error analysis (Gander *et al.* 2019) shows that we can only use a limited number of time-steps to parallelize, in double precision about 20, since we have to balance roundoff error with truncation error. Another shortcoming is that this direct ParaDiag method has only been explored for a few low-order time-integrators, such as backward Euler and the trapezoidal rule. ParaDiag I with variable time-step sizes is not easy to generalize to higher-order time-integrators, such as Runge–Kutta methods. When using a discretization of boundary value method type, the number of time-steps we can parallelize in a single time window is greatly improved, but again only backward Euler and the trapezoidal rule are applicable (Liu, Wang, Wu and Zhou 2022).

Both the limitations on the number of time-steps and the time-integrator are overcome by the ParaDiag II family (Gander *et al.* 2021*c*). The key idea is to design a suitable approximation of the time-stepping matrix and then to use it in a stationary iteration or as a preconditioner for a Krylov method, so we have to pay with iterations. The design principles for constructing such a preconditioner are twofold: its diagonalization should be well-conditioned, in contrast to the ParaDiag I family of methods (i.e. the condition number of its eigenvector matrix should be small), and the iterations should converge fast, i.e. have small spectral radius, or equivalently the spectrum of the preconditioned matrix should be tightly clustered around 1 for Krylov acceleration. The first design principle ensures that roundoff error arising from solving the preconditioning step via diagonalization is well controlled. The second design principle guarantees fast convergence of the preconditioned iteration. This iterative ParaDiag method was proposed in McDonald *et al.* (2018) and independently in Gander and Wu (2019). ParaDiag II techniques have been used as important components in new variants of Parareal and MGRiT which we will see in Sections 4.2 and 4.4, and which in their original form only work well for parabolic problems. ParaDiag II techniques enhance the new Parareal and MGRiT variants in two directions: they improve the speed-up by making the coarse grid correction parallel (Wu 2018, Wu and Zhou 2019), and they can also make Parareal and MGRiT work well for hyperbolic problems (Gander and Wu 2020) by allowing the coarse and fine propagators using the same grids, as we will show in Section 4.5. Use of ParaDiag II to solve the forward–backward system arising in PDE-constrained optimization can be found in Wu, Wang and Zhou (2023), Wu and Liu (2020) and Heinzelreiter and Pearson (2024), where ParaDiag II produces a parallel version of the matching Schur complement (MSC) preconditioner (Pearson, Stoll and Wathen 2012). Modifications and improvements of ParaDiag II can be found in Gander and Lunet (2024) and Liu and Wu (2022).

ParaDiag methods are applicable to both parabolic and hyperbolic problems, but the mechanisms for the direct and iterative versions are completely different. In the following, we introduce the main theory for these two versions and illustrate them with numerical results for the advection–diffusion equation (2.5), Burgers' equation (2.6) and the wave equation (2.7).

3.5.1. Direct ParaDiag methods (ParaDiag I)

Parallelization by diagonalization of the time-stepping matrix, originally introduced in Maday and Rønquist (2008), is based on a very simple idea: consider solving the initial value problem (2.1), i.e. $\boldsymbol{u}' = A\boldsymbol{u} + \boldsymbol{g}(t)$ with $A \in \mathbb{R}^{N_x \times N_x}$, by backward Euler with variable step sizes

$$\frac{\boldsymbol{u}_n - \boldsymbol{u}_{n-1}}{\Delta t_n} = A\boldsymbol{u}_n + \boldsymbol{g}_n, \quad n = 1, 2, \ldots, N_t, \tag{3.22}$$

with $\sum_{n=1}^{N_t} \Delta t_n = T$. Instead of solving these N_t difference equations one by one, we reformulate them as an *all-at-once* system, that is, we solve all the solution vectors collected in $\boldsymbol{U} := (\boldsymbol{u}_1^\top, \boldsymbol{u}_2^\top, \ldots, \boldsymbol{u}_{N_t}^\top)^\top$ in one shot,

$$\mathcal{K}\boldsymbol{U} = \boldsymbol{b}, \quad \mathcal{K} := B \otimes I_x - I_t \otimes A, \tag{3.23a}$$

where $\otimes$ is the Kronecker product, $I_x \in \mathbb{R}^{N_x \times N_x}$ and $I_t \in \mathbb{R}^{N_t \times N_t}$ are identity matrices, and B is the time-stepping matrix,

$$B = \begin{bmatrix} \frac{1}{\Delta t_1} & & & \\ -\frac{1}{\Delta t_2} & \frac{1}{\Delta t_2} & & \\ & \ddots & \ddots & \\ & & -\frac{1}{\Delta t_{N_t}} & \frac{1}{\Delta t_{N_t}} \end{bmatrix}, \quad \boldsymbol{b} = \begin{bmatrix} \frac{1}{\Delta t_1}\boldsymbol{u}_0 + \boldsymbol{g}_1 \\ \boldsymbol{g}_2 \\ \vdots \\ \boldsymbol{g}_{N_t} \end{bmatrix}. \tag{3.23b}$$

Since the time-steps $\{\Delta t_n\}$ are all different from each other, we can diagonalize B:

$$B = VDV^{-1}, \quad D = \operatorname{diag}\left(\frac{1}{\Delta t_1}, \frac{1}{\Delta t_2}, \ldots, \frac{1}{\Delta t_{N_t}}\right). \tag{3.24}$$

Then we can factor $\mathcal{K}$ in a blockwise manner as

$$\mathcal{K} = (V \otimes I_x)(D \otimes I_x - I_t \otimes A)(V^{-1} \otimes I_x).$$

This allows us to solve $\boldsymbol{U}$ from (3.23a) via the following three steps:

$$\begin{cases} \boldsymbol{U}^a = (V^{-1} \otimes I_x)\boldsymbol{b}, & \text{(step a)} \\ \left(\frac{1}{\Delta t_n} I_x - A\right)\boldsymbol{u}_n^b = \boldsymbol{u}_n^a, \quad n = 1, 2, \ldots, N_t, & \text{(step b)} \\ \boldsymbol{U} = (V \otimes I_x)\boldsymbol{u}^b, & \text{(step c)} \end{cases} \tag{3.25}$$

where

$$\boldsymbol{U}^a := \left(\left(\boldsymbol{u}_1^a\right)^\top, \ldots, \left(\boldsymbol{u}_{N_t}^a\right)^\top\right)^\top \quad \text{and} \quad \boldsymbol{U}^b := \left(\left(\boldsymbol{u}_1^b\right)^\top, \ldots, \left(\boldsymbol{u}_{N_t}^b\right)^\top\right)^\top.$$

Note that the first and last steps only involve matrix–vector multiplications and thus the computation is cheap. The major computation is step b, but interestingly, all the N_t linear systems stemming from the time-steps are independent and can be solved in parallel.

For an arbitrary choice of the step sizes $\{\Delta t_n\}$, we have to rely on numerical methods (e.g. `eig` in MATLAB) to obtain the eigenvector matrix V. This does not bring significant computational burden since N_t does not need to be very large in practice, but it prevents us from performing a complete analysis of the method, such as studying the roundoff error and the selection of the parameters involved. The time mesh used in Maday and Rønquist (2008) is a geometric mesh $\Delta t_n = \mu^{n-1}\Delta t_1$ with $\mu > 1$. They tested this direct time-parallel method with $\mu = 1.2$ for the heat equation in one dimension and obtained close-to-perfect speed-up.

For prescribed T, the constraint

$$\sum_{n=1}^{N_t} \Delta t_n = \sum_{n=1}^{N_t} \mu^{n-1}\Delta t_1 = T$$

specifies the first step size Δt_1 as

$$\Delta t_1 = \frac{T}{\sum_{n=1}^{N_t} \mu^{n-1}}.$$

This gives

$$\Delta t_n = \frac{\mu^{n-1}}{\sum_{n=1}^{N_t} \mu^{n-1}} T. \tag{3.26}$$

A large μ will produce large step sizes and thus large discretization error, while a small μ close to 1 produces large roundoff error when diagonalizing the time-stepping matrix B, which can be understood by noticing that as μ approaches 1, the time-stepping matrix B is close to a Jordan block, and diagonalizing such matrices results in large roundoff error. Therefore it is important to know how to fix μ by balancing the discretization and roundoff error. This was carefully studied in Gander *et al.* (2016*a*) for first-order parabolic problems, and in Gander *et al.* (2019) for the second-order wave equation. In what follows, we let $\mu = 1 + \varrho$, with $\varrho > 0$ being a small value, and we revisit the main existing results for fixing ϱ.

Theorem 3.5 (first-order problem). For the system of ODEs $\boldsymbol{u}' = A\boldsymbol{u} + \boldsymbol{g}$ with initial value $\boldsymbol{u}(0) = \boldsymbol{u}_0$ and $t \in [0, T]$, suppose $\sigma(A) \subset \mathbb{R}^-$ with $|\lambda(A)| \leq \lambda_{\max}$[2]. Let $\boldsymbol{u}_{N_t}(\varrho)$ and $\boldsymbol{u}_{N_t}(0)$ be the numerical solutions at $t = T$ obtained by using backward Euler with geometric step sizes and the uniform step size, respectively.

[2] Here and hereafter, $\lambda(\cdot)$ and $\sigma(\cdot)$ denote an arbitrary eigenvalue and the spectrum of the involved matrix.

Let $\{\tilde{\boldsymbol{u}}_n(\varrho)\}$ be the numerical solution computed by the diagonalization method (3.25). Then we obtain

$$\begin{aligned} \|\boldsymbol{u}_{N_t}(\varrho) - \boldsymbol{u}_{N_t}(0)\| &\lesssim C(\lambda_* T, N_t)\varrho^2, \\ \|\tilde{\boldsymbol{u}}_n(\varrho) - \boldsymbol{u}_n(\varrho)\| &\lesssim \epsilon \frac{N_t^2(2N_t+1)(N_t+\lambda_{\max}T)}{\phi(N_t)} \varrho^{-(N_t-1)}, \end{aligned} \tag{3.27}$$

where

$$C(x, N_t) \coloneqq \frac{N_t(N_t^2-1)}{24} r(x/N_t, N_t) \quad \text{with} \quad r(\tilde{x}, N_t) \coloneqq \left(\frac{\tilde{x}}{1+\tilde{x}}\right)^2 (1+\tilde{x})^{-N_t}.$$

Here ϵ is the machine precision[3] and

$$\phi(N_t) \coloneqq \begin{cases} \frac{N_t}{2}! \left(\frac{N_t}{2} - 1\right)!, & \text{if } N_t \text{ is even,} \\ \left(\frac{N_t - 1}{2}!\right)^2, & \text{if } N_t \text{ is odd.} \end{cases}$$

The quantity $\lambda_* \coloneqq N_t \tilde{x}_*/T$, where $\tilde{x}_*$ is the maximizer of the function $r(\tilde{x}, N_t)$ for $\tilde{x} \in [0, \infty)$. The best choice of ϱ, denoted by ϱ_{opt}, is the quantity balancing the two error bounds in (3.27), that is,

$$\varrho_{\text{opt}} = \left(\epsilon \frac{N_t^2(2N_t+1)(N_t+\lambda_{\max}T)}{\phi(N_t)C(\lambda_* T, N_t)}\right)^{1/(N_t+1)}. \tag{3.28}$$

Proof. Let $\lambda \in \sigma(A)$ be an arbitrary eigenvalue of A and consider the Dahlquist test equation $y' = \lambda y$. Then the first estimate in (3.27) follows from the analysis in Gander *et al.* (2016*a*, Theorem 2). For this test equation, the error due to diagonalization follows from the analysis in Gander *et al.* (2016*a*, Theorem 6) and the bound of the error reaches its maximum when $|\lambda| = \lambda_{\max}$. □

The first estimate in (3.27) presents the truncation error between the use of a geometric time mesh and a uniform time mesh. From this, we can estimate the truncation error between $\boldsymbol{u}_{N_t}(\varrho)$ and the exact solution $\boldsymbol{u}(T)$ as

$$\|\boldsymbol{u}_{N_t}(\varrho) - \boldsymbol{u}(T)\| \le \|\boldsymbol{u}_{N_t}(\varrho) - \boldsymbol{u}_{N_t}(0)\| + \|\boldsymbol{u}_{N_t}(0) - \boldsymbol{u}(T)\|,$$

where the estimate of the last term is well understood and does not play a dominant role. The second estimate in (3.27) is the roundoff error due to diagonalization of the time-stepping matrix B. The analysis of this error is closely related to the condition number of the eigenvector matrix V. With the geometric step sizes in

[3] In the ISO C Standard, $\epsilon = 1.19 \times 10^{-7}$ for single precision and $\epsilon = 2.22 \times 10^{-16}$ for double precision.

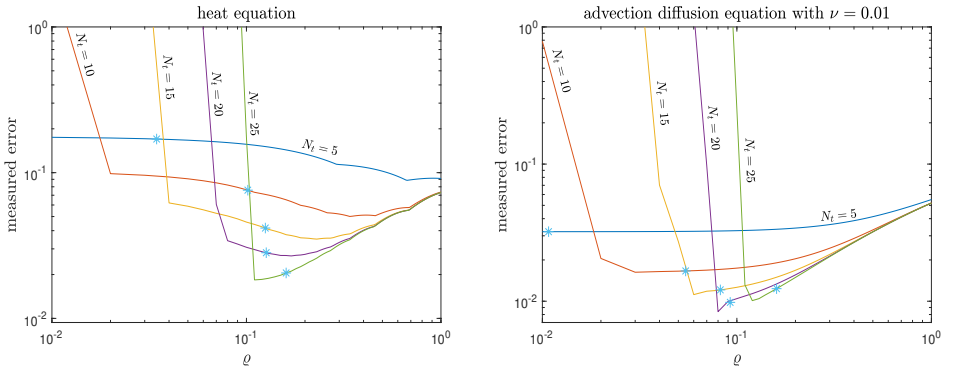

Figure 3.9. Measured error of ParaDiag I for five values of N_t using geometric step sizes as in (3.26) with $\mu = 1 + \varrho$ and $\varrho \in [10^{-2}, 1]$. The star denotes the theoretically estimated ϱ_{opt} from (3.28).

(3.26), V and V^{-1} are lower triangular Toeplitz matrices (see Gander *et al.* 2016*a*),

$$V = \mathbb{T}(p_1, p_2, \ldots, p_{N_t-1}), \quad p_n := \frac{1}{\prod_{j=1}^{n}(1-\varrho^j)}, \qquad (3.29a)$$
$$V^{-1} = \mathbb{T}(q_1, q_2, \ldots, q_{N_t-1}), \quad q_n = (-1)^n \varrho^{n(n-1)/2} p_n,$$

where $\mathbb{T}$ is the lower triangular Toeplitz operator

$$\mathbb{T}(a_1, a_2, \ldots, a_{N_t}) = \begin{bmatrix} 1 & & & \\ a_1 & 1 & & \\ \vdots & \ddots & \ddots & \\ a_{N_t-1} & \ldots & a_1 & 1 \end{bmatrix}. \qquad (3.29b)$$

The closed-form formula for V and V^{-1} in (3.29a) is useful for estimating $\text{Cond}(V)$, and then the roundoff error in (3.27). However, in practice we do not use these formulas for V and V^{-1} in (3.25). Instead we use the command `eig` in MATLAB to get V and V^{-1}, since it automatically optimizes the condition number by scaling the eigenvectors.

We now study the error of the ParaDiag I method for two PDEs with homogeneous Dirichlet boundary conditions and the initial value $u(x, 0) = \sin(2\pi x)$ for $x \in (0, 1)$, the heat equation (2.3) and the advection–diffusion equation (2.5) with $\nu = 10^{-2}$. Both PDEs are discretized by centred finite differences with mesh size $\Delta x = \frac{1}{50}$. With $T = 0.2$ and five values of N_t, Figure 3.9 shows the error of ParaDiag I for $\varrho \in [10^{-2}, 1]$. The error is measured as $\max_{n=1,2,\ldots,N_t} \|\tilde{\boldsymbol{u}}_n(\varrho) - \boldsymbol{u}(t_n)\|_\infty$, where $\boldsymbol{u}(t_n)$ is the reference solution computed by the exponential integrator, that is, $\boldsymbol{u}(t_n) = \mathrm{e}^{-At_n}\boldsymbol{u}_0$ and $\tilde{\boldsymbol{u}}_n(\varrho)$ is the solution at $t = t_n$ by ParaDiag I. Clearly there exists an optimal choice of ϱ that minimizes the error. We also use a star to show for each N_t the theoretically estimated ϱ_{opt} from (3.28). For the advection–

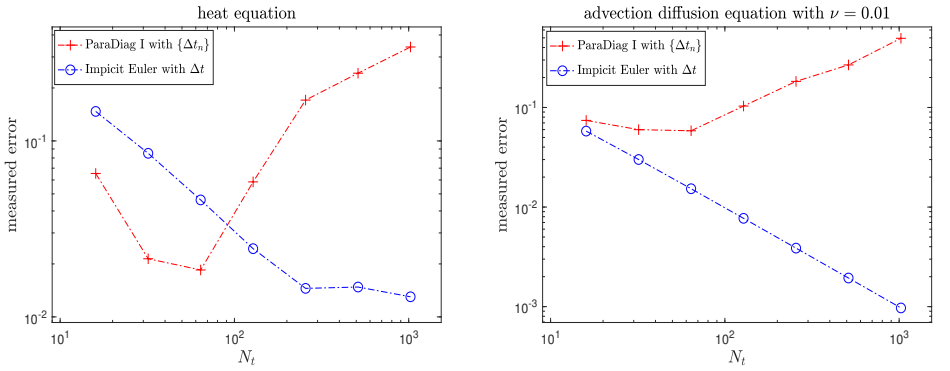

Figure 3.10. The error of ParaDiag I increases rapidly for N_t exceeding a threshold when using $\mu = 1 + \varrho_{\text{num}}$.

diffusion equation, this ϱ_{opt} predicts the optimal choice very well, and also quite well for the heat equation, except when N_t is small, even though the theoretical estimate was just obtained by balancing roundoff and truncation error estimates asymptotically. Let ϱ_{num} be the minimizer determined numerically, as shown in Figure 3.9. In Figure 3.10 we show the error for backward Euler with uniform step size $\Delta t = T/N_t$ and the ParaDiag I method using variable step sizes Δt_n, i.e. (3.26) with $\mu = 1 + \varrho_{\text{num}}$. Here $T = 0.5$ and $N_t = 2^{4:10}$. As N_t grows, the error for ParaDiag I decreases first and then increases rapidly when N_t exceeds some threshold less than 100.

We next consider a second-order problem, e.g. the wave equation (2.7) after space discretization,

$$\boldsymbol{u}''(t) = A\boldsymbol{u}(t) \quad \text{for } t \in (0,T], \quad \boldsymbol{u}(0) = \boldsymbol{u}_0, \quad \boldsymbol{u}'(0) = \tilde{\boldsymbol{u}}_0, \tag{3.30}$$

where $A \in \mathbb{R}^{N_x \times N_x}$. For the wave equation (2.7), A is a discretized Laplacian. To use ParaDiag I, we transform this equation into a first-order system,

$$\boldsymbol{w}'(t) = \boldsymbol{A}\boldsymbol{w}(t) \quad \text{for } t \in (0,T], \quad \boldsymbol{w}(0) = (\boldsymbol{u}_0^\top, \tilde{\boldsymbol{u}}_0^\top)^\top, \tag{3.31}$$

where $\boldsymbol{w}(t) = (\boldsymbol{u}^\top(t), (\boldsymbol{u}'(t))^\top)^\top$ and

$$\boldsymbol{A} = \begin{bmatrix} & I_x \\ A & \end{bmatrix}.$$

To avoid numerical dispersion, we use the trapezoidal rule as the time-integrator,

$$\frac{\boldsymbol{w}_n - \boldsymbol{w}_{n-1}}{\Delta t_n} = \frac{\boldsymbol{A}}{2}(\boldsymbol{w}_n + \boldsymbol{w}_{n-1}), \quad n = 1, 2, \ldots, N_t, \tag{3.32}$$

which is energy-preserving in the sense that $\|\boldsymbol{w}_n\|_2 = \|\boldsymbol{w}_0\|_2$. The step sizes $\{\Delta t_n\}$ are again geometric as in (3.26) with some parameter $\mu = 1 + \varrho > 1$. Similarly to

(3.23a), we can represent (3.32) as an all-at-once system,

$$\mathcal{K}\boldsymbol{W} = \boldsymbol{b}, \quad \mathcal{K} = B \otimes I_x - \tilde{B} \otimes A, \tag{3.33a}$$

with some suitable vector $\boldsymbol{b}$, where B is the matrix in (3.23b) and

$$\tilde{B} = \frac{1}{2}\begin{bmatrix} 1 & & & \\ 1 & 1 & & \\ & \ddots & \ddots & \\ & & 1 & 1 \end{bmatrix}. \tag{3.33b}$$

To apply the diagonalization technique, we rewrite (3.33a) as

$$\mathcal{K}\boldsymbol{W} = \tilde{\boldsymbol{b}}, \quad \mathcal{K} = \tilde{B}^{-1}B \otimes I_x - I_t \otimes A, \quad \tilde{\boldsymbol{b}} = (\tilde{B}^{-1} \otimes I_x)\boldsymbol{b}. \tag{3.34}$$

The matrix $\tilde{B}^{-1}B$ can be diagonalized (see Gander *et al.* 2019),

$$\tilde{B}^{-1}B = V \operatorname{diag}\left(\frac{2}{\Delta t_1}, \ldots, \frac{2}{\Delta t_{N_t}}\right) V^{-1}, \tag{3.35a}$$

where V and V^{-1} are given by

$$\begin{aligned} V &= \mathbb{T}(p_1, p_2, \ldots, p_{N_t-1}), \quad p_n := \prod_{j=1}^{n} \frac{1+\mu^j}{1-\mu^j}, \\ V^{-1} &= \mathbb{T}(q_1, q_2, \ldots, q_{N_t-1}), \quad q_n := \mu^{-n} \prod_{j=1}^{n} \frac{1+\mu^{-j+2}}{1-\mu^{-j}}. \end{aligned} \tag{3.35b}$$

Then the all-at-once system (3.34) can be solved via ParaDiag I (see (3.25)) as well.

Similarly to the first-order equation studied above, by balancing the truncation error (between the geometric mesh and the uniform mesh) and the roundoff error, the best mesh parameter $\mu = 1 + \varrho_{\text{opt}}$ is obtained as follows.

Theorem 3.6 (second-order problem). For the second-order system of ODEs $\boldsymbol{u}'' = A\boldsymbol{u}$ with $\lambda(A) \le 0$, let $\boldsymbol{u}_{N_t}(\varrho)$ and $\boldsymbol{u}_{N_t}(0)$ denote the numerical solutions at $t = T$ obtained by using the trapezoidal rule with geometric time-step sizes and the uniform time-step size. Let $\{\tilde{\boldsymbol{u}}_n(\varrho)\}$ denote the numerical solution computed by the diagonalization method (3.25). Then we obtain

$$\begin{aligned} \|\boldsymbol{u}_{N_t}(\varrho) - \boldsymbol{u}_{N_t}(0)\| &\lesssim \frac{N_t(N_t^2-1)}{15}\varrho^2, \\ \|\tilde{\boldsymbol{u}}_n(\varrho) - \boldsymbol{u}_n(\varrho)\| &\lesssim \epsilon \frac{2^{2N_t-1/2}N_t}{(N_t-1)!}\varrho^{-(N_t-1)}. \end{aligned} \tag{3.36}$$

The best choice of ϱ, denoted by ϱ_{opt}, is the quantity balancing the two error bounds in (3.36), that is,

$$\varrho_{\text{opt}} = \left(\epsilon \frac{15 \times 2^{2N_t-1/2}}{(N_t^2-1)(N_t-1)!}\right)^{1/(N_t+1)}. \tag{3.37}$$

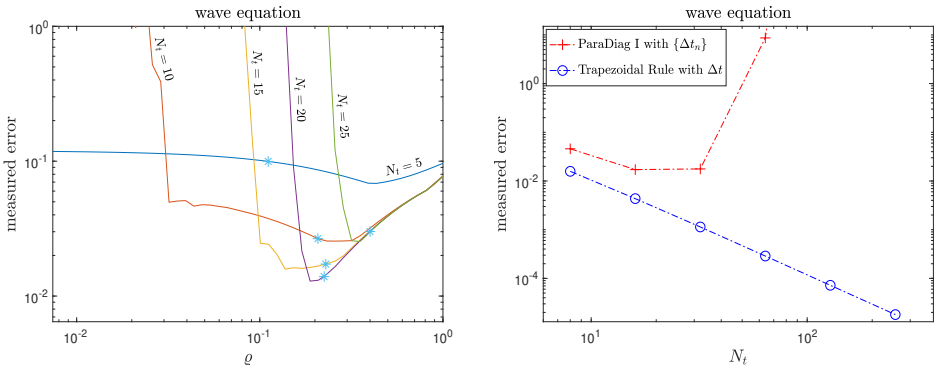

(a) (b)

Figure 3.11. Measured error of ParaDiag I and the trapezoidal rule using uniform step sizes for the wave equation (2.7). The star in (a) is the parameter ϱ_{opt} obtained in theory (see (3.37)).

Proof. Let $\lambda > 0$ be an arbitrary eigenvalue of $-A$ and consider the scalar equation $u'' + \lambda u = 0$. Then, for small ϱ, according to Gander *et al.* (2019, Theorem 2.1), the truncation error between using the geometric mesh and the uniform mesh is of order

$$O\left(\frac{N_t(N_t^2-1)}{6} r_1\left(\frac{\lambda T}{2N_t}\right)\varrho^2\right) \quad \text{with } r_1(s) = \frac{s^3}{(1+s^2)^2}.$$

For $s \geq 0$ we have $r_1(s) \leq \frac{2}{5}$, and this gives the first estimate in (3.36). The second estimate follows from the roundoff error analysis in Gander *et al.* (2019, Theorem 2.11), which is

$$\frac{2^{2N_t-1/2}N_t}{(N_t-1)!} r_2\left(\frac{\lambda T}{2N_t}\right) \quad \text{with } r_2(s) = \frac{1}{1+s^2}.$$

For $s \geq 0$ we have $r_2(s) \leq 1$. □

In Figure 3.11(a) we show the error of ParaDiag I for five values of N_t when applied to the wave equation (2.7) with homogeneous Dirichlet boundary conditions. For each N_t, the parameter ϱ varies from 10^{-2} to 1. Here, $\Delta x = \frac{1}{20}$ and $T = 0.2$. Similarly to the first-order parabolic problems (see Figure 3.9), there exists an optimal choice of ϱ which minimizes the error, and the theoretical estimate ϱ_{opt} is close to this choice. With ϱ_{num} denoting the best working parameter determined numerically for each N_t, Figure 3.11(b) shows the error for the geometric time mesh and the uniform time mesh. For the former, the error grows rapidly when $N_t > 32$.

For ParaDiag I, the increase in the error shown in Figures 3.10 and 3.11(b) can be attributed to the poor condition number of the eigenvector matrix V of the time-step matrices B and $\tilde{B}^{-1}B$. In Table 3.1 we show this condition number for several

Table 3.1. Cond(V) for B (backward Euler) and $\tilde{B}^{-1}B$ (trapezoidal rule).

N_t	5	10	20	30	60	100
B	1.7×10^3	8.4×10^4	1.3×10^6	2.8×10^6	4.4×10^6	4.8×10^6
$\tilde{B}^{-1}B$	4.7×10^3	7.9×10^5	6.9×10^7	3.8×10^8	1.9×10^9	4.1×10^9

values of N_t, where $\mu = 1 + \varrho_{\text{num}}$, and ϱ_{num} is determined numerically for each N_t by minimizing the error shown in Figures 3.9 and 3.11(a). As N_t increases, the condition number rises rapidly, which confirms our analysis of roundoff error very well (see (3.27) and (3.36)), but then reaches a plateau when using the numerically optimized parameter and not the theoretically determined one, an observation that merits further study.

We now introduce another ParaDiag I method from Liu *et al.* (2022), which addresses the limitation associated with N_t. Instead of using backward Euler or the trapezoidal rule with geometric time-step sizes, we use the same time-step size Δt but different methods, an idea which goes back to the boundary value technique (Axelsson and Verwer 1985). In this approach, we take, for example, centred finite differences for the first $(N_t - 1)$ time-steps, followed by a final backward Euler step. For the system of ODEs (2.1), this gives

$$\begin{cases} \dfrac{\boldsymbol{u}_{n+1} - \boldsymbol{u}_{n-1}}{2\Delta t} = A\boldsymbol{u}_n + \boldsymbol{g}_n, & n = 1, 2, \ldots, N_t - 1, \\ \dfrac{\boldsymbol{u}_{N_t} - \boldsymbol{u}_{N_t-1}}{\Delta t} = A\boldsymbol{u}_{N_t} + \boldsymbol{g}_{N_t}. \end{cases} \tag{3.38}$$

It is important to note that this implicit boundary value technique time discretization has quite different stability properties from traditional time discretizations; see e.g. Gander (2015, Section 5.2). For the boundary value technique discretization (3.38), the all-at-once system is

$$\mathcal{K}\boldsymbol{U} = \boldsymbol{b}, \quad \mathcal{K} = B \otimes I_x - I_t \otimes A, \tag{3.39a}$$

where

$$B = \frac{1}{\Delta t}\begin{bmatrix} 0 & \frac{1}{2} & & & \\ -\frac{1}{2} & 0 & \frac{1}{2} & & \\ & \ddots & \ddots & \ddots & \\ & & -\frac{1}{2} & 0 & \frac{1}{2} \\ & & & -1 & 1 \end{bmatrix}, \quad \boldsymbol{b} = \begin{bmatrix} \frac{\boldsymbol{u}_0}{2\Delta t} + \boldsymbol{g}_1 \\ \boldsymbol{g}_2 \\ \vdots \\ \boldsymbol{g}_{N_t} \end{bmatrix}. \tag{3.39b}$$

For the all-at-once system given by equation (3.39a), only the initial value $\boldsymbol{u}_0$ is required, and all time-steps are solved simultaneously in one shot.

Axelsson and Verwer (1985) explored boundary value techniques to circumvent the well-known Dahlquist barriers between convergence and stability, which arise when using (3.38) in a time-stepping mode. In a general nonlinear case, they proved that the numerical solutions obtained simultaneously are of uniform second-order accuracy (Axelsson and Verwer 1985, Theorem 4), even though the last step is a first-order scheme. Even earlier, in Fox (1954) and also Fox and Mitchell (1957), such boundary value technique discretizations had already appeared: instead of backward Euler, the authors used the BDF2 method for the last step in (3.38),

$$\frac{3\boldsymbol{u}_{N_t} - 4\boldsymbol{u}_{N_t-1} + \boldsymbol{u}_{N_t-2}}{2\Delta t} = A\boldsymbol{u}_{N_t} + \boldsymbol{g}_{N_t}.$$

The method (3.38) is a prime example of the so-called *boundary value methods* (BVMs) developed a bit later, and the all-at-once system (3.39a) was carefully justified in Brugnano, Mazzia and Trigiante (1993); see also Brugnano and Trigiante (2003). In BVMs, the resulting all-at-once system is typically solved iteratively by constructing effective preconditioners.

A mathematical analysis of ParaDiag I based on BVM discretization like (3.38) can be found in Liu *et al.* (2022).

Theorem 3.7. The time-stepping matrix B given by (3.39b) can be factored as $B = VDV^{-1}$ with $\mathrm{Cond}(V) = O(N_t^2)$[4].

ParaDiag I with BVM discretization can also be applied to second-order problems of the form $\boldsymbol{u}'' = A\boldsymbol{u}$, with initial values $\boldsymbol{u}(0) = \boldsymbol{u}_0$ and $\boldsymbol{u}'(0) = \tilde{\boldsymbol{u}}_0$. By setting $\boldsymbol{v}(t) := \boldsymbol{u}'(t)$ and $\boldsymbol{w}(t) := (\boldsymbol{u}^\top(t), \boldsymbol{v}^\top(t))^\top$, we can rewrite this equation as

$$\boldsymbol{w}'(t) = \boldsymbol{A}\boldsymbol{w}(t), \quad \boldsymbol{A} := \begin{bmatrix} & I_x \\ A & \end{bmatrix}, \quad \boldsymbol{w}(0) := \begin{bmatrix} \boldsymbol{u}_0 \\ \tilde{\boldsymbol{u}}_0 \end{bmatrix}.$$

Then, similarly to (3.38), the same time discretization scheme leads to

$$\begin{cases} \dfrac{\boldsymbol{w}_{n+1} - \boldsymbol{w}_{n-1}}{2\Delta t} = \boldsymbol{A}\boldsymbol{w}_n, \quad n = 1, 2, \ldots, N_t - 1, \\ \dfrac{\boldsymbol{w}_{N_t} - \boldsymbol{w}_{N_t-1}}{\Delta t} = \boldsymbol{A}\boldsymbol{w}_{N_t}. \end{cases} \tag{3.40}$$

Rewriting the second-order problem as a first-order system doubles the storage requirement for the space variables at each time point, which is not desirable, especially if the second-order problem arises from a semi-discretization of a PDE in high dimensions or with small mesh sizes. To avoid this, one can write the all-at-once system for (3.40) using only $\boldsymbol{U} := (\boldsymbol{u}_1, \boldsymbol{u}_2, \ldots, \boldsymbol{u}_{N_t})^\top$, which leads to

$$(B^2 \otimes I_x - I_t \otimes A)\boldsymbol{U} = \boldsymbol{b}, \tag{3.41}$$

[4] Closed-form formulas for V, V^{-1}, and D are provided in Liu *et al.* (2022, Section 3).

where B is the matrix defined in (3.39b), and

$$\boldsymbol{b} := \left(\frac{\tilde{\boldsymbol{u}}_0^\top}{2\Delta t}, -\frac{\boldsymbol{u}_0^\top}{4\Delta t^2}, 0, \ldots, 0\right)^\top.$$

To see this, we trace back the steps at the discrete level which led to the first-order system at the continuous level: from (3.40) we represent $\{\boldsymbol{u}_n\}$ and $\{\boldsymbol{v}_n\}$ separately as

$$\begin{cases} \dfrac{\boldsymbol{u}_{n+1} - \boldsymbol{u}_{n-1}}{2\Delta t} = \boldsymbol{v}_n, \ n = 1, 2, \ldots, N_t - 1, \\ \dfrac{\boldsymbol{u}_{N_t} - \boldsymbol{u}_{N_t-1}}{\Delta t} = \boldsymbol{v}_{N_t}, \end{cases}$$

$$\begin{cases} \dfrac{\boldsymbol{v}_{n+1} - \boldsymbol{v}_{n-1}}{2\Delta t} = A\boldsymbol{u}_n, \ n = 1, 2, \ldots, N_t - 1, \\ \dfrac{\boldsymbol{v}_{N_t} - \boldsymbol{v}_{N_t-1}}{\Delta t} = A\boldsymbol{u}_{N_t}. \end{cases}$$

Hence, with the matrix B in (3.39b), we have

$$(B \otimes I_x)\boldsymbol{U} - \boldsymbol{V} = \boldsymbol{b}_1, \quad (B \otimes I_x)\boldsymbol{V} - A\boldsymbol{U} = \boldsymbol{b}_2,$$

where

$$\boldsymbol{V} := (\boldsymbol{v}_1^\top, \ldots, \boldsymbol{v}_{N_t}^\top)^\top, \quad \boldsymbol{b}_1 := \left(\frac{\boldsymbol{u}_0^\top}{2\Delta t}, 0, \ldots, 0\right)^\top \text{ and } \quad \boldsymbol{b}_2 := \left(\frac{\tilde{\boldsymbol{u}}_0^\top}{2\Delta t}, 0, \ldots, 0\right)^\top.$$

From the first equation, we have $\boldsymbol{V} = (B \otimes I_x)\boldsymbol{U} - \boldsymbol{b}_1$. Substituting this into the second equation gives $(B \otimes I_x)^2\boldsymbol{U} - A\boldsymbol{U} = \boldsymbol{b}_2 + (B \otimes I_x)\boldsymbol{b}_1$. A routine calculation then yields $\boldsymbol{b}_2 + (B \otimes I_x)\boldsymbol{b}_1 = \boldsymbol{b}$, and combining this with $(B \otimes I_x)^2 = B^2 \otimes I_x$ gives the all-at-once system (3.41).

We now compare the ParaDiag I method with geometric time-stepping to the method with BVM discretization applied to the wave equation (2.7) with homogeneous Dirichlet boundary conditions and $T = 0.5$, discretized in space using centred finite differences with $\Delta x = \frac{1}{40}$. The errors for $N_t = 2^2$ to 2^8 are shown in Figure 3.12(a). We see that the error of ParaDiag I with geometric time-stepping shows the typical deterioration due to roundoff around $N_t = 32$, whereas ParaDiag I with BVM discretization is of order $O(\Delta t^2)$ without any deterioration, like the trapezoidal rule. In Figure 3.12(b) we show the corresponding condition number of the eigenvector matrix of the time-step matrix, which shows that ParaDiag I with BVM discretization has a much lower condition number and explains why we do not observe any deterioration.

To conclude this section, we show how to apply ParaDiag I to nonlinear problems. We consider the first-order nonlinear system of ODEs (2.2), i.e. $\boldsymbol{u}'(t) = f(\boldsymbol{u}(t), t)$ with initial value $\boldsymbol{u}(0) = \boldsymbol{u}_0$, nonlinear second-order problems can be treated similarly. As in the linear case, the all-at-once system for this nonlinear problem is

$$(B \otimes I_x)\boldsymbol{U} - F(\boldsymbol{U}) = \boldsymbol{b}, \tag{3.42}$$

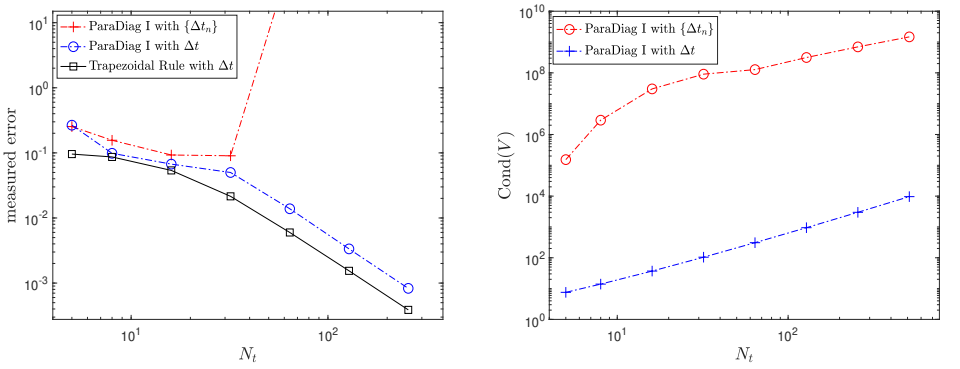

(a) (b)

Figure 3.12. (a) Measured error for the wave equation (2.7) using ParaDiag I with the trapezoidal rule and geometric step sizes $\{\Delta t_n\}$ and the BVM discretization (3.38) with uniform time-step $\Delta t = T/N_t$. (b) Condition number of the eigenvector matrix of the time-stepping matrix.

where $F(\boldsymbol{U}) := (f^\top(\boldsymbol{u}_1, t_1), f^\top(\boldsymbol{u}_2, t_2), \ldots, f^\top(\boldsymbol{u}_{N_t}, t_{N_t}))^\top$, and $\boldsymbol{b}$ is a suitable right-hand side vector containing the initial condition and possible terms not depending on the solution. The time-step matrix B is either the one given in (3.23b) using variable time-steps, or the one given in (3.39b) corresponding to the BVM discretization (3.38).

Since the problem (3.42) is nonlinear, we apply Newton's method,

$$(B \otimes I_x - \nabla F(\boldsymbol{U}^k))(\boldsymbol{U}^{k+1} - \boldsymbol{U}^k) = \boldsymbol{b} - ((B \otimes I_x)\boldsymbol{U}^k - F(\boldsymbol{U}^k)),$$

which can be simplified to

$$(B \otimes I_x - \nabla F(\boldsymbol{U}^k))\boldsymbol{U}^{k+1} = \boldsymbol{b} - (\nabla F(\boldsymbol{U}^k)\boldsymbol{U}^k - F(\boldsymbol{U}^k)), \tag{3.43a}$$

where $k \geq 0$ is the Newton iteration index, and

$$\nabla F(\boldsymbol{U}^k) = \text{blkdiag}\big(\nabla f\big(\boldsymbol{u}_1^k, t_1\big), \ldots, \nabla f\big(\boldsymbol{u}_{N_t}^k, t_{N_t}\big)\big), \tag{3.43b}$$

with $\nabla f(\boldsymbol{u}_n^k, t_n)$ being the Jacobian matrix of $f(\boldsymbol{u}, t_n)$ with respect to the first variable $\boldsymbol{u}$. To make the diagonalization technique still applicable, we have to replace (or approximate) all the blocks $\{\nabla f(\boldsymbol{u}_n^k, t_n)\}$ by a single matrix A_k. Inspired by the idea in Gander and Halpern (2017), we consider an averaged Jacobian matrix,

$$A_k := \frac{1}{N_t}\sum_{n=1}^{N_t} \nabla f(\boldsymbol{u}_n^k, t_n) \quad \text{or} \quad A_k := \nabla f\left(\frac{1}{N_t}\sum_{n=1}^{N_t} \boldsymbol{u}_n^k, \frac{T}{N_t}\right). \tag{3.44}$$

Then we get a simple Kronecker-product approximation of $\nabla F(\boldsymbol{U}^k)$ as

$$\nabla F(\boldsymbol{U}^k) \approx I_t \otimes A_k.$$

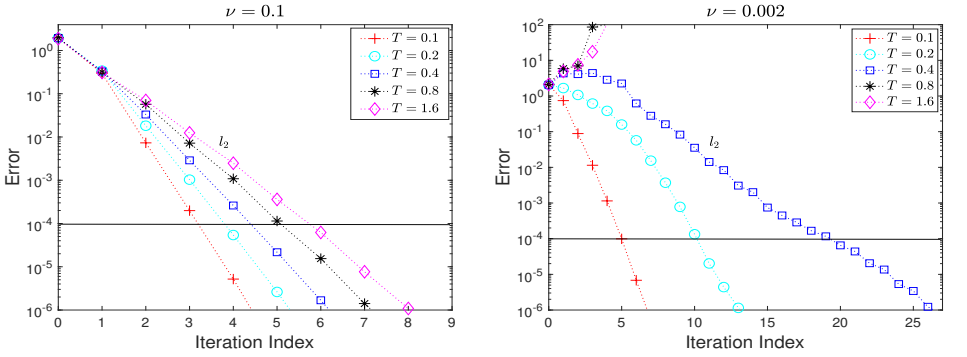

(a) (b)

Figure 3.13. Error of ParaDiag I with BVM discretization (3.38) for Burgers' equation (2.6) with two values of the diffusion parameter ν. For each value of T, the number of time-steps is fixed to $N_t = T/\Delta t = 200$. The horizontal line denotes the approximate space–time discretization error $\max\{\Delta t^2, \Delta x^2\} = 10^{-4}$.

By substituting this into (3.43a), we obtain the quasi-Newton method

$$(B \otimes I_x - I_t \otimes A_k)\boldsymbol{U}^{k+1} = \boldsymbol{b} - ((I_t \otimes A_k)\boldsymbol{U}^k - F(\boldsymbol{U}^k)). \tag{3.45}$$

Convergence of such quasi-Newton methods is well understood; see e.g. Deuflhard (2004, Theorem 2.5) and Ortega and Rheinboldt (2000).

In this quasi-Newton method (3.45), the Jacobian system can also be solved parallel in time: with the diagonalization $B = VDV^{-1}$, we solve $\boldsymbol{U}^{k+1}$ in (3.45) again in three steps,

$$\begin{cases} \boldsymbol{U}^a = (V^{-1} \otimes I_x)\boldsymbol{r}^k, & \text{(step a)} \\ (\lambda_n I_x - A_k)\boldsymbol{u}_n^b = \boldsymbol{u}_n^a, \ n = 1, 2, \ldots, N_t, & \text{(step b)} \\ \boldsymbol{U}^{k+1} = (V \otimes I_x)\boldsymbol{U}^b, & \text{(step c)} \end{cases} \tag{3.46}$$

where $\boldsymbol{r}^k := \boldsymbol{b} - ((I_t \otimes A_k)\boldsymbol{U}^k - F(\boldsymbol{U}^k)$. In the linear case, i.e. $f(\boldsymbol{u}, t) = A\boldsymbol{u} + \boldsymbol{g}(t)$, we have $A_k = A$ and $\boldsymbol{r}^k = \boldsymbol{b}$, and (3.46) reduces to (3.25).

The convergence rate of the quasi-Newton method depends on the accuracy of the approximation of the average matrix A_k to all N_t Jacobian blocks $\nabla f(\boldsymbol{u}_n^k, t_n)$. One can imagine that if $\nabla f(u_n^k, t_n)$ changes dramatically for $n = 1, 2, \ldots, N_t$, any single matrix cannot be a good approximation. In this case we can divide the time interval $[0, T]$ into multiple smaller windows and apply ParaDiag I to these time windows sequentially. We tested this approach by combining ParaDiag I with the BVM discretization (3.38) for Burgers' equation (2.6) with periodic boundary conditions. We discretized in space using centred finite differences with mesh size $\Delta x = 0.01$. In time, both the time-step size Δt and the length of the time interval T were varied simultaneously, maintaining a fixed number of time-steps, $N_t = T/\Delta t = 200$. In Figure 3.13, we present the convergence histories for two

Table 3.2. Number of total Jacobian solves for the sequential trapezoidal rule and ParaDiag I with BVM discretization in parallel.

	T	0.1	0.2	0.4	0.8	1.6
$\nu = 0.1$	trapezoidal rule	401	401	403	419	443
	ParaDiag I	5	5	6	7	7
$\nu = 0.002$	trapezoidal rule	400	446	476	460	526
	ParaDiag I	7	12	22	×	×

values of the diffusion parameter ν and several values of T. Note the dependence of the convergence rate on T, especially when ν is small. For $\nu = 0.1$, ParaDiag I has similar convergence rates when T increases, indicating that the Jacobian matrix $\nabla f(u,t)$ has smaller variations for $(t,u) \in \{(t_1,u_1),(t_2,u_n),\ldots,(t_{N_t},u_{N_t})\}$.

The major computation in ParaDiag I is solving the N_t independent Jacobian systems in step b of (3.46). Assuming the method reaches the stopping criterion after k iterations, the total number of Jacobian solves is k, given that we have access to N_t processors and each of them handles one Jacobian system in step b. On the other hand, in a time-stepping mode, we would need to solve $\sum_{n=1}^{N_t} \mathrm{It}_n$ Jacobian systems, where It_n represents the number of Newton iterations performed at the nth time-step. Table 3.2 shows a comparison of the total number of parallel Jacobian solves in ParaDiag I with BVM discretization, and when using the trapezoidal rule sequentially. We see the clear computational advantage of ParaDiag I with BVM discretization, especially when convergence is rapid.

An idea recently proposed in Liu and Wu (2022, Section 3.3) to accelerate nonlinear ParaDiag II, which we will see in the next section, can also be used to accelerate nonlinear ParaDiag I: instead of using a single matrix A_k to approximate all the blocks $\{\nabla f(\boldsymbol{u}_n^k, t_n)\}$ (see (3.44)), we approximate $\nabla F(\boldsymbol{U}^k)$ by using a tensor structure matrix $\Phi_k \otimes A_k$ with a diagonal matrix Φ_k determined by minimizing

$$\min_{\Phi_k = \mathrm{diag}(\phi_1,\phi_2,\ldots,\phi_{N_t})} \|\nabla F(\boldsymbol{U}^k) - \Phi_k \otimes A_k\|, \tag{3.47}$$

where A_k is the averaging matrix given in (3.44). For the Frobenius norm $\|\cdot\|_F$, the solution of this minimization problem is known as the *nearest Kronecker product approximation* (NKA), given by Van Loan and Pitsianis (1993, Theorem 3),

$$\phi_n = \frac{\mathrm{trace}\big(\big(\nabla f\big(\boldsymbol{u}_n^k, t_n\big)\big)^\top A_k\big)}{\mathrm{trace}\big(A_k^\top A_k\big)}, \quad n = 1,2,\ldots,N_t, \tag{3.48}$$

under the assumption that $\mathrm{trace}\big(A_k^\top A_k\big) > 0$. This leads to the quasi-Newton

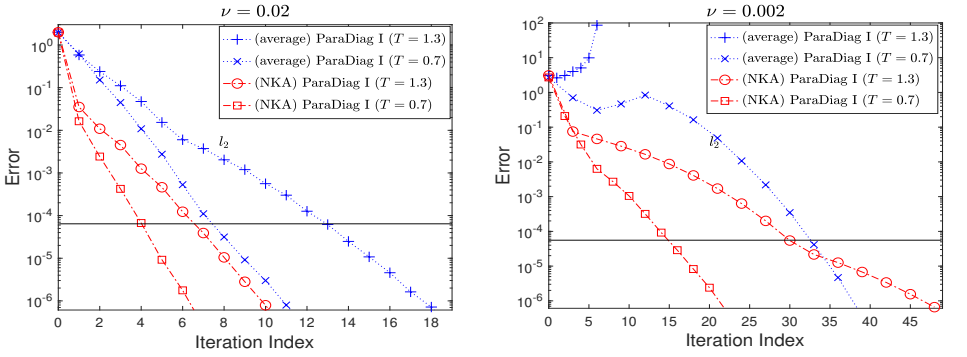

(a) (b)

Figure 3.14. Error of the two quasi-Newton versions of ParaDiag I with BVM discretization (3.38) for Burgers' equation (2.6) with two values of the diffusion parameter ν.

iteration

$$(B \otimes I_x - \Phi_k \otimes A_k)\boldsymbol{U}^{k+1} = \boldsymbol{b} - ((\Phi_k \otimes A_k)\boldsymbol{U}^k - F(\boldsymbol{U}^k)),$$

which, after multiplying both sides by the matrix $B^{-1} \otimes I_x$, can be represented as

$$(I_t \otimes I_x - B^{-1}\Phi_k \otimes A_k)\boldsymbol{U}^{k+1} = (B^{-1} \otimes I_x)(\boldsymbol{b} + F(\boldsymbol{U}^k)) - (B^{-1}\Phi_k \otimes A_k)\boldsymbol{U}^k.$$

By diagonalizing $B^{-1}\Phi_k$ as $V\text{diag}(\lambda_1, \lambda_2, \ldots, \lambda_{N_t})V^{-1}$, we can solve $\boldsymbol{U}^{k+1}$ via the three-step diagonalization procedure (3.46) as well, where for step b we now have to solve the linear systems

$$(I_x - \lambda_n A_k)\boldsymbol{u}_n^b = \boldsymbol{u}_n^a, \ n = 1, 2, \ldots, N_t.$$

So far there is no theory for the diagonalization of $B^{-1}\Phi_k$, but in practice this matrix is often diagonalizable and V is generally well-conditioned.

In practice, it is better not to compute the scaling factors $\{\phi_n\}$ for each Newton iteration, which can be rather expensive due to the matrix–matrix multiplications in (3.48). It suffices to compute these quantities only once before starting the Newton iteration (i.e. as an offline task) by using a *reduced* model. For time-dependent PDEs, such a model could be a semi-discretized system of ODEs obtained by using a coarse space grid. We now show this idea for Burgers' equation (2.6) with periodic boundary conditions, discretized by a centred finite difference scheme with mesh size $\Delta x = \frac{1}{200}$. The scaling factors $\{\phi_n\}$ were determined by the trapezoidal rule with a coarse mesh size $\Delta X = \frac{1}{20}$. In Figure 3.14 we show for two values of the diffusion parameter ν how the error decays for the two quasi-Newton versions of ParaDiag I with BVM discretization (3.38). For each ν we consider two time interval lengths, $T = 0.7$ and $T = 1.3$. Clearly the quasi-Newton version with the NKA technique improves the convergence rate, especially when $T = 1.3$.

3.5.2. Iterative ParaDiag methods (ParaDiag II)

It is difficult to generalize ParaDiag I to high-order time-integrators such as multistage Runge–Kutta methods. This is not the case for the class of ParaDiag II methods, which use approximations of the time-stepping matrices in order to make them diagonalizable, and then solve the all-at-once system by iteration.

The first member in the ParaDiag II class of methods was proposed in McDonald *et al.* (2018) at the discrete level, and independently in Gander and Wu (2019) at the continuous level. Although these two papers describe essentially the same method, the descriptions themselves are quite different. McDonald *et al.* (2018) considered the approximate solution of the first-order linear system of ODEs (2.1) using a linear multistep method with m-steps,

$$\sum_{l=0}^{m} a_l \boldsymbol{u}_{n-l} = \Delta t \sum_{l=0}^{m} b_l (A\boldsymbol{u}_{n-l}) + \bar{\boldsymbol{g}}_n, \ n = 1, \ldots, N_t,$$

where we assume that the first m initial values $\{\boldsymbol{u}_{-(m-1)}, \boldsymbol{u}_{-(m-2)}, \ldots, \boldsymbol{u}_0\}$ are given. The all-at-once system of these N_t difference equations is $\mathcal{K}\boldsymbol{U} = \boldsymbol{b}$ with $\boldsymbol{U} := (\boldsymbol{u}_1^\top, \ldots, \boldsymbol{u}_{N_t}^\top)^\top$ and $\mathcal{K} := B_1 \otimes I_x - B_2 \otimes (\Delta t A)$, where $\boldsymbol{b}$ is a vector depending on the initial values and the source term $\boldsymbol{g}(t)$, and

$$B_1 := \begin{bmatrix} a_0 & & & & & \\ a_1 & a_0 & & & & \\ \vdots & \ddots & \ddots & & & \\ a_m & & \ddots & \ddots & & \\ & \ddots & & a_1 & a_0 & \\ & & a_m & \ldots & a_1 & a_0 \end{bmatrix}, \quad B_2 := \begin{bmatrix} b_0 & & & & & \\ b_1 & b_0 & & & & \\ \vdots & \ddots & \ddots & & & \\ b_m & & \ddots & \ddots & & \\ & \ddots & & b_1 & b_0 & \\ & & a_m & \ldots & b_1 & b_0 \end{bmatrix}.$$

McDonald *et al.* (2018) solved this all-at-once system with GMRES using a preconditioner $\mathcal{P}$ for $\mathcal{K}$ obtained by replacing the two time-stepping matrices B_1 and B_2 with two circulant matrices of Strang type, that is,

$$\mathcal{P} := C_1 \otimes I_x - C_2 \otimes (\Delta t A),$$

where

$$C_1 := \begin{bmatrix} a_0 & & a_m & \ldots & a_1 & a_0 \\ a_1 & a_0 & & & & a_1 \\ \vdots & \ddots & \ddots & & \ddots & \vdots \\ a_m & & \ddots & \ddots & & a_m \\ & \ddots & & a_1 & a_0 & \\ & & a_m & \ldots & a_1 & a_0 \end{bmatrix}, \quad C_2 := \begin{bmatrix} b_0 & & b_m & \ldots & b_1 & b_0 \\ b_1 & b_0 & & & & b_1 \\ \vdots & \ddots & \ddots & & \ddots & \vdots \\ b_m & & \ddots & \ddots & & b_m \\ & \ddots & & b_1 & b_0 & \\ & & b_m & \ldots & b_1 & b_0 \end{bmatrix}.$$

For a theoretical understanding, or if the preconditioner $\mathcal{P}$ is very good (such as multigrid for Poisson problems), one can use it directly in the stationary iteration

$$\mathcal{P}\Delta \boldsymbol{U}^k = \boldsymbol{r}^k := \boldsymbol{b} - \mathcal{K}\boldsymbol{U}^k, \quad \boldsymbol{U}^{k+1} = \boldsymbol{U}^k + \Delta \boldsymbol{U}^k, \quad k = 0, 1, \ldots, \tag{3.49}$$

and the asymptotic convergence is fast if $\rho(\mathcal{P}^{-1}\mathcal{K}) \ll 1$. If convergence is not fast, this process can be accelerated using the preconditioner $\mathcal{P}$ within a Krylov method, i.e. solving the preconditioned linear system $\mathcal{P}^{-1}\mathcal{K}\boldsymbol{U} = \mathcal{P}^{-1}\boldsymbol{b}$ with a Krylov method; see Ciaramella and Gander (2022, Section 4.1) for a simple introduction. This can even work when $\rho(\mathcal{P}^{-1}\mathcal{K}) \geq 1$, and is advantageous when the spectrum $\sigma(\mathcal{P}^{-1}\mathcal{K})$ is clustered.

The first advantage of using the block-circulant matrix $\mathcal{P}$ as a preconditioner is that, similar to ParaDiag I, for each iteration, the preconditioning step $\mathcal{P}^{-1}\boldsymbol{r}^k$ can be solved via the diagonalization procedure, because any two circulant matrices C_1 and C_2 are commutative and can therefore be diagonalized simultaneously (Ng 2004, Chapter 4), that is,

$$C_l = \mathrm{F}^* D_l \mathrm{F}, \quad l = 1, 2,$$

where F is the discrete Fourier matrix defined as (F^* is the conjugate transform of F)

$$\mathrm{F} := \frac{1}{\sqrt{N_t}} \begin{bmatrix} 1 & 1 & \cdots & 1 \\ 1 & \omega & \cdots & \omega^{N_t-1} \\ \vdots & \vdots & \cdots & \vdots \\ 1 & \omega^{N_t-1} & \cdots & \omega^{(N_t-1)^2} \end{bmatrix}, \quad \omega := \exp\left(\frac{2\pi \mathrm{i}}{N_t}\right), \tag{3.50}$$

and $D_l := \mathrm{diag}(\lambda_{l,1}, \lambda_{l,2}, \ldots, \lambda_{l,N_t})$ contains the eigenvalues of C_l, that is,

$$D_l = \mathrm{diag}\left(\sqrt{N_t}\mathrm{F}C_l(:,1)\right), \quad l = 1, 2. \tag{3.51}$$

Then, according to the property of the Kronecker product, we can factor $\mathcal{P} = (\mathrm{F}^* \otimes I_x)(D_1 \otimes I_x - D_2 \otimes (\Delta t A))(\mathrm{F} \otimes I_x)$ and thus we can compute $\mathcal{P}^{-1}\boldsymbol{r}^k$ by again performing three steps:

$$\begin{cases} \boldsymbol{U}^a = (\mathrm{F} \otimes I_x)\boldsymbol{r}^k, & \text{(step a)} \\ (\lambda_{1,n} I_x - \lambda_{2,n}\Delta t A)\boldsymbol{u}_n^b = \boldsymbol{u}_n^a, \ n = 1, 2, \ldots, N_t, & \text{(step b)} \\ \boldsymbol{U} = (\mathrm{F}^* \otimes I_x)\boldsymbol{U}^b. & \text{(step c)} \end{cases} \tag{3.52}$$

Here the first and last steps can be computed efficiently using the fast Fourier transform (FFT), with $O(N_x N_t \log N_t)$ operations, and as in all ParaDiag methods, step b can be computed in parallel, since all linear systems are completely independent of each other at different time points.

McDonald *et al.* (2018, Section 3) obtained an important result about the clustering of eigenvalues of the preconditioned matrix $\mathcal{P}^{-1}\mathcal{K}$ when this ParaDiag II technique is used to precondition a system for its solve by a Krylov method.

Theorem 3.8. When $A \in \mathbb{R}^{N_x \times N_x}$ is symmetric negative definite, the preconditioned matrix $\mathcal{P}^{-1}\mathcal{K}$ has at most mN_x eigenvalues not equal to 1.

This implies that GMRES converges in at most $mN_x + 1$ steps for the all-at-once system $\mathcal{K}\boldsymbol{U} = \boldsymbol{b}$ using $\mathcal{P}$ as a preconditioner. Note, however, that when N_x is large, this result does not guarantee fast convergence of GMRES, and moreover, if A is not symmetric, the clustering of $\sigma(\mathcal{P}^{-1}\mathcal{K})$ becomes worse. To illustrate this, we consider three examples: the heat equation (2.3), the advection–diffusion equation (2.5) with two values of the diffusion parameter ν, and the second-order wave equation (2.7). We use homogeneous Dirichlet boundary conditions and the initial condition $u(x, 0) = \sin(2\pi x)$ for all PDEs, and for the wave equation we set $\partial_t u(x, 0) = 0$.

The semi-discrete system of ODEs using centred finite differences is of the form (2.1) for the first-order parabolic problems, and for the second-order wave equation we get

$$\boldsymbol{u}''(t) = A\boldsymbol{u}(t), \quad \boldsymbol{u}(0) = \boldsymbol{u}_0, \quad \boldsymbol{u}'(0) = 0, \quad t \in (0, T], \tag{3.53}$$

where $A = \text{Tri}[1 \quad -2 \quad 1]/\Delta x^2$. We solve the first-order system of ODEs (2.1) using the trapezoidal rule, and the second-order system of ODEs (3.53) using a parametrized Numerov-type method (Chawla 1983),

$$\begin{cases} \tilde{\boldsymbol{u}}_n - \boldsymbol{u}_n + \gamma \Delta t^2 A(\boldsymbol{u}_{n+1} - 2\boldsymbol{u}_n + \boldsymbol{u}_{n-1}) = 0, \\ \boldsymbol{u}_{n+1} - 2\boldsymbol{u}_n + \boldsymbol{u}_{n-1} - \dfrac{\Delta t^2 A}{12}(\boldsymbol{u}_{n+1} + 10\tilde{\boldsymbol{u}}_n + \boldsymbol{u}_n) = 0, \end{cases} \tag{3.54}$$

where $\gamma > 0$ is a parameter. For $\gamma = 0$, (3.54) reduces to the classical Numerov method, which is a fourth-order method but only conditionally stable. With $\gamma \geq \frac{1}{120}$, this method is unconditionally stable and still fourth-order.

Let $T = 2$, $\Delta t = \frac{1}{50}$, $\Delta x = \frac{1}{100}$ and $\gamma = \frac{1}{100}$. In Figure 3.15 we show the eigenvalues of the preconditioned matrix $\mathcal{P}^{-1}\mathcal{K}$ for these three PDEs, and the decay of the residual as function of the iteration number of the preconditioned GMRES solver. We see that for a wide range of problems, the block-circulant matrix $\mathcal{P}$ is a good preconditioner, even for the advection-dominated diffusion equation with a small diffusion parameter $\nu = 10^{-3}$. However, if we continue to reduce ν, Figure 3.15(c,d) shows that the preconditioner $\mathcal{P}$ becomes worse, and ultimately it loses its power when we switch to the hyperbolic problem represented by the wave equation.

During the same time, and independently of the work in McDonald *et al.* (2018), another diagonalization-based time parallel method was proposed in Gander and Wu (2019) within the framework of *waveform relaxation*. It is constructed at the continuous level by using a *head–tail* coupled condition,

$$\boldsymbol{u}_t^k(t) = A\boldsymbol{u}^k(t) + \boldsymbol{g}(t), \quad \boldsymbol{u}^k(0) = \alpha[\boldsymbol{u}^k(T) - \boldsymbol{u}^{k-1}(T)] + \boldsymbol{u}_0, \tag{3.55}$$

where $\alpha \in \mathbb{C}$ is a free parameter. Upon convergence, we recover the solution to the initial value problem (2.1), i.e. $\boldsymbol{u}_t(t) = A\boldsymbol{u}(t) + \boldsymbol{g}(t)$ with $\boldsymbol{u}(0) = \boldsymbol{u}_0$. For

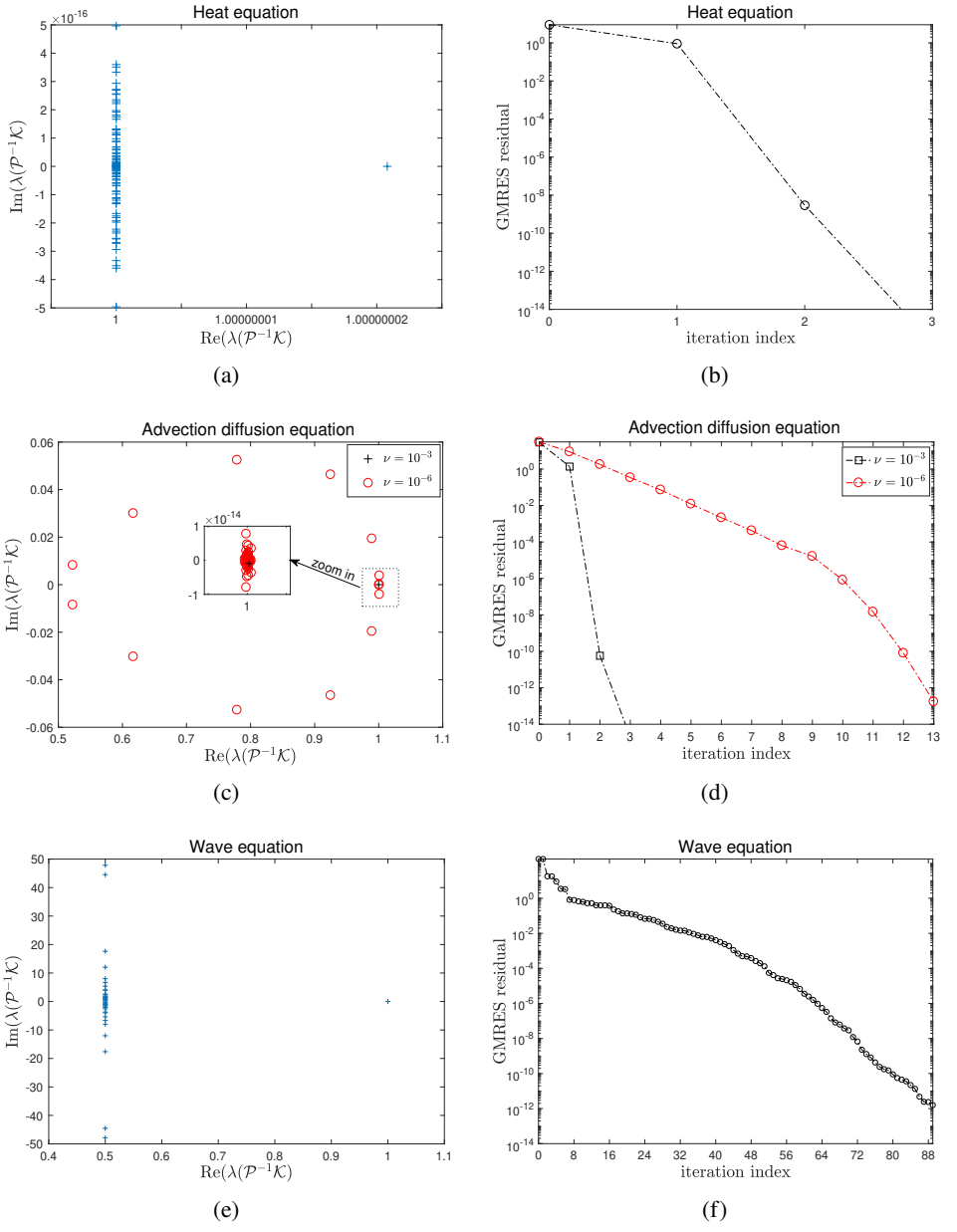

Figure 3.15. Spectra of the preconditioned matrix $\mathcal{P}^{-1}\mathcal{K}$ (a, c, e) and the measured convergence of preconditioned GMRES (b, d, f) for the three representative PDEs.

the second-order problem (2.7), the iteration (3.55) can be defined similarly by reducing the problem to a first-order system. The advantage of this iteration is that we can solve each iterate $\boldsymbol{u}^k(t)$ independently for all the time-steps. To see this, we need to take a closer look at the structure of the discrete system stemming from (3.55). Suppose we discretize (3.55) using a one-step time-integrator specified by two matrices $r_1(\Delta t A)$ and $r_2(\Delta t A)$,

$$\begin{cases} r_1(\Delta t A)\boldsymbol{u}_n^k = r_2(\Delta t A)\boldsymbol{u}_{n-1}^k + \tilde{\boldsymbol{g}}_n, \ n = 1, \dots, N_t, \\ \boldsymbol{u}_0^k = \alpha\left(\boldsymbol{u}_{N_t}^k - \boldsymbol{u}_{N_t}^{k-1}\right) + \boldsymbol{u}_0, \end{cases} \tag{3.56}$$

where $N_t = T/\Delta t$, $\boldsymbol{u}_0$ is a given initial value and $\tilde{\boldsymbol{g}}_n \in \mathbb{R}^{N_x}$ is a vector coming from the source term $\boldsymbol{g}(t)$. Examples for $r_1(\Delta t A)$ and $r_2(\Delta t A)$ are

$$\begin{cases} r_1 = I_x - \Delta t A, \ r_2 = I_x, & \text{backward Euler}, \\ r_1 = I_x - \dfrac{1}{2}\Delta t A, \ r_2 = I_x + \dfrac{1}{2}\Delta t A, & \text{trapezoidal rule}. \end{cases} \tag{3.57}$$

By replacing $\boldsymbol{u}_0^k$ with $\alpha\left(\boldsymbol{u}_{N_t}^k - \boldsymbol{u}_{N_t}^{k-1}\right) + \boldsymbol{u}_0$ for $n = 1$, we can unfold (3.56) as

$$\begin{cases} r_1(\Delta t A)\boldsymbol{u}_1^k - \alpha r_2(\Delta t A)\boldsymbol{u}_{N_t}^k = \alpha r_2(\Delta t A)\boldsymbol{u}_{N_t}^{k-1} + r_2(\Delta t A)\boldsymbol{u}_0 + \tilde{\boldsymbol{g}}_1, \\ r_1(\Delta t A)\boldsymbol{u}_2^k - r_2(\Delta t A)\boldsymbol{u}_1^k = \tilde{\boldsymbol{g}}_2, \\ r_1(\Delta t A)\boldsymbol{u}_3^k - r_2(\Delta t A)\boldsymbol{u}_2^k = \tilde{\boldsymbol{g}}_3, \\ \vdots \\ r_1(\Delta t A)\boldsymbol{u}_{N_t}^k - r_2(\Delta t A)\boldsymbol{u}_{N_t-1}^k = \tilde{\boldsymbol{g}}_{N_t}. \end{cases}$$

We see that all the discrete unknowns $\boldsymbol{u}_1, \boldsymbol{u}_2, \dots, \boldsymbol{u}_{N_t}$ are coupled together and therefore we have to solve them in one shot. To this end, we represent these N_t equations as

$$\mathcal{P}_\alpha \boldsymbol{U}^k = \boldsymbol{b}^k, \tag{3.58a}$$

where $\boldsymbol{U}^k := \left(\left(\boldsymbol{u}_1^k\right)^\top, \dots, \left(\boldsymbol{u}_{N_t}^k\right)^\top\right)^\top$ and $\boldsymbol{b}^k$ is a vector consisting of

$$\boldsymbol{b}^k := \boldsymbol{b} - \alpha \begin{bmatrix} r_2(\Delta t A)\boldsymbol{u}_{N_t}^{k-1} \\ 0 \\ \vdots \\ 0 \end{bmatrix}, \quad \boldsymbol{b} := \begin{bmatrix} r_2(\Delta t A)\boldsymbol{u}_0 + \tilde{\boldsymbol{g}}_1 \\ \tilde{\boldsymbol{g}}_2 \\ \vdots \\ \tilde{\boldsymbol{g}}_{N_t} \end{bmatrix}. \tag{3.58b}$$

The matrix $\mathcal{P}_\alpha$ is given by

$$\begin{aligned}\mathcal{P}_\alpha &:= \begin{bmatrix} r_1(\Delta t A) & & & -\alpha r_2(\Delta t A) \\ -r_2(\Delta t A) & r_1(\Delta t A) & & \\ & \ddots & \ddots & \\ & & -r_2(\Delta t A) & r_1(\Delta t A) \end{bmatrix} \\ &= I_t \otimes r_1(\Delta t A) - C_\alpha \otimes r_2(\Delta t A), \end{aligned} \tag{3.58c}$$

$$C_\alpha := \begin{bmatrix} 0 & & & \alpha \\ 1 & 0 & & \\ & \ddots & \ddots & \\ & & 1 & 0 \end{bmatrix} \in \mathbb{R}^{N_t \times N_t}.$$

The matrix C_α is known as an α-circulant matrix, which, similarly to the standard circulant matrix where $\alpha = 1$, can be diagonalized by an eigenvector matrix V_α that depends only on α. Specifically, according to Bini, Latouche and Meini (2005, Theorem 2.10), for an arbitrary α-circulant matrix C_α of Strang type, we have the spectral decomposition

$$C_\alpha = V_\alpha D_\alpha V_\alpha^{-1}, \tag{3.59a}$$

where the diagonal eigenvalue matrix and the eigenvector matrix V_α are given by

$$\begin{aligned} &D_\alpha = \operatorname{diag}(\sqrt{N_t}\mathrm{F}\Lambda_\alpha C_\alpha(:,1)), \\ &V_\alpha = \Lambda_\alpha \mathrm{F}^*,\ \Lambda_\alpha := \operatorname{diag}\left(1, \alpha^{-1/N_t}, \ldots, \alpha^{-(N_t-1)/N_t}\right), \end{aligned} \tag{3.59b}$$

and $C_\alpha(:,1)$ represents the first column of C_α. Using the property of the Kronecker product, we can factor $\mathcal{P}_\alpha$ as

$$\mathcal{P}_\alpha = (V_\alpha \otimes I_x)(I_t \otimes r_1(\Delta t A) - D_\alpha \otimes r_2(\Delta t A))(V_\alpha^{-1} \otimes I_x),$$

and hence again solve as in all ParaDiag methods for $\boldsymbol{U}^k$ in (3.58a) using three steps:

$$\begin{cases} \boldsymbol{U}^a = (V_\alpha^{-1} \otimes I_x)\boldsymbol{b}^k, & \text{(step a)} \\ (r_1(\Delta t A) - \lambda_n r_2(\Delta t A))\boldsymbol{u}_n^b = \boldsymbol{u}_n^a,\ n = 1, 2, \ldots, N_t, & \text{(step b)} \\ \boldsymbol{U}^k = (V_\alpha \otimes I_x)\boldsymbol{U}^b. & \text{(step c)} \end{cases} \tag{3.60}$$

When $\alpha = 1$, the eigenvector matrix becomes the Fourier matrix, $V_\alpha = \mathrm{F}^*$, and hence this ParaDiag II method obtained from the discretization of the continuous formulation (3.55) coincides with (3.52) from McDonald *et al.* (2018), and since $V_\alpha \otimes I_x = (\Lambda_\alpha \otimes I_x)(\mathrm{F}^* \otimes I_x)$ and $V_\alpha^{-1} \otimes I_x = (\mathrm{F} \otimes I_x)(\Lambda_\alpha^{-1} \otimes I_x)$, we can still use FFT techniques for the first and last step, also when $\alpha \neq 1$.

Gander and Wu (2019) examined the convergence of the waveform relaxation iterations (3.55) at the continuous level, and showed that the error $\boldsymbol{u}^k(t) - \boldsymbol{u}(t)$ decays rapidly for both first-order and second-order problems, with a rate depending on α.

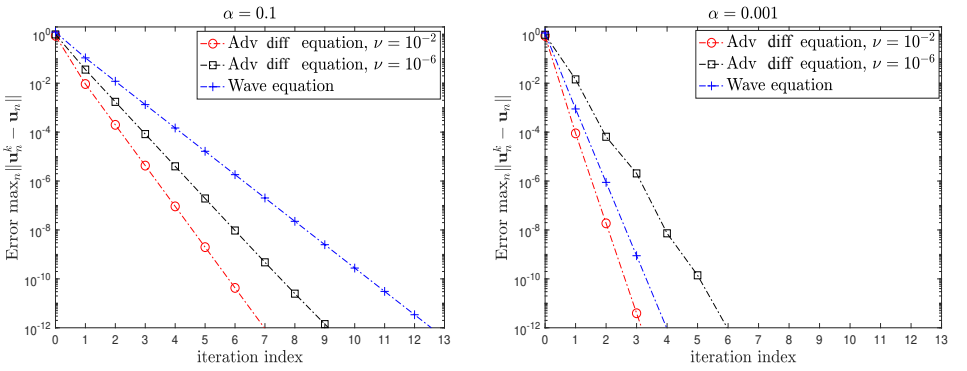

Figure 3.16. Error as a function of iteration for the head–tail coupled waveform relaxation method (3.55) using two values of the parameter α and the trapezoidal rule.

We illustrate this in Figure 3.16, where the data for the two PDEs are the same as those used in Figure 3.15, but using periodic boundary conditions. For this type of boundary conditions, the preconditioner $\mathcal{P}$ with the special choice $\alpha = 1$ as proposed in McDonald *et al.* (2018) is singular and cannot be used, so we need to use $\alpha < 1$. We see that the introduction of the parameter α makes this ParaDiag II method a very powerful solver, which also works very well for highly advection-dominated problems as well as the hyperbolic wave equation – and this without Krylov acceleration!

Gander and Wu (2019) studied two time-integrators, backward Euler and the trapezoidal rule, and showed that the discrete algorithm (3.56) preserves the convergence rate obtained from the analysis at the continuous level. The proof is technical and relies on a special representation of $r_1^{-1}(\Delta t A) r_2(\Delta t A)$ that appears to hold only for these two specific time-integrators (see (3.57) for the formulas of r_1 and r_2).

The head–tail coupled waveform relaxation method at the discrete level (3.56) can be represented as the *preconditioned* stationary iteration

$$\mathcal{P}_\alpha \Delta \boldsymbol{U}^{k-1} = \boldsymbol{r}^{k-1} := \boldsymbol{b} - \mathcal{K}\boldsymbol{U}^{k-1}, \quad \boldsymbol{U}^k = \boldsymbol{U}^{k-1} + \Delta \boldsymbol{U}^{k-1}, \quad k = 1, 2, \ldots, \tag{3.61}$$

where

$$\begin{aligned} \mathcal{K} &:= \begin{bmatrix} r_1(\Delta t A) & & & \\ -r_2(\Delta t A) & r_1(\Delta t A) & & \\ & \ddots & \ddots & \\ & & -r_2(\Delta t A) & r_1(\Delta t A) \end{bmatrix} \\ &= I_t \otimes r_1(\Delta t A) - B \otimes r_2(\Delta t A), \end{aligned} \tag{3.62a}$$

and $B \in \mathbb{R}^{N_t \times N_t}$ is a Toeplitz matrix,

$$B := \begin{bmatrix} 0 & & & \\ 1 & 0 & & \\ & \ddots & \ddots & \\ & & 1 & 0 \end{bmatrix}. \tag{3.62b}$$

We thus see that the preconditioned iteration (3.61) with $\alpha = 1$ is precisely the method (3.49) of McDonald *et al.* (2018). For $\alpha \in (0, 1)$ the preconditioned iteration is the parallel method proposed by Banjai and Peterseim (2012). To see why the preconditioned iteration (3.61) equals the head–tail coupled waveform relaxation method (3.56), we notice that the vector $\boldsymbol{b}^k$ in (3.62b) can be represented as $\boldsymbol{b}^k = (\mathcal{P}_\alpha - \mathcal{K})\boldsymbol{U}^{k-1} + \boldsymbol{b}$, and substituting this into (3.62a) gives $\mathcal{P}_\alpha \boldsymbol{U}^k = (\mathcal{P}_\alpha - \mathcal{K})\boldsymbol{U}^{k-1} + \boldsymbol{b}$, which leads to (3.61).

Applying a one-step time-integrator specified by $r_1(\Delta t A)$ and $r_2(\Delta t A)$ to the initial value problem (2.1), i.e. $\boldsymbol{u}'(t) = A\boldsymbol{u}(t) + \boldsymbol{g}(t)$ with $\boldsymbol{u}(0) = \boldsymbol{u}_0$, leads to

$$r_1(\Delta t A)\boldsymbol{u}_n = r_2(\Delta t A)\boldsymbol{u}_{n-1} + \tilde{\boldsymbol{g}}_n,\ n = 1, \ldots, N_t. \tag{3.63}$$

Therefore the matrix $\mathcal{K}$ is an all-at-once representation of these N_t difference equations, i.e. $\mathcal{K}\boldsymbol{U} = \boldsymbol{b}$. From this point of view, $\mathcal{P}_\alpha$ is a generalized block circulant preconditioner for $\mathcal{K}$.

For second-order problems of the form $\boldsymbol{u}''(t) = A\boldsymbol{u}(t) + \boldsymbol{g}(t)$ with initial values $\boldsymbol{u}(0) = u_0$ and $\tilde{\boldsymbol{u}}(0) = \tilde{\boldsymbol{u}}_0$, we can introduce $\boldsymbol{v}(t) = \boldsymbol{u}'(t)$ to transform them into a larger first-order system of ODEs, and then apply ParaDiag II. However, this approach doubles the memory requirements at each time-step, which can be problematic in cases of very fine spatial mesh sizes or for high-dimensional problems. In that case it can be preferable to discretize the second-order problem directly, and we consider the symmetric two-step method

$$r_1(\Delta t^2 A)\boldsymbol{u}_{n+1} - r_2(\Delta t^2 A)\boldsymbol{u}_n + r_1(\Delta t^2 A)\boldsymbol{u}_{n-1} = \tilde{\boldsymbol{g}}_n, \quad n = 1, \ldots, N_t - 1, \tag{3.64}$$

assuming that the second initial value $\boldsymbol{u}_1$ is given. Examples of the matrices r_1 and r_2 are

$$r_1(\Delta t^2 A) = I_x - \frac{\Delta t^2 A}{12} + \frac{10\gamma(\Delta t^2 A)^2}{12},$$
$$r_2(\Delta t^2 A) = 2I_x + \frac{10\Delta t^2 A}{12} + \frac{20\gamma(\Delta t^2 A)^2}{12},$$

if we use the Numerov-type method from (3.54) as the time-integrator. For (3.64), the all-at-once matrix and the corresponding preconditioner are

$$\begin{aligned} \mathcal{K} &= \tilde{B} \otimes r_1(\Delta t^2 A) - B \otimes r_2(\Delta t^2 A), \\ \mathcal{P}_\alpha &= \tilde{C}_\alpha \otimes r_1(\Delta t^2 A) - C_\alpha \otimes r_2(\Delta t^2 A), \end{aligned} \tag{3.65a}$$

where B is the Toeplitz matrix from (3.62b), and C_α is the α-circulant matrix of B

(see (3.58c)). The matrices $\tilde{B}$ and $\tilde{C}_\alpha$ are defined as

$$\tilde{B} := \begin{bmatrix} 1 & & & & \\ 0 & 1 & & & \\ 1 & 0 & 1 & & \\ & \ddots & \ddots & \ddots & \\ & & 1 & 0 & 1 \end{bmatrix}, \quad \tilde{C}_\alpha := \begin{bmatrix} 1 & & & \alpha & \\ 0 & 1 & & & \alpha \\ 1 & 0 & 1 & & \\ & \ddots & \ddots & \ddots & \\ & & 1 & 0 & 1 \end{bmatrix}. \tag{3.65b}$$

According to (3.59a)–(3.59b), we can simultaneously diagonalize C_α and $\tilde{C}_\alpha$. Thus, for the stationary iteration (3.61), we can solve the preconditioning step $\mathcal{P}_\alpha^{-1}\boldsymbol{r}^k$ using the diagonalization procedure (see (3.60)) as well.

The preconditioner $\mathcal{P}_\alpha$ used in the ParaDiag II method involves substituting the Toeplitz matrix within the all-at-once matrix $\mathcal{K}$ with a circulant (or α-circulant) matrix, while keeping the space matrices unchanged. This substitution, which approximates a pointwise Toeplitz matrix B by a circulant (or α-circulant) matrix C, is a natural approach that dates back to Strang (1986). The spectrum of the preconditioned matrix $C^{-1}B$ has been extensively examined by researchers over the past three decades, yielding fruitful results; for more details, see the survey paper by Chan and Ng (1996) and the monographs by Ng (2004) and Bini *et al.* (2005).

For blockwise Toeplitz matrices, where all blocks are Toeplitz (referred to as BTTB matrices), the circulant preconditioner is obtained by approximating each block by a circulant matrix, analogous to the approach used in ParaDiag II. Spectral analyses of such preconditioned matrices can be found in Chan and Ng (1996) and Ng (2004). However, in the context of ParaDiag II, the blocks (e.g. $r_1(\Delta t A)$ and $r_2(\Delta t A)$ in (3.57)) are not Toeplitz. In this scenario, there is a lack of systematic results regarding the eigenvalues of $\mathcal{P}_\alpha^{-1}\mathcal{K}$, and the work in McDonald *et al.* (2018) explores this for $\alpha = 1$.

Since McDonald *et al.* (2018) and Gander and Wu (2019), a lot of effort has been put into analysing the spectrum of $\mathcal{P}_\alpha^{-1}\mathcal{K}$. Examples include the work of Gu and Wu (2020), Lin and Ng (2021), Wu and Zhou (2021*a*,*b*), Danieli, Southworth and Wathen (2022), Bouillon, Samaey and Meerbergen (2024) and Heinzelreiter and Pearson (2024) for parabolic problems, and Danieli and Wathen (2021) and Liu and Wu (2020) for hyperbolic problems. The analyses are intricate and rely heavily on special properties of the time-integrator, such as sparsity, Toeplitz structure and diagonal dominance of the time-stepping matrix.

A comprehensive spectral analysis of the preconditioned matrix $\mathcal{P}_\alpha^{-1}\mathcal{K}$ for both first-order and second-order problems can be found in Wu, Zhou and Zhou (2022), with results that hold for any stable one-step time-integrator for first-order systems of ODEs, and any two-step symmetric time-integrator for second-order systems of ODEs.

Theorem 3.9. For the first-order system of ODEs $\boldsymbol{u}'(t) = A\boldsymbol{u}(t) + \boldsymbol{g}(t)$, if the one-step time-integrator (3.63) is stable, i.e. $|r_1^{-1}(z)r_2(z)| \le 1$ for $z \in \sigma(\Delta t A) \subset \mathbb{C}^-$,

then the eigenvalues of the preconditioned matrix satisfy

$$\frac{1}{1-\alpha} \leq |\lambda(\mathcal{P}_\alpha^{-1}\mathcal{K})| \leq \frac{1}{1+\alpha}, \tag{3.66}$$

where $\mathcal{K}$ is the all-at-once matrix of the time-integrator (3.63), and $\mathcal{P}_\alpha$ is the block α-circulant matrix given by (3.58c) with $\alpha \in (0, 1)$. Similarly, for the second-order system of ODEs $\boldsymbol{u}''(t) = A\boldsymbol{u}(t) + \boldsymbol{g}(t)$, if the two-step method (3.64) is stable, i.e. $|r_1^{-1}(z)r_2(z)| \leq 2$ (for all $z \in \sigma(\Delta t^2 A) \subset \mathbb{R}^-$ and $|r_1^{-1}(z)r_2(z)| = 2$ only if $z = 0$), then the eigenvalues of the preconditioned matrix $\mathcal{P}_\alpha^{-1}\mathcal{K}$ (with $\mathcal{P}$ and $\mathcal{K}$ given by (3.65a)–(3.65b)) also satisfy the bounds in (3.66).

For the stationary iteration (3.61), the iteration matrix $\mathcal{M}$ is given by

$$\mathcal{M} = \mathcal{I} - \mathcal{P}_\alpha^{-1}\mathcal{K}, \tag{3.67}$$

and based on (3.66), we get $\rho(\mathcal{M}) \leq \alpha/(1-\alpha)$. This explains the faster convergence of the ParaDiag II head–tail waveform relaxation method (3.55) when α is small, as we have seen in Figure 3.16. The stability of the underlying time-integrator serves as a sufficient condition for the eigenvalue bounds of the preconditioned matrix $\mathcal{P}_\alpha^{-1}\mathcal{K}$ in Theorem 3.9, or equivalently the iteration matrix $\mathcal{M}$. Numerically, we find that stability is also a necessary condition. We illustrate this now for the Numerov-type method (3.54) applied to a second-order problem with A being a centred finite difference discretization of the Laplacian with Dirichlet boundary conditions, that is,

$$\frac{1}{\Delta x^2} A \approx \partial_{xx}.$$

Setting $\Delta t = \frac{1}{16}$, $\Delta x = \frac{1}{128}$, and $\alpha = 0.02$, Figure 3.17 shows the eigenvalues of the iteration matrix $\mathcal{M}$ for $T = 0.5$, 10 and 20, using the two values $\gamma = \frac{1}{120}$ and $\gamma = \frac{1}{120.01}$ for the Numerov-type method, where according to Chawla (1983), $\gamma = \frac{1}{120}$ represents a stability threshold for the Numerov-type method. For this threshold value (Figure 3.17(a–c)), all eigenvalues of $\mathcal{M}$ lie within the theoretically analysed circle. However, with $\gamma = \frac{1}{120.01}$ (slightly below the threshold), the Numerov-type method loses unconditional stability, and the results in Figure 3.17(d–f) clearly indicate that the eigenvalue bounds (3.66) no longer hold for large T.

The eigenvalue bounds (3.66) indicate that the ParaDiag II method converges faster when α decreases. This is true within a certain range of α, such as $\alpha \in [10^{-3}, 10^{-1}]$, as shown earlier (see Figure 3.16). However, α cannot be arbitrarily small due to roundoff errors arising from diagonalizing the α-circulant matrix. Specifically, for any diagonalizable square matrix P, floating point operations limit the precision of its factorization $P \approx VDV^{-1}$. For the α-circulant matrix C_α (see (3.58c)), even though its eigenvalues and eigenvectors have closed-form expressions, the difference between C_α and $V_\alpha D_\alpha V_\alpha^{-1}$ grows linearly as α

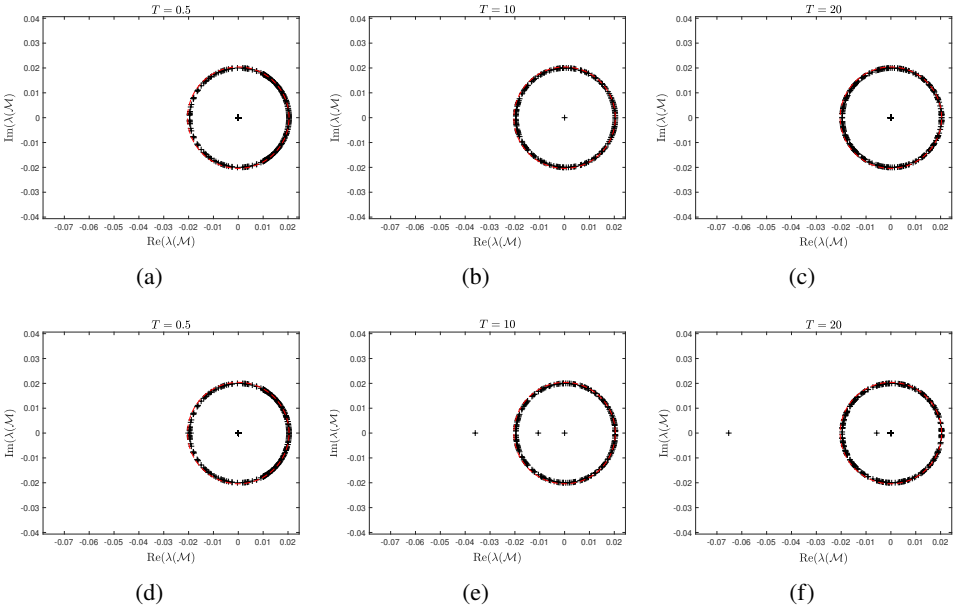

Figure 3.17. Eigenvalues of the iteration matrix $\mathcal{M}$ (see (3.67)) for the wave equation (2.7): (a,b,c) $\gamma = \frac{1}{120}$, (d,e,f) $\gamma = \frac{1}{120.01}$. In each panel, the dashed line represents the circle with radius $\alpha/(1-\alpha)$.

decreases, the roundoff error $\mathrm{err}_{\mathrm{ro}}$ behaving like

$$\mathrm{err}_{\mathrm{ro}} = O(\epsilon \mathrm{Cond}_2(V_\alpha)) = O\left(\frac{\epsilon}{\alpha}\right),$$

where ϵ is the machine precision (e.g. $\epsilon = 2.2204 \times 10^{-16}$ for double precision), and the equality follows from Gander and Wu (2019) and the fact that $V_\alpha = \Lambda_\alpha \mathrm{F}^*$ (see (3.59b)) with $\mathrm{Cond}_2(\mathrm{F}^*) = 1$, implying $\mathrm{Cond}_2(V_\alpha) = 1/\alpha$. Interestingly, this does not necessarily imply a similar growth in the roundoff error of the ParaDiag II method. The error behaviour depends on the implementation: directly solving for $\boldsymbol{U}^k$ as in (3.58a)–(3.58b) may lead to the growth discussed above, while first solving the error equation for $\Delta\boldsymbol{U}^{k-1}$ and then updating $\boldsymbol{U}^k$ (see (3.61)) can significantly mitigate the roundoff error; see Figure 3.18 for an illustration. A comprehensive study of the roundoff error for ParaDiag II will appear in Wu, Yang and Zhou (2025).

So far we have only considered one-step and symmetric two-step time-integrators. For general multistep methods, the eigenvalues of the preconditioned matrix $\mathcal{P}_\alpha^{-1}\mathcal{K}$ do not necessarily satisfy (3.66), yet we can demonstrate analogous results. For example, the case where $\mathcal{K} = B \otimes I_x - I_t \otimes A$, with B being a *dense* lower triangular Toeplitz matrix, was studied in Gu and Wu (2020). This matrix arises in solving Volterra partial integro-differential equations, and its first column

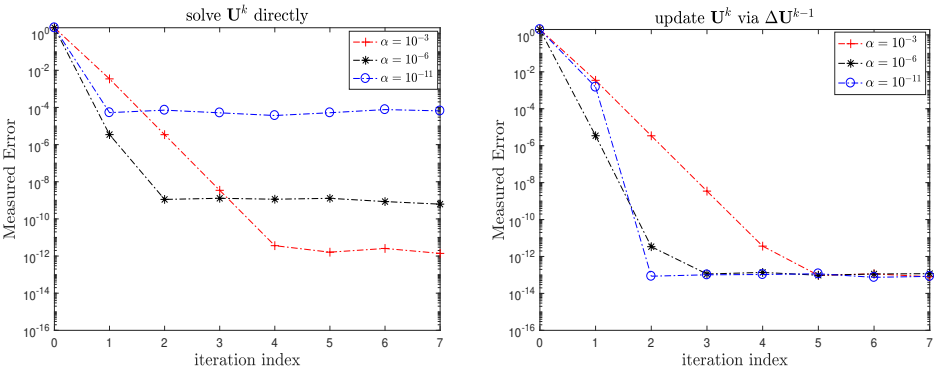

Figure 3.18. Measured error of ParaDiag II for the wave equation (2.7) implemented in two modes for three values of α.

$\boldsymbol{\omega} = (\omega_0, \omega_1, \ldots, \omega_{N_t})$ is determined by the quadrature used to handle the integral term. Gu and Wu (2020) established a bound for the eigenvalues of the form $|\lambda(\mathcal{P}_\alpha^{-1}\mathcal{K})| = 1 + O(\alpha)$, provided that the quantities $\{\omega_n\}$ satisfy certain conditions, such as positivity and monotonicity.

Turning to nonlinear problems, the application of ParaDiag II closely resembles that of ParaDiag I. We illustrate this for the first-order problem $\boldsymbol{u}'(t) = f(t, \boldsymbol{u}(t))$ discretized using backward Euler with step size Δt. Initially we apply Newton's iteration to the nonlinear all-at-once system,

$$\mathcal{J}\Delta\boldsymbol{U}^l = \boldsymbol{b} - F(\boldsymbol{U}^l), \quad \boldsymbol{U}^{l+1} = \boldsymbol{U}^l + \Delta\boldsymbol{U}^l, \tag{3.68}$$

where the Jacobian matrix $\mathcal{J} := B \otimes I_x - \nabla F_l$ (see (3.43a)–(3.43b)), with

$$\nabla F_l = \mathrm{blkdiag}\big(\nabla f(\boldsymbol{u}_1^l, t_1), \ldots, \nabla f(\boldsymbol{u}_{N_t}^l, t_{N_t})\big),$$

$$B = \frac{1}{\Delta t}\begin{bmatrix} 1 & & & \\ -1 & 1 & & \\ & \ddots & \ddots & \\ & & -1 & 1 \end{bmatrix}.$$

Then we solve (3.68) with GMRES using $\mathcal{P}_\alpha = C_\alpha \otimes I_x - I_t \otimes A_l$ as preconditioner, where C_α is the α-circulant matrix of B, and A_l is the average matrix of $\{\nabla f(\boldsymbol{u}_n^l, t_n)\}$. In general we cannot use the stationary iteration (3.61) to solve the Jacobian system (3.68) since $\rho(\mathcal{P}_\alpha^{-1}\mathcal{J}) > 1$. However, the eigenvalues of $\mathcal{P}_\alpha^{-1}\mathcal{J}$ are clustered, which is good for GMRES. The eigenvalue distribution of $\mathcal{P}_\alpha^{-1}\mathcal{J}$ is influenced by the length of the time interval T, with a shorter T leading to more clustered eigenvalues and thus faster GMRES convergence. Numerical evidence supporting this aspect can be found in Gander and Wu (2019) and Wu *et al.* (2022). Additionally, we can leverage the nearest Kronecker product approximation introduced in Section 3.5.1 to accelerate convergence; see Liu and Wu (2022).

4. PinT methods designed for parabolic problems

In Section 2 we showed intuitively why realizing PinT computations for hyperbolic problems is more challenging than for parabolic problems: parabolic problems tend to have local solutions in time, except for very low-frequency components, whereas hyperbolic problems have highly non-local solutions in time, and this is over all frequency components, from the lowest to the highest ones. Nevertheless, in Section 3 we showed PinT methods that are effective for hyperbolic problems and thus tackle all frequency components in a non-local way in time. Naturally, these methods often perform even better when applied to parabolic problems, since they tackle all frequency components over a long time, which includes the few very low-frequency components that are highly non-local in time in parabolic problems. The methods we have seen so far, however, were often designed for linear problems, where they are most effective, whereas for nonlinear problems they all suffer from certain drawbacks. For example, for OSWR it is not easy to determine the optimized Robin parameters, and without a reasonable parameter, the convergence rate can be quite poor. For ParaExp and ParaDiag I and II, nonlinearity also affects the convergence rate of the Newton iteration used as an outer solver, and in particular, the Newton iteration may converge slowly or even diverge when the time interval is large. In this section we now show PinT methods that were designed for parabolic problems and take advantage of their properties to be local in time, as we saw in Section 2, and they work equally well for linear and nonlinear problems. They have entirely different convergence mechanisms and properties from the methods in Section 3, and a direct application of these methods to hyperbolic problems often leads to slow convergence or even divergence.

4.1. Historical development

The first method we want to introduce is the Parareal algorithm from Lions *et al.* (2001), which we have already mentioned in Section 3.4 to describe the nonlinear ParaExp variant. Even though Parareal was invented independently, it has its roots in earlier work on multiple shooting techniques for evolution problems (see Bellen and Zennaro 1989, Chartier and Philippe 1993), and the algorithm had already been presented in Saha *et al.* (1997) with a coarse model instead of a coarse grid in the context of solar system simulations, mentioning a relation to waveform relaxation. A very early precursor is the paper by Nievergelt (1964), although the method there is not iterative. Parareal, proposed 20 years ago, has attracted considerable attention in scientific and engineering computations. The convergence of Parareal is very well understood; see e.g. Gander and Vandewalle (2007), Gander and Hairer (2008, 2014) and Gander and Lunet (2024). In a sense, Parareal can be regarded as a template for developing more efficient PinT methods. There are numerous modifications of Parareal in the literature to make it applicable to different problems or for different purposes. Interesting examples are the *parallel implicit time integration algorithm* (PITA) (see Farhat and Chandesris 2003, Farhat, Cortial, Dastillung

and Bavestrello 2006, Cortial and Farhat 2009), the *parallel full approximation scheme in space–time* (PFASST) (see Minion 2011, Emmett and Minion 2012, Minion *et al.* 2015), *multigrid reduction in time* (MGRiT) (see Falgout *et al.* 2014, Dobrev, Kolev, Petersson and Schroder 2017, Hessenthaler *et al.* 2020), and also combinations of Parareal with ParaDiag (Wu 2018, Gander and Wu 2020). We present the convergence mechanisms and convergence properties of Parareal and its variants in this section. The basic feature of PinT methods based on Parareal is that they use two grids (or more) for the time discretization, while for space discretization they use just one grid. The idea of using multigrid in both space and time goes back to the *parabolic multigrid method* in Hackbusch (1984), with an elegant analysis in the form of *multigrid waveform relaxation* in Lubich and Ostermann (1987). Coarsening in time was not effectively possible in this approach, and important improvements using multigrid techniques for highly advective problems were proposed in Vandewalle and Van de Velde (1994), Horton and Vandewalle (1995), Janssen and Vandewalle (1996) and Van Lent and Vandewalle (2002). A new *space–time multigrid* (STMG) method using only standard components but, as a new main ingredient, a block Jacobi smoother in time was introduced and analysed in Gander and Neumüller (2016), and this is currently one of the most powerful PinT algorithms for parabolic problems, with excellent strong and weak scalability properties; see also Neumüller and Smears (2019). We will introduce STMG at the end of this section, and show its effectiveness for nonlinear parabolic problems as well.

4.2. Parareal

The Parareal algorithm proposed in Lions *et al.* (2001) is a non-intrusive time-parallel solver that is based on multiple shooting, although it was not invented in this context but in the context of virtual control. In Parareal, the Jacobian in Newton's method used to solve the shooting equations is approximated by a finite difference across two iterates on a coarser grid or model (Gander and Vandewalle 2007). Similarly to ParaExp, it is based on a time decomposition of the interval $(0, T)$ into several smaller time intervals $0 = T_0 < T_1 < \cdots < T_N = T$, with for example $T_n = T_0 + n\Delta t$. However, in contrast to ParaExp, it uses an iteration, starting with an initial guess $\boldsymbol{U}_n^0$ at T_n. For iteration index $k = 0, 1, \ldots$, Parareal computes improved approximations using the update formula

$$\boldsymbol{u}_{n+1}^{k+1} = \mathcal{F}\big(T_n, T_{n+1}, \boldsymbol{u}_n^k\big) + \mathcal{G}\big(T_n, T_{n+1}, \boldsymbol{u}_n^{k+1}\big) - \mathcal{G}\big(T_n, T_{n+1}, \boldsymbol{u}_n^k\big). \tag{4.1}$$

Here, $\mathcal{F}(T_n, T_{n+1}, \boldsymbol{u}_n^k)$ represents an accurate solver that uses a smaller step size Δt for the underlying evolution problem, with initial condition $\boldsymbol{u}_n^k$ at time $t = T_n$, yielding an approximate solution at time $t = T_{n+1}$. Similarly, $\mathcal{G}$ is a less expensive and less accurate solver that uses a larger step size, for example ΔT, or a simpler model, and the difference of the two $\mathcal{G}$ terms in (4.1) represents precisely the approximation of the Jacobian; see Gander and Vandewalle (2007). Note that in

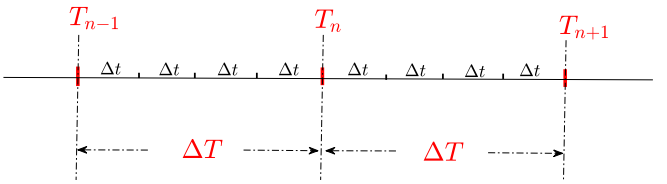

Figure 4.1. Parareal uses two time grids, where each large time-step size ΔT contains J small time-step sizes Δt.

(4.1) all the computationally expensive $\mathcal{F}$ solves can be performed in parallel, since at iteration k the approximations $\boldsymbol{u}_n^k$ are all known. For simplicity we will consider uniform fine and coarse time grids, assuming that each large step size contains J small steps, i.e. $\Delta T/\Delta t = J \geq 2$; see Figure 4.1. However, in principle, it is straightforward to apply non-uniform time grids in Parareal; see Gander (2017), Maday and Mula (2020) and Wu and Zhou (2024).

The convergence of Parareal is well understood, both for linear problems (Gander and Vandewalle 2007) and nonlinear problems (Gander and Hairer 2008): it converges superlinearly on bounded time intervals and linearly for parabolic problems on arbitrarily long time intervals. Specifically, for the linear problem (2.1), i.e. $\boldsymbol{u}'(t) = A\boldsymbol{u}(t) + \boldsymbol{g}(t)$ with initial value $\boldsymbol{u}(0) = \boldsymbol{u}_0$, and assuming that the fine and coarse solvers $\mathcal{G}$ and $\mathcal{F}$ are one-step time-integrators with stability functions $\mathrm{R}_g(z)$ and $\mathrm{R}_f(z)$, we have the following convergence results.

Theorem 4.1. Let $\{\boldsymbol{u}_n\}_{n=1}^{N_t}$ be the solutions computed sequentially by the $\mathcal{F}$ solver, $\boldsymbol{u}_{n+1} = \mathcal{F}(T_n, T_{n+1}, \boldsymbol{u}_n)$. Suppose the matrix A of the linear system of ODEs (2.1) is diagonalizable, $A = V_A D V_A^{-1}$, and the coarse solver $\mathcal{G}$ is stable, i.e. $|\mathrm{R}_g(z)| \leq 1$ for $z \in \sigma(\Delta T A)$. Then Parareal satisfies the convergence estimate

$$\max_{1\leq n\leq N_t} \|V_A(\boldsymbol{u}_n^k - \boldsymbol{u}_n)\|_\infty \leq \max_{z\in\sigma(\Delta T A)} \|M^k(z)\|_\infty \max_{1\leq n\leq N_t} \|V_A(\boldsymbol{u}_n^0 - \boldsymbol{u}_n)\|_\infty, \tag{4.2}$$

where $M(z)$ is a Toeplitz matrix given by two matrices $M_g(z)$ and $M_f(z)$,

$$\begin{aligned} M(z) &:= M_g^{-1}(z)[M_g(z) - M_f(z)], \\ M_g(z) &:= \begin{bmatrix} 1 & & & \\ -\mathrm{R}_g(z) & 1 & & \\ & \ddots & \ddots & \\ & & -\mathrm{R}_g(z) & 1 \end{bmatrix}, \\ M_f(z) &:= \begin{bmatrix} 1 & & & \\ -\mathrm{R}_f^J(z/J) & 1 & & \\ & \ddots & \ddots & \\ & & -\mathrm{R}_f^J(z/J) & 1 \end{bmatrix}. \end{aligned} \tag{4.3}$$

Proof. Applying the Parareal iteration (4.1) to the system of ODEs yields

$$\boldsymbol{u}_{n+1}^{k+1} = \mathrm{R}_f^J(\Delta TA/J)\boldsymbol{u}_n^k + \mathrm{R}_g(\Delta TA)\boldsymbol{u}_n^{k+1} - \mathrm{R}_g(\Delta TA)\boldsymbol{u}_n^k, \quad n = 0, 1, \ldots, N_t - 1.$$

Since the overall fine solution computed sequentially by the $\mathcal{F}$ solver satisfies $\boldsymbol{u}_{n+1} = \mathcal{F}(T_n, T_{n+1}, \boldsymbol{u}_n)$, it also satisfies by adding and subtracting the same term

$$\boldsymbol{u}_{n+1} = \mathrm{R}_f^J(\Delta TA/J)\boldsymbol{u}_n + \mathrm{R}_g(\Delta TA)\boldsymbol{u}_n - \mathrm{R}_g(\Delta TA)\boldsymbol{u}_n.$$

The error $\boldsymbol{e}_n^k := \boldsymbol{u}_n - \boldsymbol{u}_n^k$ thus satisfies for $k \geq 0$ the error equation

$$\boldsymbol{e}_{n+1}^{k+1} = \mathrm{R}_g(\Delta TA)\boldsymbol{e}_n^{k+1} + \left[\mathrm{R}_f^J(\Delta TA/J) - \mathrm{R}_g(\Delta TA)\right]\boldsymbol{e}_n^k, \quad n = 0, 1, \ldots, N_t - 1.$$

For $n = 0$, $\boldsymbol{e}_0^k = 0$, since the initial value is known. Since $A = V_A D V_A^{-1}$, we have

$$\mathrm{R}_g(\Delta TA) = V_A \mathrm{R}_g(\Delta TD)V_A^{-1}, \quad \mathrm{R}_f^J(\Delta TA/J) = V_A \mathrm{R}_f^J(\Delta TD/J)V_A^{-1}.$$

Hence we obtain the error equations in scalar form,

$$\xi_{n+1}^{k+1}(z) = \mathrm{R}_g(z)\xi_n^{k+1}(z) + \left[\mathrm{R}_f^J(z/J) - \mathrm{R}_g(z)\right]\xi_n^k(z), \quad n = 0, 1, \ldots, N_t - 1,$$

where $z = \Delta T\lambda$, with λ being an arbitrary eigenvalue of A, and $\xi_n^k(z)$ is the element of $V_A\boldsymbol{e}_n^k$ corresponding to λ. Clearly we have

$$\|V_A\boldsymbol{e}_n^k\|_\infty = \max_{z\in\sigma(\Delta TA)}|\xi_n^k(z)|. \tag{4.4}$$

Since $\xi_0^k(z) = 0$ for $k \geq 0$, we have $M_g(z)\boldsymbol{\xi}^{k+1}(z) = [M_g(z) - M_f(z)]\boldsymbol{\xi}^k(z)$, which gives

$$\boldsymbol{\xi}^{k+1}(z) = M_g^{-1}(z)[M_g(z) - M_f(z)]\boldsymbol{\xi}^k(z),$$

where $\boldsymbol{\xi}^k(z) = \left(\xi_1^k(z), \xi_2^k(z), \ldots, \xi_{N_t}^k(z)\right)^\top$ for $k \geq 0$. From (4.4) we have

$$\max_{1\leq n\leq N_t}\|V_A\boldsymbol{e}_n^k\|_\infty = \max_{z\in\sigma(\Delta TA)}\max_{1\leq n\leq N_t}|\xi_n^k(z)| = \max_{z\in\sigma(\Delta TA)}\|\boldsymbol{\xi}^k(z)\|_\infty,$$

which completes the proof of (4.2). □

From (4.2), we see that the norm $\|M^k(z)\|_\infty$ represents the convergence factor of the Parareal algorithm when applied to the Dahlquist test equation $u'(t) = \lambda u(t) + g(t)$, where λ is an arbitrary eigenvalue of A.

Remark 4.1. From (4.3) we can interpret the Parareal algorithm from the perspective of a preconditioner by observing that

$$M(z) = I_t - M_g^{-1}(z)M_f(z).$$

For the Dahlquist test equation $u'(t) = \lambda u(t) + g(t)$, the matrix $M_f(z)$ corresponds to the all-at-once matrix of the fine solver $\mathcal{F}$,

$$M_f(z)U = b,$$

where $U = (u_1, u_2, \ldots, u_{N_t})^\top$ and b is an appropriate vector. Parareal can thus be written as

$$M_g(z)\Delta U^k = r^k := b - M_f(z)U^k, \quad U^{k+1} = U^k + \Delta U^k,$$

and the parallelization stems from computing the residual r^k: given U^k from the previous iteration, all components of r^k can be computed simultaneously as

$$r_n^k = b_n - \left(u_n^k - \mathcal{F}\left(T_{n-1}, T_n, u_{n-1}^k\right)\right) = b_n - \left(u_n^k - \mathrm{R}_f^J(z/J)u_{n-1}^k\right).$$

This understanding is valuable for designing new variants of Parareal, and we will revisit this in Section 4.5.

Using $\|M^k(z)\|_\infty$ to predict the convergence behaviour of Parareal is not convenient, so we introduce the results given in Gander and Vandewalle (2007), which provide a very useful estimate of the convergence rate. This involves examining the structure of the matrix $M(z)$. Since

$$M_g^{-1}(z) = \begin{bmatrix} 1 & & & \\ \mathrm{R}_g(z) & 1 & & \\ \vdots & \ddots & \ddots & \\ \mathrm{R}_g^{N_t-1}(z) & \ldots & \mathrm{R}_g(z) & 1 \end{bmatrix},$$

we have

$$M(z) = \left[\mathrm{R}_f^J(z/J) - \mathrm{R}_g(z)\right]\tilde{M}(\mathrm{R}_g(z)),$$

$$\tilde{M}(\beta) := \begin{bmatrix} 0 & & & & \\ 1 & 0 & & & \\ \beta & 1 & 0 & & \\ \vdots & \ddots & \ddots & \ddots & \\ \beta^{N_t-2} & \ldots & \beta & 1 & 0 \end{bmatrix}.$$

This implies that

$$\|M^k(z)\|_\infty = |\mathrm{R}_f^J(z/J) - \mathrm{R}_g(z)|^k \|\tilde{M}^k(\mathrm{R}_g(z))\|_\infty.$$

The infinity norm of the matrix $\tilde{M}^k$ was studied in Gander and Vandewalle (2007, Lemma 4.4), and the main result is

$$\|\tilde{M}^k(\mathrm{R}_g(z))\|_\infty \le \begin{cases} \min\left\{\left(\dfrac{1-|\mathrm{R}_g(z)|^{N_t-1}}{1-|\mathrm{R}_g(z)|}\right)^k, \binom{N_t-1}{k}\right\} & \text{if } |\mathrm{R}_g(z)| < 1, \\ \binom{N_t-1}{k} & \text{if } |\mathrm{R}_g(z)| = 1. \end{cases}$$

Substituting this into (4.2) leads to two different estimates of the convergence rate of the Parareal algorithm.

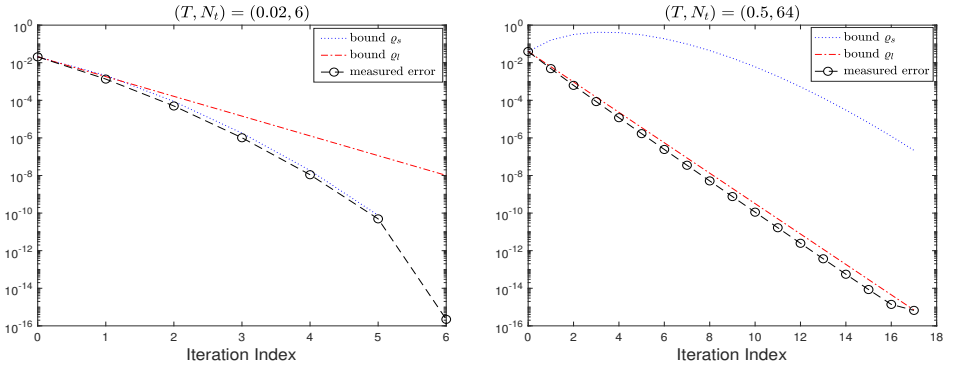

Figure 4.2. Parareal convergence for the heat equation showing its typical two convergence regimes: superlinear convergence over short time intervals and linear convergence over long time intervals.

Theorem 4.2. With the same notation and assumptions used in Theorem 4.1, the error of the kth Parareal iteration satisfies

$$\max_{1\le n\le N_t} \|\boldsymbol{e}_n^k\|_\infty \le \max_{z\in\sigma(\Delta TA)} \varrho_s(J, z, N_t, k) \max_{1\le n\le N_t} \|\boldsymbol{e}_n^0\|_\infty,$$
$$\varrho_s(J, z, N_t, k) := \frac{|\mathrm{R}_g(z) - \mathrm{R}_f^J(z/J)|^k}{k!} \prod_{j=1}^{k} (N_t - j), \tag{4.5a}$$

where $\boldsymbol{e}_n^k = V_A(\boldsymbol{u}_n^k - \boldsymbol{u}_n)$. If $|\mathrm{R}_g(z)| < 1$, for all $z \in \sigma(\Delta TA)$, we obtain

$$\max_{1\le n\le N_t} \|\boldsymbol{e}_n^k\|_\infty \le \max_{z\in\sigma(\Delta TA)} \varrho_l^k(J, z) \max_{1\le n\le N_t} \|\boldsymbol{e}_n^0\|_\infty,$$
$$\varrho_l(J, z) := \frac{|\mathrm{R}_g(z) - \mathrm{R}_f^J(z/J)|}{1 - |\mathrm{R}_g(z)|}. \tag{4.5b}$$

The estimate presented in (4.5a) indicates that Parareal converges superlinearly and completes iterations in at most N_t steps, since $\rho_s = 0$ when $k = N_t$. This estimate is particularly suitable for *short* time intervals where N_t is small. For larger N_t, ρ_s may not provide accurate predictions: initially ρ_s increases, but the error actually decreases uniformly. This is illustrated in Figure 4.2 for the heat equation (2.3) with periodic boundary conditions, $g(x, t) = 0$, and initial value $u(x, 0) = \sin^2(2\pi x)$ for $x \in (0, 1)$. We use in space a very large mesh size $\Delta x = \frac{1}{5}$, and both $\mathcal{F}$ and $\mathcal{G}$ use backward Euler, with a coarsening factor $J = 10$. For $T = 0.02$ and $N_t = 6$, the error decreases at a superlinear rate, and ϱ_s accurately predicts this decrease. However, for a larger T and N_t, the error decreases linearly, and the prediction by ϱ_s is inaccurate. Note that for finer meshes in space (e.g. $\Delta x = \frac{1}{8}$), Parareal converges linearly.

A convergence analysis of Parareal for nonlinear systems of ordinary differential equations using generating functions can be found in Gander and Hairer (2008, Theorem 1); see also Gander and Lunet (2024, Theorem 2.6).

Theorem 4.3. Let $\mathcal{F}$ be the exact propagator and let $\mathcal{G}$ be a time-integrator of order p with its local truncation error bounded by $C_3\Delta T^{p+1}$. Assume that $\mathcal{G}$ satisfies the Lipschitz condition

$$\|\mathcal{G}(T_n, T_n + \Delta T, \boldsymbol{v}) - \mathcal{G}(T_n, T_n + \Delta T, \boldsymbol{w})\| \le (1 + C_2\Delta T)\|\boldsymbol{v} - \boldsymbol{w}\|,$$

and the difference between $\mathcal{G}$ and $\mathcal{F}$ can be expressed, for small ΔT, as

$$\mathcal{F}(T_n, T_{n+1}, \boldsymbol{v}) - \mathcal{G}(T_n, T_{n+1}, \boldsymbol{v}) = c_{p+1}(\boldsymbol{v})\Delta T^{p+1} + c_{p+2}(\boldsymbol{v})\Delta T^{p+2} + \cdots,$$

where the coefficients $c_{p+1}, c_{p+2}, \ldots$ are continuously differentiable functions of $\boldsymbol{v}$. Then the error of Parareal at iteration k is bounded by

$$\|\boldsymbol{u}(T_n) - \boldsymbol{u}_n^k\| \le \frac{C_3\Delta T^{p+1}(C_1\Delta T^{p+1})^{k+1}}{(k+1)!}(1 + C_2\Delta T)^{n-k-1}\prod_{j=0}^{k}(n-j), \qquad (4.6)$$

where $n = 1, 2, \ldots, N_t$ and C_1 is a constant related to the difference between $\mathcal{F}$ and $\mathcal{G}$.

The error estimate (4.6) has a similar consequence to the linear error estimate for short time intervals and small N_t (see (4.5a)): the product term includes a factor of zero, resulting in an error bound of zero, indicating convergence in at most N_t steps. A detailed convergence analysis for Parareal applied to Hamiltonian systems using backward error analysis can be found in Gander and Hairer (2014).

Parareal is highly effective for *diffusive* problems, such as the heat equation shown in Figure 4.2. In particular, for linear systems of ODEs of the form $\boldsymbol{u}'(t) = A\boldsymbol{u}(t) + \boldsymbol{g}(t)$, where A is a negative semi-definite matrix, it can be shown that Parareal has a constant convergence factor around 0.3 for arbitrarily large T and N_t, provided we use backward Euler[5] for $\mathcal{G}$ and $\mathcal{F}$ is an L-stable Runge–Kutta method.

Theorem 4.4. If $\mathcal{G}$ is backward Euler and $\mathcal{F}$ is an L-stable Runge–Kutta method, then

$$\max_{z\in\mathbb{R}^-} \varrho_l(J, z) \approx 0.3 \quad \text{for all } J \ge J_{\min}, \qquad (4.7)$$

where $J_{\min} = O(1)$.

Proof. For the case where $\mathcal{F}$ is backward Euler, this result was established in Mathew, Sarkis and Schaerer (2010). When $\mathcal{F}$ is the trapezoidal rule or BDF2 (i.e. MATLAB's `ode23s` solver) or two singly diagonal implicit Runge–Kutta (SDIRK) methods, proofs can be found in Wu (2015) and Wu and Zhou (2015). For a general L-stable $\mathcal{F}$, the proof can be found in Yang, Yuan and Zhou (2023). □

[5] Note that using backward Euler for $\mathcal{G}$ in Parareal is justified due to the need for a cheap and stable coarse grid correction.

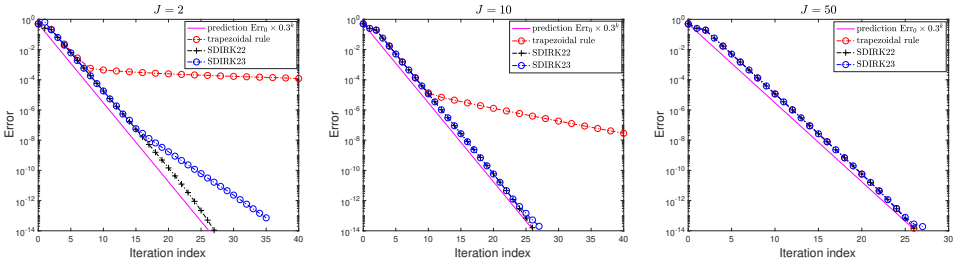

Figure 4.3. Different choices of the fine solver $\mathcal{F}$ lead to different convergence rates for Parareal.

The origins of this result go back to a result already shown in Gander and Vandewalle (2007, Table 5.1) at the continuous level, and for other coarse propagators too, and contraction can be even better, e.g. ≈ 0.068 for Radau IIA.

If $\mathcal{F}$ is only A-stable (not L-stable), e.g. the trapezoidal rule, Parareal does not always have a constant convergence factor. However, for large coarsening factors J, a similar result holds, namely

$$\max_{z\in[0,z_{\max}]} \varrho_I(J,z) \approx 0.3 \quad \text{for all } J \geq J_{\min} = O(\log^2(z_{\max})), \tag{4.8}$$

which was proved for the trapezoidal rule and a fourth-order Gauss Runge–Kutta method in Wu and Zhou (2015). This differs significantly from the scenario where $\mathcal{F}$ is assumed to be the exact solution propagator (i.e. $\mathcal{F} = \exp(\Delta T A)$), where Parareal converges with a rate around 0.3 for $J \geq 2$.

We now illustrate this constant convergence factor by applying Parareal to the heat equation with periodic boundary conditions and discretization and problem parameters $\Delta x = \frac{1}{256}$, $\Delta T = 0.1$, $T = 4$ and $\nu = 0.1$ (the diffusion coefficient). For $\mathcal{F}$ we use the trapezoidal rule and two SDIRK methods given by the Butcher tableau

$$\underbrace{\begin{array}{c|cc} \gamma & \gamma & 0 \\ 1-\gamma & 1-\gamma & \gamma \\ \hline & 1-\gamma & 1-\gamma \end{array}}_{\text{SDIRK22, } \gamma=(2-\sqrt{2})/2}, \qquad \underbrace{\begin{array}{c|cc} \gamma & \gamma & 0 \\ 1-\gamma & \frac{-1}{\sqrt{3}} & \gamma \\ \hline & \frac{1}{2} & \frac{1}{2} \end{array}}_{\text{SDIRK23, } \gamma=(3+\sqrt{3})/6}. \tag{4.9}$$

Here, 'SDIRKsp' denotes an s-stage SDIRK method of order p. For SDIRK22, (4.7) holds for $J_{\min} = 2$ (Wu 2015), and for SDIRK23, $J_{\min} = 4$ (Wu and Zhou 2015). In Figure 4.3 we show the measured error at each iteration for three values of the coarsening factor J. We observe that for small J, these three time-integrators indeed lead to different convergence rates, especially for the trapezoidal rule and the SDIRK23 method, where Parareal converges more slowly. When J is large, say $J = 50$, Parareal converges at a similar rate close to 0.3 for all three time-integrators.

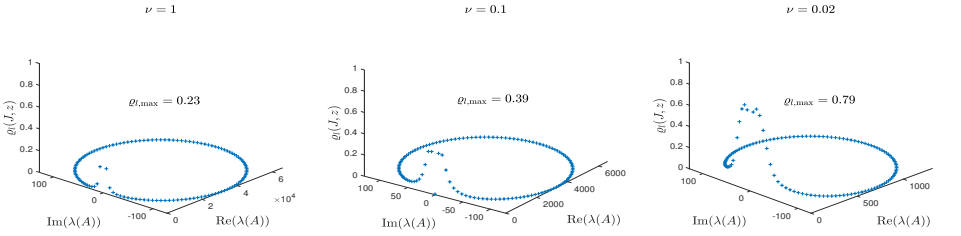

Figure 4.4. The quantity $\varrho_l(J, z)$ for each $z = \Delta T\lambda(A)$ for the advection–diffusion equation with three values of the diffusion parameter ν. As ν decreases, the maximum of ϱ_l approaches 1.

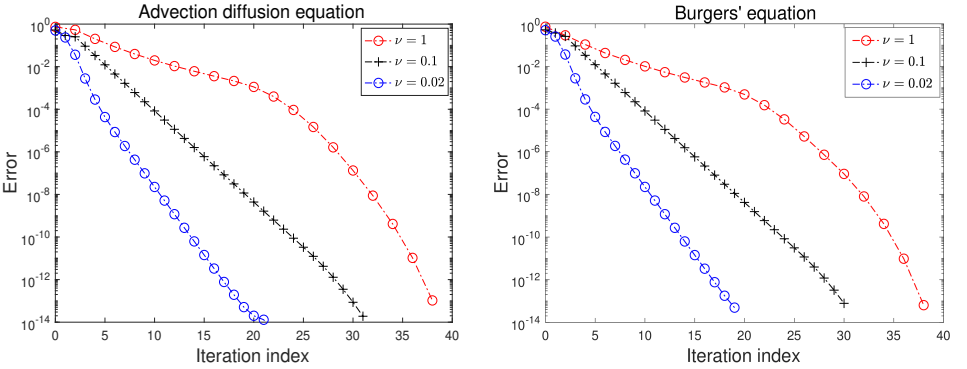

Figure 4.5. Convergence of Parareal applied to (a) the advection–diffusion equation and (b) Burgers' equation with three values of the diffusion parameter ν.

This can be intuitively understood by the fact that for small J the fine integrator that is not L-stable does not resolve the physics accurately enough for high frequencies, and Parareal tries to converge to this incorrect solution with backward Euler as the coarse propagator that represents the correct physics for high frequencies.

While Parareal converges very well for the heat equation and more generally diffusive problems, Parareal is not well-suited to problems that are only weakly diffusive, since its convergence rate continuously deteriorates as the diffusion weakens. We illustrate this for the advection–diffusion equation (2.5) and Burgers' equation (2.6) with periodic boundary conditions, $g(x, t) = 0$, and initial condition $u(x, 0) = \sin(2\pi x)$. We use $T = 4$, $\Delta T = 0.1$, $\Delta x = \frac{1}{128}$ and $J = 32$ for the problem and discretization parameters. The coarse solver is backward Euler, and the fine solver is SDIRK22. For three values of the diffusion parameter ν, we show in Figure 4.4 the quantity $\varrho_l(J, z)$ for each $z = \Delta T\lambda(A)$. As ν decreases, the maximum of ϱ_l grows, indicating that Parareal converges more slowly. This is confirmed in Figure 4.5(a), where we run Parareal on the corresponding problem.

For Burgers' equation we do not have a theoretical analysis as precise as that for the advection–diffusion equation in Figure 4.4, but the results in Figure 4.5(b) show that Parareal also converges ever more slowly for small ν. If we continue to reduce the parameter ν, meaning that the advection term becomes increasingly dominant, Parareal eventually diverges, approximately when $\nu \leq 10^{-3}$, except that the finite step convergence still holds if we iterate for long enough.

For hyperbolic problems, such as the second-order wave equation (2.7), Parareal is also not convergent, as was already shown in Gander and Vandewalle (2007); see also Gander and Lunet (2020*a*,*b*), Gander, Lunet and Pogoželskytė (2023*a*) and Gander, Lunet, Ruprecht and Speck (2023*b*) for more recent and detailed analyses. This degeneration can be attributed to the fact that for hyperbolic problems, as illustrated in Figure 2.4, arbitrarily small high-frequency components, i.e. small oscillations, propagate arbitrarily far in both space and time. Consequently, it becomes very challenging to achieve high-accuracy solutions in the coarse solver $\mathcal{G}$ that are comparable to the fine solver $\mathcal{F}$, in both space and time. If we strive for high accuracy in $\mathcal{G}$, the coarse grid correction becomes rather time-consuming, and we fail to achieve any speed-up.

In the MGRiT community (MGRiT is a multilevel generalization of Parareal; see Section 4.4), considerable research effort has been directed towards making MGRiT work for advection equations; see Howse *et al.* (2019), De Sterck *et al.* (2021), De Sterck, Falgout, Krzysik and Schroder (2023*b*) and De Sterck, Falgout and Krzysik (2023*a*) and references therein. The idea is to design an optimized coarse solver through the so-called semi-Lagrangian discretization. This technique performs well for linear advection equations, while research on the nonlinear case is still ongoing, as the semi-Lagrangian discretization is a characteristics-based method that is not easily realized for nonlinear problems. Another idea, proposed in Gander and Wu (2020), also aims to make Parareal (and MGRiT) work for hyperbolic problems. In this approach it is relatively easy to handle nonlinear problems, as we will see in Section 4.5.

4.3. PFASST

In this and the next two subsections, we present three variants of the Parareal algorithm. We begin by introducing the parallel full approximation scheme in space–time (PFASST), which was proposed in Emmett and Minion (2012). The concept of this method emerged two years earlier when Minion (2010) replaced the fine solver with one iteration of SDC (Dutt *et al.* 2000), in order to reduce the computational cost of one Parareal iteration. PFASST has been successfully applied to several problems (Emmett and Minion 2012, Speck *et al.* 2012, 2014), but a clear description and theoretical analysis of this method are rather challenging. Recently, Bolten, Moser and Speck (2017) described PFASST as a time multigrid method based on an algebraic representation of SDC introduced in Minion *et al.* (2015), and provided a convergence analysis in Bolten, Moser and Speck (2018).

In the formalism of block iterations, PFASST was precisely described and studied for a model problem in Gander *et al.* (2023*b*). In particular, for the system of ODEs (2.1), a two-level variant of PFASST can be described as follows: we first partition the time interval $(0, T)$ into N_t large subintervals $[T_0, T_1] \cup [T_1, T_2] \cup \cdots \cup [T_{N_t-1}, T_{N_t}]$ with $T_0 = 0$, $T_{N_t} = T$ and $T_n = n\Delta t$. For each subinterval, e.g. the nth subinterval $[T_n, T_{n+1}]$, we define M_f and M_c time points

$$\begin{cases} \{t^f_{n,m} \coloneqq T_n + \tau^f_m \Delta t\}, \ m = 0, 1, \ldots, M_f \text{ and } \tau^f_0 = 0, \ \tau^f_{M_f} = 1, \\ \{t^c_{n,m} \coloneqq T_n + \tau^c_m \Delta t\}, \ m = 0, 1, \ldots, M_c \text{ and } \tau^c_0 = 0, \ \tau^c_{M_c} = 1, \end{cases}$$

where $M_f > M_c$. Here we use the superscript 'f' and 'c' to denote the fine and the coarse time grids. Then we solve (2.1) for $t \in [T_n, T_{n+1}]$ by numerical quadrature as

$$\boldsymbol{u}_{n,m} = \boldsymbol{u}_{n,0} + \Delta t \sum\nolimits_{j=1}^{M} q_{m,j}(A\boldsymbol{u}_{n,j} + \boldsymbol{g}(t_{n,j})), \quad m = 1, 2, \ldots, M, \tag{4.10}$$

where $\boldsymbol{u}_{n,j}$ is an approximation of $\boldsymbol{u}$ at $t = t_{n,j}$. Here $M = M_f$ or M_c, $t_{n,j} = t^f_{n,j}$ or $t^c_{n,j}$. We represent (4.10) as

$$\boldsymbol{u}_n = \Delta t(Q \otimes A)\boldsymbol{u}_n + \boldsymbol{\chi}\boldsymbol{u}_{n-1} + \Delta t \boldsymbol{b}_n,$$

where

$$Q \coloneqq (q_{m,j}), \quad \boldsymbol{u}_n \coloneqq \left(u^\top_{n,1}, u^\top_{n,2}, \ldots, u^\top_{n,M}\right)^\top, \quad \boldsymbol{b}_n \coloneqq (Q \otimes I_x)\boldsymbol{g}_n$$

and $\boldsymbol{\chi}$ is the block 'copying' matrix $\boldsymbol{\chi} \coloneqq \chi \otimes I_x$ with

$$\chi \coloneqq \begin{bmatrix} 0 & \cdots & 0 & 1 \\ 0 & \cdots & 0 & 1 \\ \vdots & \cdots & \vdots & \vdots \\ 0 & \cdots & 0 & 1 \end{bmatrix} \in \mathbb{R}^{M \times M}, \quad \boldsymbol{g}_n \coloneqq \begin{bmatrix} \boldsymbol{g}(t_{n,1}) \\ \boldsymbol{g}(t_{n,2}) \\ \vdots \\ \boldsymbol{g}(t_{n,M}) \end{bmatrix}.$$

Hence, for the fine and coarse time grids we have

$$\begin{aligned} \boldsymbol{u}^f_n &= \boldsymbol{\phi}_f^{-1}\left(\boldsymbol{\chi}_f \boldsymbol{u}^f_{n-1} + \Delta t \boldsymbol{b}^f_n\right), \quad & \boldsymbol{u}^c_n &= \boldsymbol{\phi}_c^{-1}(\boldsymbol{\chi}_c \boldsymbol{u}^c_{n-1} + \Delta t \boldsymbol{b}^c_n), \\ \boldsymbol{\phi}_f &\coloneqq \boldsymbol{I}_f - \Delta t Q_f \otimes A, & \boldsymbol{\phi}_c &\coloneqq \boldsymbol{I}_c - \Delta t Q_c \otimes A, \end{aligned}$$

where $n = 1, 2, \ldots, N_t$, $\boldsymbol{I}_c = I_{M_c} \otimes I_x$ and $\boldsymbol{I}_f = I_{M_f} \otimes I_x$.

For PFASST, we need transfer matrices $\mathbf{T}^{c \to f}$ and $\mathbf{T}^{f \to c}$, which prolongate and restrict vectors defined on the coarse and fine time grids. These transfer matrices are defined via Lagrange interpolation,

$$\begin{aligned} p^c(\tau; \boldsymbol{u}^c) &= \sum_{m=1}^{M_c} u^c_m L^c_m(\tau), \quad & L^c_m(\tau) &\coloneqq \frac{\prod_{j=1, j\neq m}^{M_c}(\tau - \tau^c_m)}{\prod_{j=1, j\neq m}^{M_c}(\tau^c_j - \tau^c_m)}, \\ p^f\left(\tau; \boldsymbol{u}^f\right) &= \sum_{m=1}^{M_f} u^f_m L^f_m(\tau), \quad & L^f_m(\tau) &\coloneqq \frac{\prod_{j=1, j\neq m}^{M_f}\left(\tau - \tau^f_m\right)}{\prod_{j=1, j\neq m}^{M_f}\left(\tau^f_j - \tau^f_m\right)}, \end{aligned}$$

where L_m^c and L_m^f are the mth basis function specified by the coarse and fine interpolation nodes. The function p^c is evaluated at the fine nodes $\{\tau_m^f\}$ and the function p^f is evaluated at the coarse nodes $\{\tau_m^c\}$. Specifically,

$$\begin{bmatrix} p^c(\tau_1^f;\boldsymbol{u}^c) \\ p^c(\tau_2^f;\boldsymbol{u}^c) \\ \vdots \\ p^c(\tau_{M_f}^f;\boldsymbol{u}^c) \end{bmatrix} = \underbrace{\left(\begin{bmatrix} L_1^c(\tau_1^f) & L_2^c(\tau_1^f) & \cdots & L_{M_c}^c(\tau_1^f) \\ L_1^c(\tau_2^f) & L_2^c(\tau_2^f) & \cdots & L_{M_c}^c(\tau_2^f) \\ \vdots & \vdots & \cdots & \vdots \\ L_1^c(\tau_{M_f}^f) & L_2^c(\tau_{M_f}^f) & \cdots & L_{M_c}^c(\tau_{M_f}^f) \end{bmatrix} \otimes I_x \right)}_{=:\mathbf{T}^{c\to f}\in\mathbb{R}^{M_fN_x\times M_cN_x}} \boldsymbol{u}^c.$$

The matrix $\mathbf{T}^{f\to c} \in \mathbb{R}^{M_cN_x\times M_fN_x}$ is defined similarly.

With the above notation, according to Gander *et al.* (2023*b*), PFASST can be written as

$$\boldsymbol{u}_{n+1}^{k+1} = \mathbf{B}_1^0\boldsymbol{u}_{n+1}^k + \mathbf{B}_0^1\big(\chi\boldsymbol{u}_n^{k+1} + \Delta t\boldsymbol{b}_n^f\big) + \mathbf{B}_0^0\big(\chi\boldsymbol{u}_n^k + \Delta t\boldsymbol{b}_n^f\big),$$

where

$$\begin{aligned} \mathbf{B}_1^0 &= [\boldsymbol{I}_f - \mathbf{T}^{c\to f}\boldsymbol{\phi}_c^{-1}\mathbf{T}^{f\to c}\boldsymbol{\phi}_f]\big(\boldsymbol{I}_f - \tilde{\boldsymbol{\phi}}_f^{-1}\boldsymbol{\phi}_f\big), \\ \mathbf{B}_0^1 &= \mathbf{T}^{c\to f}\boldsymbol{\phi}_c^{-1}\mathbf{T}^{f\to c}, \\ \mathbf{B}_0^0 &= [\boldsymbol{I}_f - \mathbf{T}^{c\to f}\boldsymbol{\phi}_c^{-1}\mathbf{T}^{f\to c}\boldsymbol{\phi}_f]\tilde{\boldsymbol{\phi}}_f^{-1}, \end{aligned}$$

and $\tilde{\boldsymbol{\phi}}_f$ is an approximation of $\boldsymbol{\phi}_f$. In practice, we construct $\tilde{\boldsymbol{\phi}}_f$ by using an implicit Euler method on the time points $\{t_{n,m}^f\}$:

$$\frac{\boldsymbol{u}_{n,m+1} - \boldsymbol{u}_{n,m}}{\Delta t(\tau_{m+1}^f - \tau_m^f)} = A\boldsymbol{u}_{n,m+1} + \boldsymbol{g}\big(t_{n,m+1}^f\big), \quad m = 0, 1, \ldots, M_f - 1, \tag{4.11}$$

that is,

$$\tilde{\boldsymbol{\phi}}_f = \begin{bmatrix} 1 & & & \\ -1 & 1 & & \\ & \ddots & \ddots & \\ & & -1 & 1 \end{bmatrix} \otimes I_x - \Delta t \begin{bmatrix} \tau_1^f - \tau_0^f & & & \\ & \tau_2^f - \tau_1^f & & \\ & & \ddots & \\ & & & \tau_{M_f}^f - \tau_{M_f-1}^f \end{bmatrix} \otimes A.$$

We now apply PFASST to the heat equation (2.3) and the advection–diffusion equation (2.5) with $T = 3$, periodic boundary conditions and initial value $u(x, 0) = 0$. The source term $g(x, t)$ for the two PDEs is given by (2.4) with $\sigma = 1000$ and the space–time mesh size is $\Delta x = \frac{1}{128}$, $\Delta t = \frac{1}{64}$. For the numerical quadrature (4.10), we use the Radau IIA method for both fine and coarse nodes with $M_f = 3$ and $M_c = 2$. The nodes are

$$\{\tau_m^f\} := \left\{0, \frac{4-\sqrt{6}}{10}, \frac{4+\sqrt{6}}{10}, 1\right\}, \quad \{\tau_m^c\} := \left\{0, \frac{1}{3}\, 1\right\},$$

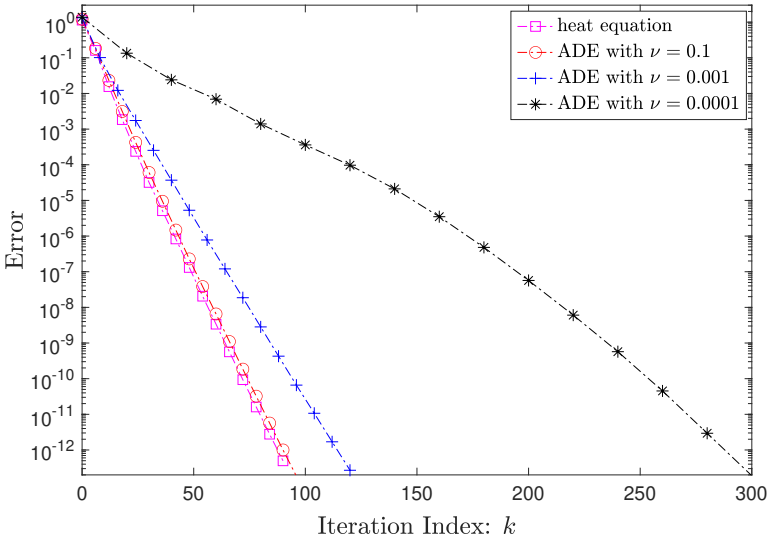

Figure 4.6. Measured error of PFASST for the heat equation and the advection–diffusion equation (ADE) with three diffusion parameters.

and the corresponding weight matrices Q_f and Q_c are

$$Q_f := \begin{bmatrix} \frac{88-7\sqrt{6}}{360} & \frac{296-169\sqrt{6}}{1800} & \frac{-2+3\sqrt{6}}{225} \\ \frac{296+169\sqrt{6}}{1800} & \frac{88+7\sqrt{6}}{360} & \frac{-2-3\sqrt{6}}{225} \\ \frac{16-\sqrt{6}}{36} & \frac{16+\sqrt{6}}{36} & \frac{1}{9} \end{bmatrix}, \quad Q_c := \begin{bmatrix} \frac{5}{12} & -\frac{1}{12} \\ \frac{3}{4} & \frac{1}{4} \end{bmatrix}.$$

Then the two transfer matrices are

$$\mathbf{T}^{c\to f} = \begin{bmatrix} 1.2674 & -0.2674 \\ 0.5325 & 0.4674 \\ 0 & 1 \end{bmatrix} \otimes I_x, \quad \mathbf{T}^{f\to c} = \begin{bmatrix} 0.5018 & 0.6833 & -0.1851 \\ 0 & 0 & 1 \end{bmatrix} \otimes I_x.$$

In Figure 4.6 we show the measured error of PFASST for the heat equation and the advection–diffusion equation with three diffusion parameters. We see that the convergence rate also deteriorates when the diffusion in the PDE becomes weak, as in Parareal and MGRiT, seen earlier.

4.4. MGRiT

Multigrid reduction in time (MGRiT) is another variant of Parareal, introduced by Falgout *et al.* (2014). MGRiT can be interpreted in different ways, such as an algebraic multigrid method with the so-called FCF-relaxation, a block iteration (Gander *et al.* 2023*b* and Gander and Lunet 2024, Chapter 4.6), or as an overlapping Parareal variant (Gander *et al.* 2018*b*, Theorem 4 and Corollary 1). Here we present

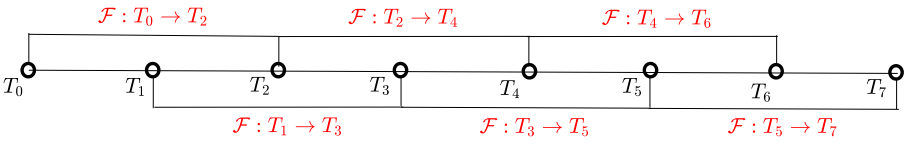

Figure 4.7. Geometric representation of MGRiT with FCF-relaxation as an overlapping variant of Parareal. The dark circles represent the coarse time points where the coarse solver $\mathcal{G}$ runs.

MGRiT as an overlapping variant of Parareal applied to nonlinear systems of ODEs (2.2), i.e. $\boldsymbol{u}' = f(\boldsymbol{u}, t)$ with initial value $\boldsymbol{u}(0) = \boldsymbol{u}_0$. MGRiT with two levels and FCF-relaxation then corresponds to the iteration

$$\begin{aligned} \boldsymbol{u}_0^{k+1} &= \boldsymbol{u}_0,\ \boldsymbol{u}_1^{k+1} = \mathcal{F}(T_0, T_1, \boldsymbol{u}_0), \\ \boldsymbol{u}_{n+1}^{k+1} &= \mathcal{F}\big(T_n, T_{n+1}, \mathcal{F}\big(T_{n-1}, T_n, \boldsymbol{u}_{n-1}^k\big)\big) + \mathcal{G}\big(T_n, T_{n+1}, \boldsymbol{u}_n^{k+1}\big) \\ &\quad - \mathcal{G}\big(T_n, T_{n+1}, \mathcal{F}\big(T_{n-1}, T_n, \boldsymbol{u}_{n-1}^k\big)\big), \end{aligned} \tag{4.12}$$

where $n = 1, 2, \ldots, N_t - 1$, and $\mathcal{G}$ and $\mathcal{F}$ are the coarse and fine time propagators used in Parareal (see (4.1)). We see from (4.12) that MGRiT with FCF-relaxation costs two fine solves in each iteration, compared to only one fine solve in Parareal. A geometric representation of MGRiT with FCF-relaxation is shown in Figure 4.7, illustrating that two-level MGRiT with FCF relaxation is a Parareal algorithm with overlap size ΔT, and it thus also converges in a finite number of iterations, that is, the global error decays to zero after at most $k = \lceil N_t/2 \rceil$ iterations (Gander *et al.* 2018*b*, Theorem 5). A superlinear convergence result for two-level MGRiT applied to nonlinear problems with more general F(CF)$^\nu$-relaxation, $\nu = 1, 2, \ldots$, can be found in Gander *et al.* (2018*b*, Theorem 6), and it is shown that this corresponds to Parareal with ν coarse time interval ΔT overlap; see Gander *et al.* (2018*b*, Corollary 1).

In the linear case, a linear convergence estimate can be found in Dobrev *et al.* (2017), which we now show. We consider the linear system of ODEs (2.1), i.e. $\boldsymbol{u}' = A\boldsymbol{u} + \boldsymbol{g}$ with initial value $\boldsymbol{u}(0) = \boldsymbol{u}_0$, where we assume that A is diagonalizable with spectrum $\sigma(A) \subset \mathbb{C}^-$.

Theorem 4.5 (Dobrev *et al.* 2017). With the same notation and assumptions as in Theorem 4.2, MGRiT with FCF-relaxation satisfies the convergence estimate

$$\begin{aligned} \max_{1\le n\le N_t} \|\boldsymbol{e}_n^k\|_\infty &\le \max_{z\in\sigma(\Delta T A)} \varrho_l^k(J, z) \max_{1\le n\le N_t} \|\boldsymbol{e}_n^0\|_\infty, \\ \varrho_l(J, z) &:= \frac{|\mathrm{R}_f^J(z/J)||\mathrm{R}_g(z) - \mathrm{R}_f^J(z/J)|}{1 - |\mathrm{R}_g(z)|}, \end{aligned} \tag{4.13}$$

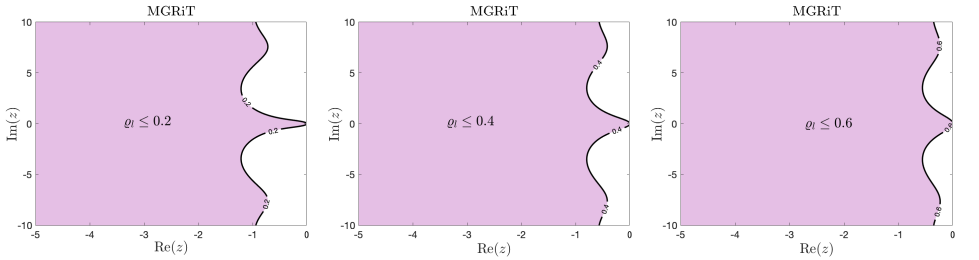

(a)

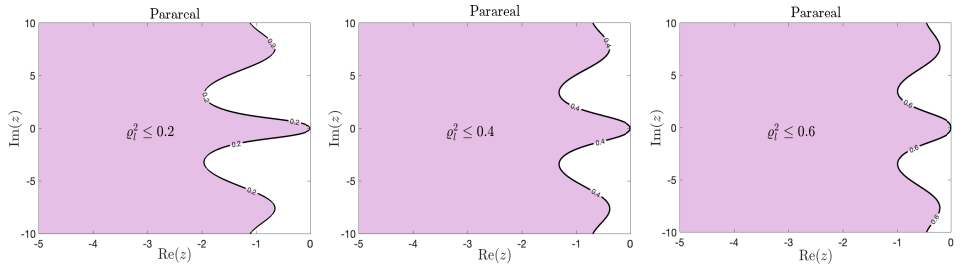

(b)

Figure 4.8. The regions where $\varrho_l \le \hat{\varrho}$ in the left half of the complex plane for MGRiT with FCF-relaxation (a) and Parareal (b).

where R_g and R_f are the stability functions of the coarse solver $\mathcal{G}$ and the fine solver $\mathcal{F}$, $\boldsymbol{e}_n^k := V_A(\boldsymbol{u}_n^k - \boldsymbol{u}_n)$, and the coarse solver $\mathcal{G}$ is stable in the sense that $|\mathrm{R}_g(z)| < 1$ for $z \in \sigma(\Delta T A)$.

The quantity ϱ_l in (4.13) is the *linear* convergence factor of MGRiT for long-time computations when applied to linear problems. Letting $\varrho_{l,\text{parareal}}$ denote the convergence factor of Parareal (see (4.5b)) and $\varrho_{l,\text{mgrit}}$ the convergence factor of MGRiT, we obtain

$$\varrho_{l,\text{mgrit}} = |\mathrm{R}_f^J(z/J)| \times \varrho_{l,\text{parareal}}.$$

In practice, the fine solver $\mathcal{F}$ is stable, i.e. $|\mathrm{R}_f(z)| \le 1$ for all $z \in \sigma(\Delta T A)$, and thus each additional CF relaxation adds a further contraction to MGRiT compared to Parareal, but each such relaxation again costs an expensive fine parallel solve. To illustrate this, in Figure 4.8 we show the regions where $\varrho_{l,\text{mgrit}} \le \hat{\varrho}$ and $\varrho_{l,\text{parareal}}^2 \le \hat{\varrho}$ with $\hat{\varrho} = 0.2, 0.4, 0.6$ in the left half of the complex plane (i.e. $z \in \mathbb{C}^-$) for Parareal and MGRiT.[6] Here, we chose backward Euler for $\mathcal{G}$ and the exact time-integrator $\mathcal{F} = \exp(\Delta T A)$ for $\mathcal{F}$. The stability functions of these two solvers are $\mathrm{R}_g(z) = 1/(1-z)$ and $\mathrm{R}_f(z) = \mathrm{e}^z$. We see that for a given upper bound $\hat{\varrho}$, the

[6] For a fair comparison, we compare two Parareal iterations with one MGRiT iteration with FCF relaxation, since both then use two fine solves.

regions where $\varrho_{l,\text{mgrit}} \le \hat{\varrho}$ are comparable to those where $\varrho^s_{l,\text{parareal}} \le \hat{\varrho}$. For other fine time solvers, such as the two SDIRK methods in (4.9), the results look similar, and the above conclusion holds as well.

A more quantitative comparison for the case $z \in \mathbb{R}^-$ is as follows.

Theorem 4.6 (Wu and Zhou 2019). Suppose we use an L-stable time-integrator for $\mathcal{F}$ and the ratio between ΔT and Δt, i.e. $J = \Delta T/\Delta t$, satisfies $J = O(1)$. Then, if we use the backward Euler method for $\mathcal{G}$,

$$\max_{z\ge 0}\varrho_l \approx \begin{cases} 0.2984, & \text{Parareal,} \\ 0.1115, & \text{MGRiT with FCF-relaxation.} \end{cases}$$

If we use the LIIIC-2 method (i.e. the second-order Lobatto IIIC Runge–Kutta method) for $\mathcal{G}$,

$$\max_{z\ge 0}\varrho_l \approx \begin{cases} 0.0817, & \text{Parareal,} \\ 0.0197, & \text{MGRiT with FCF-relaxation.} \end{cases}$$

Therefore, when using backward Euler for $\mathcal{G}$, the convergence factor of one MGRiT iteration with FCF-relaxation is a bit worse than the convergence factor of two Parareal iterations ($0.2984^2 = 0.0890 < 0.1115$ and $0.0817^2 = 0.0067 < 0.0197$), and the cost in fine solves of one MGRiT iteration with FCF-relaxation is the same as the cost of two Parareal iterations.

We now compare the convergence rates of Parareal and MGRiT by applying them to the heat equation (2.3) and the advection–diffusion equation (2.5). We impose homogeneous Dirichlet boundary conditions for the heat equation and periodic boundary conditions for ADE. For both PDEs the initial condition is $u(x,0) = \sin^2(8\pi(1-x)^2)$ for $x \in (0,1)$. The problem and discretization parameters are $T = 5$, $J = 20$, $\Delta T = \frac{1}{8}$ and $\Delta x = \frac{1}{160}$. For $\mathcal{G}$ we use backward Euler, and for $\mathcal{F}$ we use SDIRK22 from (4.9). In Figure 4.9, for both the heat equation and the advection–diffusion equation with two different values of the diffusion parameter ν, we show the quantity $\varrho_l(J,z)$ for $z \in \sigma(\Delta T A)$. The maximum, denoted by $\varrho_{l,\max} := \max_{z\in\sigma(\Delta T A)}\varrho_l(J,z)$, represents the convergence factor for the two methods. It is evident that for the heat equation and the ADE with $\nu = 0.1$, the convergence factor of MGRiT with FCF-relaxation is approximately equal to the square of that of Parareal, indicating that MGRiT with FCF-relaxation converges twice as fast as Parareal, but also at twice the cost, since it uses two $\mathcal{F}$ solves and Parareal only one, which is consistent with Theorem 4.6. For ADE with $\nu = 0.01$, the convergence factors of both MGRiT and Parareal are close to 1, indicating very slow convergence for both. This is due to the fact that the coarse propagator is no longer good enough for small ν when advection dominates. Note also that this has a greater impact for Parareal, which uses the coarse propagator after each fine solve (see (4.1)), whereas MGRiT with FCF-relaxation performs two consecutive fine solves without a coarse solve in between (see (4.12)). In Figure 4.10 we present the measured errors for the two methods, where we plot for Parareal each double

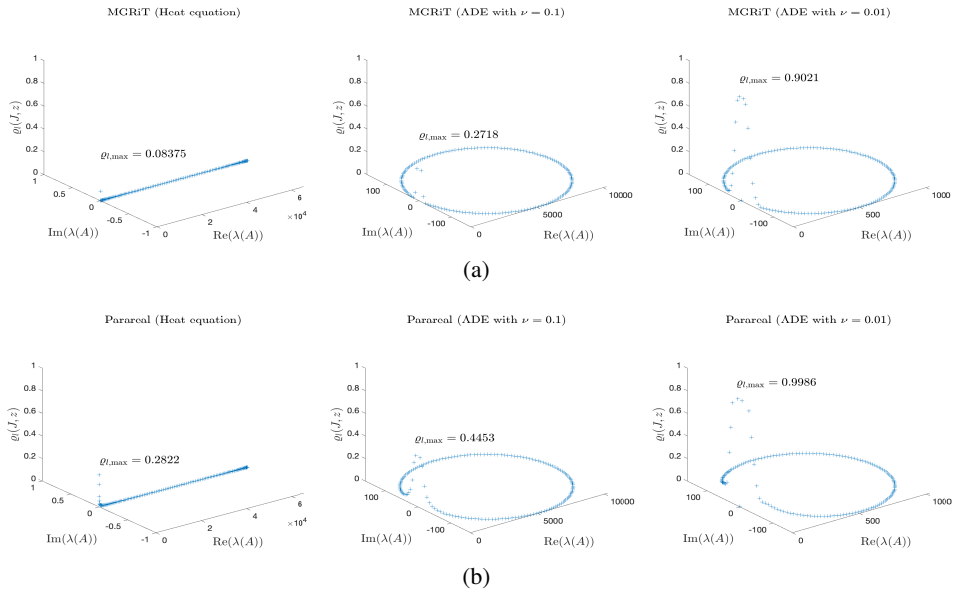

Figure 4.9. The distribution of $\varrho_l(J, z)$ for $z \in \sigma(\Delta T A)$ for the heat equation and the advection–diffusion equation (ADE) with two values of the diffusion parameter ν. (a) MGRiT, (b) Parareal. In each panel, $\varrho_{l,\max} = \max_{z\in\sigma(\Delta T A)} \varrho_l(z)$.

iteration as one, in order to use two fine solves, as in MGRiT with FCF-relaxation. We see that for the heat equation and ADE with $\nu = 0.1$, convergence of Parareal and MGRiT is very similar, as expected, but with advection convergence is worse. This is confirmed for ADE with $\nu = 0.01$, where both MGRiT with FCF-relaxation and Parareal now converge very slowly, and we observe that Parareal deterioration is more pronounced due to the use of the ineffective coarse solve after each fine solve, as indicated by the analysis. Finally, for $\nu = 0.002$, both Parareal and MGRiT diverge; the corresponding values are $\varrho_{l,\max} = 1.4211$ for Parareal and $\varrho_{l,\max} = 1.2812$ for MGRiT. These results clearly show convergence problems of both methods when approaching the hyperbolic regime.

Like Parareal, MGRiT can also be applied to nonlinear problems, where $\mathcal{G}$ and $\mathcal{F}$ require the use of some nonlinear solver. A convergence analysis of MGRiT for nonlinear cases can be found in Gander *et al.* (2018*b*), under the assumption of certain Lipschitz conditions for $\mathcal{G}$, $\mathcal{F}$, and their difference. The main conclusion is as follows: one MGRiT iteration with FCF-relaxation (thus using two fine solves) contracts similarly to two Parareal iterations (also using two fine solves) as long as the coarse solver $\mathcal{G}$ is reasonably accurate. To illustrate this, we apply MGRiT with FCF-relaxation and Parareal to Burgers' equation (2.6) with homogeneous Dirichlet boundary conditions and initial condition $u(x, 0) = \sin^2(8\pi(1 - x)^2)$ for $x \in (0, 1)$, $T = 5$ and discretization parameters $\Delta T = \frac{1}{16}$, $\Delta x = \frac{1}{160}$ and $J = 10$. We use centred

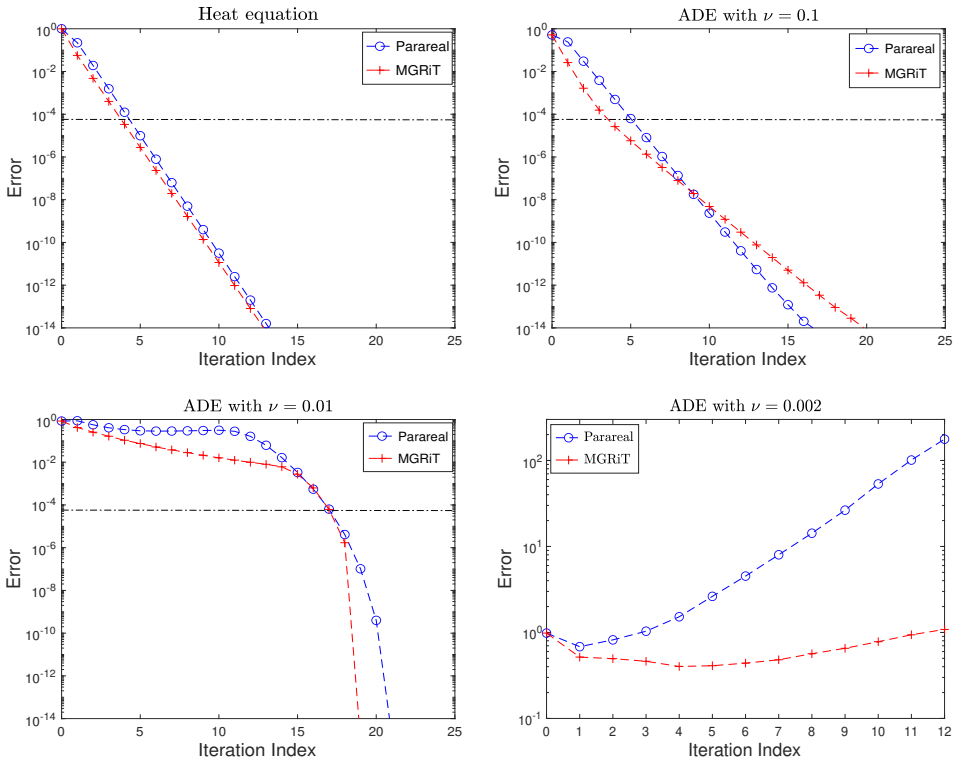

Figure 4.10. Measured errors for Parareal and MGRiT for the heat equation and the advection–diffusion equation (ADE) with three values of the diffusion parameter ν. The dash-dotted line in each panel indicates the order of the truncation error $\max\{\Delta t^2, \Delta x^2\}$ of the discretization, beyond which one would not iterate in practice.

finite differences for the space discretization, and for the time discretization we use backward Euler for $\mathcal{G}$ and SDIRK22 (4.9) for $\mathcal{F}$. In Figure 4.11 we show the errors for three values of the diffusion parameter ν, again plotting a double iteration of Parareal for one iteration of MGRiT with FCF-relaxation to measure the same number of fine solves. We see that for each ν, MGRiT converges like two steps of Parareal again, as for the linear problems in Figure 4.10.

4.5. Diagonalization-based Parareal

The third variant of Parareal we want to explain uses ParaDiag in the coarse grid correction (CGC). There are two approaches. The first uses a head–tail coupled condition to permit the CGC to be solved in one shot with ParaDiag; see Wu (2018) and Wu and Zhou (2019). The second involves designing a special coarse solver that closely approximates the fine solver, but can be applied at low cost for each

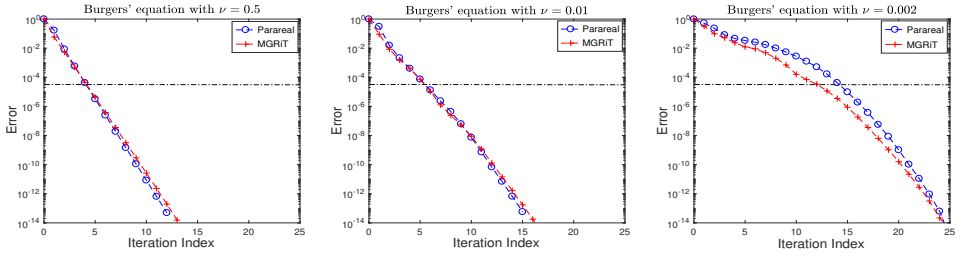

Figure 4.11. Error of Parareal and MGRiT for Burgers' equation (2.6) with three values of the diffusion parameter ν.

large time interval $[T_n, T_{n+1}]$ using ParaDiag (see Gander and Wu 2020). The two Parareal variants have distinct mechanisms, convergence properties and scopes of application.

4.5.1. Diagonalization-based CGC

For the initial-value problem $\boldsymbol{u}' = f(\boldsymbol{u})$ with $\boldsymbol{u}(0) = \boldsymbol{u}_0$, the standard CGC for Parareal follows a sequential procedure. Specifically, we solve for $\{\boldsymbol{u}_n^{k+1}\}$ step by step as

$$\boldsymbol{u}_{n+1}^{k+1} = \mathcal{G}\big(T_n, T_{n+1}, \boldsymbol{u}_n^{k+1}\big) + \boldsymbol{b}_{n+1}^{k}, \quad n = 0, 1, \ldots, N_t - 1, \tag{4.14}$$

starting from the initial condition $\boldsymbol{u}_0^{k+1} = \boldsymbol{u}_0$, where

$$\boldsymbol{b}_{n+1}^{k} = \mathcal{F}\big(T_n, T_{n+1}, \boldsymbol{u}_n^{k}\big) - \mathcal{G}\big(T_n, T_{n+1}, \boldsymbol{u}_n^{k}\big)$$

is determined from the previous iteration. The idea in Wu (2018) was to impose a head–tail-type coupling condition $\boldsymbol{u}_0^{k+1} = \alpha \boldsymbol{u}_{N_t}^{k+1} + \boldsymbol{u}_0$ for the CGC. This is different from the more natural head–tail condition we saw in ParaDiag II in (3.55), which appeared a year later in Gander and Wu (2019), but turned out to work equally well in the present context. To use this head–tail-type coupling condition, we must redefine $\boldsymbol{b}_{n+1}^{k}$ as

$$\boldsymbol{b}_{n+1}^{k} = \mathcal{F}\big(T_n, T_{n+1}, \tilde{\boldsymbol{u}}_n^{k}\big) - \mathcal{G}\big(T_n, T_{n+1}, \boldsymbol{u}_n^{k}\big),$$

where

$$\tilde{\boldsymbol{u}}_n^{k} = \begin{cases} \boldsymbol{u}_n^{k}, & \text{if } n \geq 1, \\ \boldsymbol{u}_0, & \text{if } n = 0. \end{cases}$$

This redefinition is necessary to ensure that the iterates converge to the solution of the underlying ODEs. In summary, the Parareal variant proposed in Wu (2018) with this head–tail-type coupling condition is

$$\begin{aligned} \boldsymbol{u}_{n+1}^{k+1} &= \mathcal{G}\big(T_n, T_{n+1}, \boldsymbol{u}_n^{k+1}\big) + \mathcal{F}\big(T_n, T_{n+1}, \tilde{\boldsymbol{u}}_n^{k}\big) - \mathcal{G}\big(T_n, T_{n+1}, \boldsymbol{u}_n^{k}\big), \\ \boldsymbol{u}_0^{k+1} &= \alpha \boldsymbol{u}_{N_t}^{k+1} + \boldsymbol{u}_0, \end{aligned} \tag{4.15}$$

where $n = 0, \ldots, N_t - 1$.

We first explain how to implement this variant of Parareal for the system of linear ODEs $\boldsymbol{u}' = A\boldsymbol{u}$ with initial condition $\boldsymbol{u}(0) = \boldsymbol{u}_0$ and $t \in (0, T)$; the nonlinear case will be addressed at the end of this section. We use backward Euler for the coarse solver $\mathcal{G}$ and an arbitrary one-step time-integrator for the fine solver $\mathcal{F}$. By noting that $\mathcal{G}(T_n, T_{n+1}, \boldsymbol{u}_n^{k+1}) = (I_x - \Delta T A)^{-1}\boldsymbol{u}_n^{k+1}$, the new CGC (4.15) involves solving the N_t linear equations

$$\begin{cases} (I_x - \Delta T A)\boldsymbol{u}_1^{k+1} = \boldsymbol{u}_0^{k+1} + (I_x - \Delta T A)\boldsymbol{b}_1^k, \\ (I_x - \Delta T A)\boldsymbol{u}_2^{k+1} = \boldsymbol{u}_1^{k+1} + (I_x - \Delta T A)\boldsymbol{b}_2^k, \\ \vdots \\ (I_x - \Delta T A)\boldsymbol{u}_{N_t}^{k+1} = \boldsymbol{u}_{N_t-1}^{k+1} + (I_x - \Delta T A)\boldsymbol{b}_{N_t}^k, \\ \boldsymbol{u}_0^{k+1} = \alpha\boldsymbol{u}_{N_t}^{k+1} + \boldsymbol{u}_0, \end{cases}$$

where $\boldsymbol{b}_{n+1}^k = \mathcal{F}(T_n, T_{n+1}, \tilde{\boldsymbol{u}}_n^k) - \mathcal{G}(T_n, T_{n+1}, \boldsymbol{u}_n^k)$ is known from the previous iteration. Note that these linear systems cannot be solved one by one due to the head–tail coupling condition $\boldsymbol{u}_0^{k+1} = \alpha\boldsymbol{u}_{N_t}^{k+1} + \boldsymbol{u}_0$. Substituting this condition into the first equation leads to the all-at-once system

$$(C_\alpha \otimes I_x - I_t \otimes \Delta T A)\boldsymbol{U}^{k+1} = \boldsymbol{g}^k, \tag{4.16}$$

where

$$\boldsymbol{U}^{k+1} = \left(\left(\boldsymbol{u}_1^{k+1}\right)^\top, \left(\boldsymbol{u}_2^{k+1}\right)^\top, \ldots, \left(\boldsymbol{u}_{N_t}^{k+1}\right)^\top\right)^\top$$

and

$$C_\alpha = \begin{bmatrix} 1 & & & -\alpha \\ -1 & 1 & & \\ & \ddots & \ddots & \\ & & -1 & 1 \end{bmatrix} \in \mathbb{R}^{N_t \times N_t}, \quad \boldsymbol{g}^k = \begin{bmatrix} \boldsymbol{u}_0 + (I_x - \Delta T A)\boldsymbol{b}_1^k \\ (I_x - \Delta T A)\boldsymbol{b}_2^k \\ \vdots \\ (I_x - \Delta T A)\boldsymbol{b}_{N_t}^k \end{bmatrix}.$$

Similarly to the ParaDiag II methods introduced in Section 3.5.2, we can solve for $\boldsymbol{U}^{k+1}$ using three steps,

$$\begin{cases} \boldsymbol{U}^{a,k+1} = (\mathrm{F} \otimes I_x)\boldsymbol{g}^k, & \text{(step a)} \\ (\lambda_n I_x - \Delta T A)\boldsymbol{u}_n^{b,k+1} = \boldsymbol{u}_n^{a,k+1}, \ n = 1, 2, \ldots, N_t, & \text{(step b)} \\ \boldsymbol{U}^{k+1} = (\mathrm{F}^* \otimes I_x)\boldsymbol{U}^{b,k+1}, & \text{(step c)} \end{cases} \tag{4.17}$$

where $\{\lambda_n\}$ are the eigenvalues of C_α (see (3.51)), F is the discrete Fourier matrix (see (3.50)), and

$$\boldsymbol{U}^{a,k+1} := \left(\left(\boldsymbol{u}_1^{a,k+1}\right)^\top, \ldots, \left(\boldsymbol{u}_{N_t}^{a,k+1}\right)^\top\right)^\top$$

along with

$$\boldsymbol{U}^{b,k+1} := \left(\left(\boldsymbol{u}_1^{b,k+1}\right)^\top, \ldots, \left(\boldsymbol{u}_{N_t}^{b,k+1}\right)^\top\right)^\top.$$

Through the diagonalization procedure (4.17), the new CGC (4.15) can be solved in parallel across the coarse time grid.

From (4.15) we see that the head–tail coupled CGC simplifies to the standard CGC (4.14) when $\alpha \to 0$, and hence we can expect that for sufficiently small α this Parareal variant converges as fast as the original Parareal algorithm. However, due to the roundoff error stemming from the diagonalization of C_α (as discussed in Section 3.5.2), an arbitrarily small α is impractical, particularly when the working precision is low, e.g. single or half precision. Fortunately it is not necessary to use an extremely small α for the diagonalization-based CGC to achieve the same convergence rate as the standard CGC.

Theorem 4.7 (Wu 2018). Let ρ denote the convergence factor of standard Parareal (4.14), and ρ_{new} the convergence factor of the new Parareal variant (4.15), where the coarse solver $\mathcal{G}$ is a stable time-integrator. Then we obtain

$$\rho_{\text{new}} = \rho, \quad \text{if } \alpha \leq \frac{\rho}{1+\rho}.$$

This result was proved for linear problems $\boldsymbol{u}' = A\boldsymbol{u} + g$, where A has negative real eigenvalues. For other scenarios, such as when A has complex eigenvalues, numerical results suggest its validity as well. Since the roundoff error resulting from the diagonalization procedure grows as α decreases, it is clear that the optimal choice for α is $\alpha = \rho/(1+\rho)$. In practice $\rho = O(10^{-1})$, and hence $\alpha = \rho/(1+\rho) = O(10^{-1})$ as well. The roundoff error incurred with a parameter $\alpha = O(10^{-1})$ is negligible.

To illustrate the convergence of the new Parareal variant (4.15), we consider the heat equation (2.3) and the advection–diffusion equation (ADE) (2.5) with periodic boundary conditions and an initial condition $u(x,0) = \sin(2\pi x)$ for $x \in (0,1)$. We use backward Euler as the coarse solver $\mathcal{G}$ and SDIRK22 from (4.9) for the fine solver $\mathcal{F}$. The data used here is $T = 4$, $J = 10$, $\Delta T = 0.1$ and $\Delta x = \frac{1}{128}$. In Figure 4.12 we present the measured error of Parareal using both the diagonalization-based and standard CGC. For the diagonalization-based CGC, we use three values of the parameter α to illustrate how the convergence rate depends on this parameter. For the heat equation, the convergence factor of Parareal with standard CGC is $\rho \approx 0.22$, and thus, according to Theorem 4.7, the threshold for α such that the diagonalization-based CGC achieves the same convergence rate is $\rho/(1+\rho) \approx 0.18$. If α exceeds this threshold, the diagonalization-based CGC results in a slower convergence rate. Thus the theoretical analysis accurately predicts the numerical results shown in Figure 4.12(a). For ADE with $\nu = 0.1$, $\rho \approx 0.39$ and the threshold for α is $\rho/(1+\rho) \approx 0.28$. Hence, as seen in Figure 4.12(b), $\alpha = 0.25$ suffices to let the diagonalization-based Parareal converge as fast as the standard Parareal.

We next address how to adapt the diagonalization-based CGC to nonlinear problems of the form $\boldsymbol{u}' = f(\boldsymbol{u})$ with an initial value $\boldsymbol{u}(0) = \boldsymbol{u}_0$. We continue to

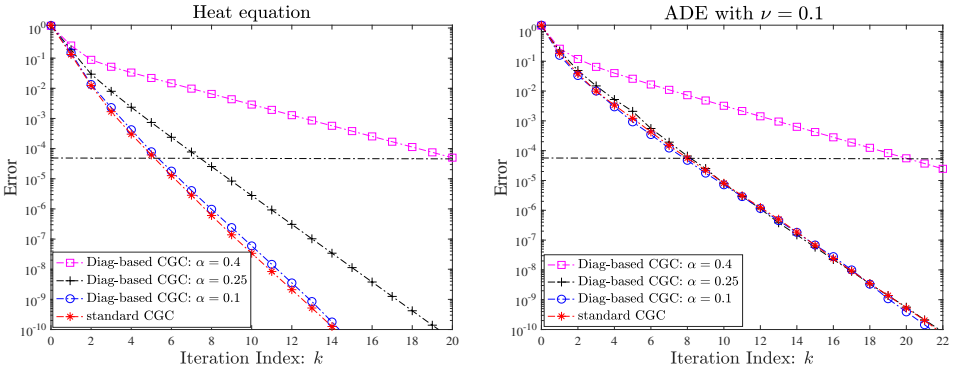

(a) (b)

Figure 4.12. Measured error of Parareal using the diagonalization-based CGC (see (4.15)) and the standard CGC (i.e. $\alpha = 0$ in (4.14)).

use backward Euler for the coarse solver $\mathcal{G}$. Then, with

$$\boldsymbol{b}_{n+1}^k := \mathcal{F}(T_n, T_{n+1}, \tilde{\boldsymbol{u}}_n^k) - \mathcal{G}(T_n, T_{n+1}, \boldsymbol{u}_n^k),$$

the initial part of the CGC algorithm (4.15), that is,

$$\boldsymbol{u}_{n+1}^{k+1} = \mathcal{G}\left(T_n, T_{n+1}, \boldsymbol{u}_n^{k+1}\right) + \boldsymbol{b}_{n+1}^k,$$

can be reformulated as

$$\frac{\boldsymbol{u}_{n+1}^{k+1} - \boldsymbol{b}_{n+1}^k - \boldsymbol{u}_n^{k+1}}{\Delta T} = f\left(\boldsymbol{u}_{n+1}^{k+1} - \boldsymbol{b}_{n+1}^k\right), \quad n = 0, 1, \ldots, N_t - 1.$$

This, together with the head–tail coupling condition $\boldsymbol{u}_0^{k+1} = \alpha \boldsymbol{u}_{N_t}^{k+1} + \boldsymbol{u}_0$, leads to the nonlinear all-at-once system

$$(C_\alpha \otimes I_x)\boldsymbol{U}^{k+1} - \Delta T F(\boldsymbol{U}^{k+1}) = \boldsymbol{g}^k, \tag{4.18}$$

where the definitions for $\boldsymbol{U}^{k+1}$ and C_α remain the same as in (4.16), and

$$F(\boldsymbol{U}^{k+1}) := \begin{bmatrix} f\left(\boldsymbol{u}_1^{k+1} - \boldsymbol{b}_1^k\right) \\ f\left(\boldsymbol{u}_2^{k+1} - \boldsymbol{b}_2^k\right) \\ \vdots \\ f\left(\boldsymbol{u}_{N_t}^{k+1} - \boldsymbol{b}_{N_t}^k\right) \end{bmatrix}, \quad \boldsymbol{g}^k := \begin{bmatrix} \boldsymbol{b}_1^k + \boldsymbol{u}_0 \\ \boldsymbol{b}_2^k \\ \vdots \\ \boldsymbol{b}_{N_t}^k \end{bmatrix}.$$

We solve the nonlinear system (4.18) by a quasi-Newton method as previously for the nonlinear ParaDiag method (see Section 3.5.1),

$$\begin{aligned} \mathcal{P}_\alpha^{k+1,l} \Delta \boldsymbol{U}^{k+1,l} &= \boldsymbol{g}^k - (C_\alpha \otimes I_x)\boldsymbol{U}^{k+1,l} + \Delta T F(\boldsymbol{U}^{k+1,l}), \\ \boldsymbol{U}^{k+1,l+1} &= \boldsymbol{U}^{k+1,l} + \Delta \boldsymbol{U}^{k+1,l}, \end{aligned} \tag{4.19a}$$

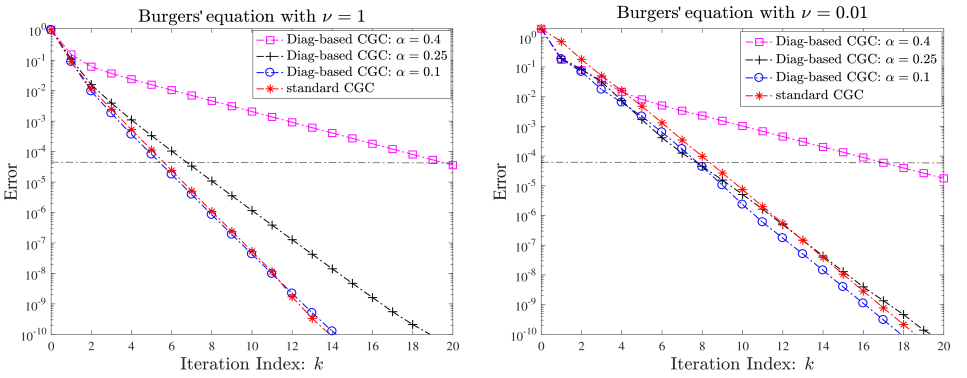

Figure 4.13. Measured error of Parareal using the two CGCs for Burgers' equation with two values of the diffusion parameter ν.

where $l = 0, 1, \ldots, l_{\max}$ denotes the Newton iteration index. The matrix $\mathcal{P}_\alpha^{k+1,l}$ is a block α-circulant matrix given by

$$\mathcal{P}_\alpha^{k+1,l} := C_\alpha \otimes I_x - I_t \otimes \Delta T A^{k+1,l}, \tag{4.19b}$$

where $A^{k+1,l}$ is the average of the Jacobi matrices,

$$A^{k+1,l} := \frac{1}{J} \sum_{j=1}^{J} \nabla f\left(\boldsymbol{u}_n^{k+1,l} - \boldsymbol{b}_n^k\right).$$

The Kronecker tensor product $I_t \otimes A^{k+1,l}$ serves as an approximation of the Jacobi matrix $\nabla F(\boldsymbol{U}^{k+1,l})$. We note that the nearest Kronecker product approximation (NKA), introduced in Section 3.5.1, could also be used to obtain a better approximation of $\nabla F(\boldsymbol{U}^{k+1,l})$, but for simplicity we will not explore this option further.

The matrix $\mathcal{P}_\alpha^{k+1,l}$ has the same structure as the coefficient matrix in (4.16), which allows us to solve for the increment $\Delta \boldsymbol{U}^{k+1,l}$ using the diagonalization procedure outlined in (4.17). The convergence analysis of the new Parareal variant (4.15) in the nonlinear context is detailed in Wu (2018, Section 4), where it is shown that the convergence rate mirrors that of Parareal with standard CGC when α is chosen appropriately small. We illustrate this by applying Parareal with both CGCs to Burgers' equation (2.6), using the same problem set-up and discretization parameters as in the previously discussed heat and advection–diffusion equation case. In Figure 4.13 we present the measured errors for two values of the diffusion parameter ν. We see that for this nonlinear problem too, the influence of α on the convergence rate remains as in the linear case.

Remark 4.2 (Extension to MGRiT). The fundamental mechanism of MGRiT (4.12) aligns with that of Parareal, and specifically, the CGC can be similarly represented as in (4.14). However, a direct extension of the diagonalization-based CGC devised for Parareal in (4.15) to MGRiT leads to divergence regardless of

the choice of α. This is because the head–tail-type coupling condition $\boldsymbol{u}_1^{k+1} = \alpha \boldsymbol{u}_{N_t}^{k+1} + \boldsymbol{u}_1$ used is less natural than the one from Gander and Wu (2019) that appeared a year later, namely

$$\boldsymbol{u}_1^{k+1} = \alpha\big(\boldsymbol{u}_{N_t}^{k+1} - \boldsymbol{u}_{N_t}^{k}\big) + \boldsymbol{u}_1.$$

Using this more natural head–tail condition, which is consistent at convergence for MGRiT, was proposed in Wu and Zhou (2019), leading to the convergent MGRiT variant

$$\begin{aligned} &\boldsymbol{u}_0^{k+1} = \boldsymbol{u}_0,\ \boldsymbol{u}_1^{k+1} = \alpha\big(\boldsymbol{u}_{N_t}^{k+1} - \boldsymbol{u}_{N_t}^{k}\big) + \boldsymbol{u}_1, \\ &\boldsymbol{u}_{n+1}^{k+1} = \mathcal{G}\big(T_n, T_{n+1}, \boldsymbol{u}_n^{k+1}\big) + \tilde{\boldsymbol{b}}_{n+1}^{k},\ n = 1, 2, \ldots, N_t - 1, \end{aligned} \tag{4.20}$$

where

$$\tilde{\boldsymbol{b}}_{n+1}^{k} = \mathcal{F}\big(T_n, T_{n+1}, \tilde{\boldsymbol{s}}_n^{k}\big) - \mathcal{G}\big(T_n, T_{n+1}, \tilde{\boldsymbol{s}}_n^{k}\big), \quad \tilde{s}_n^{k} := \mathcal{F}\big(T_{n-1}, T_n, \tilde{\boldsymbol{u}}_{n-1}^{k}\big)$$

and

$$\tilde{\boldsymbol{u}}_n^{k} = \begin{cases} \boldsymbol{u}_n, & n = 0, 1, \\ \boldsymbol{u}_n^{k}, & n \geq 2. \end{cases}$$

This variant converges at the same rate as the original MGRiT method (4.12), provided α is suitably small; Theorem 4.7 applies to MGRiT in an analogous manner. For Parareal, we can also use the more natural head–tail condition $\boldsymbol{u}_0^{k+1} = \alpha(\boldsymbol{u}_{N_t}^{k+1} - \boldsymbol{u}_{N_t}^{k}) + \boldsymbol{u}_0$, which is consistent at convergence, instead of (4.15), and we obtain the same convergence rate as shown in Theorem 4.7 for the less natural condition.

4.5.2. Diagonalization-based coarse solver

A fundamentally distinct idea from the ParaDiag CGC method in Section 4.5.1 that combines ParaDiag with Parareal was introduced in Gander and Wu (2020). The key innovation lies in using the same time-integrator and time-step size for both the coarse and fine solvers, but implementing the coarse solver through a diagonalization procedure. This approach can work for hyperbolic problems too, since it also transports all frequency components in the coarse propagator over a very long time.

We illustrate this concept for the nonlinear system of ODEs $\boldsymbol{u}' = f(\boldsymbol{u})$ with initial value $\boldsymbol{u}(0) = \boldsymbol{u}_0$. For the time discretization, we use the linear-θ method; a generalization to the s-stage Runge–Kutta method can be found in the appendix of Gander and Wu (2020). On each large time interval $[T_n, T_{n+1}]$, the fine solver $\mathcal{F}(T_n, T_{n+1}, \boldsymbol{u}_n)$ computes the solution at $t = T_{n+1}$ by performing J steps of the linear-θ method sequentially, i.e. $\mathcal{F}(T_n, T_{n+1}, \boldsymbol{u}_n) = \boldsymbol{v}_J$, with $\boldsymbol{v}_J$ being the final solution of

$$\boldsymbol{v}_{j+1} - \boldsymbol{v}_j = \Delta t[\theta f(\boldsymbol{v}_{j+1}) + (1-\theta) f(\boldsymbol{v}_j)], \quad j = 0, 1, \ldots, J-1, \tag{4.21}$$

with initial condition $\boldsymbol{v}_0 = \boldsymbol{u}_n$, where

$$\Delta t = \frac{\Delta T}{J} = \frac{T_{n+1} - T_n}{J}$$

and $\theta = 1$ or $\theta = \frac{1}{2}$. For the coarse solver, denoted by $\mathcal{F}^*_\alpha(T_n, T_{n+1}, \boldsymbol{u}_n)$, we solve the nonlinear system with a head–tail coupled condition,

$$\begin{aligned} &\boldsymbol{v}_{j+1} - \boldsymbol{v}_j = \Delta t[\theta f(\boldsymbol{v}_{j+1}) + (1-\theta) f(\boldsymbol{v}_j)], \quad j = 0, 1, \ldots, J-1, \\ &\boldsymbol{v}_0 = \alpha \boldsymbol{v}_J + (1-\alpha)\boldsymbol{u}_n. \end{aligned} \tag{4.22}$$

This system can be recast as the nonlinear all-at-once system

$$\underbrace{(C_\alpha \otimes I_x)\boldsymbol{V} - \Delta t F(\boldsymbol{V})}_{:=\mathcal{K}(\boldsymbol{V})} = \boldsymbol{b}(\boldsymbol{u}_n), \tag{4.23}$$

where

$$\boldsymbol{V} := (\boldsymbol{v}_1^\top, \boldsymbol{v}_2^\top, \ldots, \boldsymbol{v}_J^\top)^\top, \quad \boldsymbol{b}(\boldsymbol{u}_n) := ((1-\alpha)\boldsymbol{u}_n^\top, 0, \ldots, 0)^\top,$$

and

$$\begin{aligned} C_\alpha &:= \begin{bmatrix} 1 & & & -\alpha \\ -1 & 1 & & \\ & \ddots & \ddots & \\ & & -1 & 1 \end{bmatrix}, \\ F(\boldsymbol{V}) &:= \begin{bmatrix} \theta f(\boldsymbol{v}_1) + (1-\theta) f(\alpha \boldsymbol{v}_J + (1-\alpha)\boldsymbol{u}_n) \\ \theta f(\boldsymbol{v}_2) + (1-\theta) f(\boldsymbol{v}_1) \\ \vdots \\ \theta f(\boldsymbol{v}_J) + (1-\theta) f(\boldsymbol{v}_{J-1}) \end{bmatrix}. \end{aligned} \tag{4.24}$$

We solve (4.23) with the quasi-Newton method

$$\mathcal{P}_\alpha(\boldsymbol{V}^l)\Delta \boldsymbol{V}^l = \boldsymbol{b}(\boldsymbol{u}_n) - \mathcal{K}(\boldsymbol{V}^l), \quad \boldsymbol{V}^{l+1} = \boldsymbol{V}^l + \Delta \boldsymbol{V}^l, \tag{4.25a}$$

where $l = 0, 1, \ldots, l_{\max}$, and the matrix $\mathcal{P}_\alpha(\boldsymbol{V}^l)$ is a block α-circulant matrix serving as an approximation to the Jacobi matrix

$$\nabla \mathcal{K}(\boldsymbol{V}^l) = C_\alpha \otimes I_x - \Delta t(\tilde{C}_{\theta,\alpha} \otimes I_x)\nabla F(\boldsymbol{V}^l).$$

It is defined by

$$\mathcal{P}_\alpha(\boldsymbol{V}^l) = C_\alpha \otimes I_x - \Delta t \tilde{C}_{\alpha,\theta} \otimes \overline{\nabla \mathbf{f}}(\boldsymbol{V}^l), \tag{4.25b}$$

where $\tilde{C}_{\alpha,\theta}$ is an α-circulant matrix given by

$$\tilde{C}_{\theta,\alpha} := \begin{bmatrix} \theta & & & (1-\theta)\alpha \\ 1-\theta & \theta & & \\ & \ddots & \ddots & \\ & & 1-\theta & \theta \end{bmatrix},$$

and $\overline{\nabla f}(\boldsymbol{V}^l)$ represents the average of the J Jacobi blocks of $\nabla F(\boldsymbol{V}^l)$,

$$\overline{\nabla f}(\boldsymbol{V}^l) := \frac{1}{J}\left[\sum_{j=1}^{J-1} \nabla f\left(\boldsymbol{v}_j^l\right) + \nabla f\left(\alpha \boldsymbol{v}_J^l + (1-\alpha)\boldsymbol{u}_n\right)\right].$$

Using this notation, we can write the Parareal algorithm from Gander and Wu (2020) as

$$\boldsymbol{u}_{n+1}^{k+1} = \mathcal{F}_\alpha^*\left(T_n, T_{n+1}, \boldsymbol{u}_n^{k+1}\right) + \mathcal{F}\left(T_n, T_{n+1}, \boldsymbol{u}_n^k\right) - \mathcal{F}_\alpha^*\left(T_n, T_{n+1}, \boldsymbol{u}_n^k\right), \tag{4.26}$$

where $n = 0, 1, \ldots, N_t - 1$ denotes the time-step index.

For linear problems, i.e. $f(\boldsymbol{u}) = A\boldsymbol{u}$, the all-at-once system (4.23) becomes

$$(C_\alpha \otimes I_x - \tilde{C}_{\theta,\alpha} \otimes \Delta t A)\boldsymbol{V} = \boldsymbol{b}(\boldsymbol{u}_n), \tag{4.27}$$

with

$$\boldsymbol{b}(\boldsymbol{u}_n) = ([(I_x + \Delta t(1-\theta)A)(1-\alpha)\boldsymbol{u}_n]^\top, 0, \ldots, 0)^\top.$$

The coarse solver $\mathcal{F}_\alpha^*(T_n, T_{n+1}, \boldsymbol{u}_n^k)$ is defined by

$$\mathcal{F}_\alpha^*(T_n, T_{n+1}, \boldsymbol{u}_n^k) := (H_J \otimes I_x)\boldsymbol{V},$$

where $H_J := (0, \ldots, 0, 1) \in \mathbb{R}^{1\times J}$. With $\boldsymbol{V} = (\boldsymbol{v}_1^\top, \boldsymbol{v}_2^\top, \ldots, \boldsymbol{v}_J^\top)^\top$, we have $\mathcal{F}_\alpha^*(T_n, T_{n+1}, \boldsymbol{u}_n^k) = \boldsymbol{v}_J$, and the computation of $\boldsymbol{V}$ in (4.27) is equivalent to solving the all-at-once system

$$\begin{aligned} &\boldsymbol{v}_{j+1} - \boldsymbol{v}_j = \Delta t A[\theta \boldsymbol{v}_{j+1} + (1-\theta)\boldsymbol{v}_j], \quad j = 0, 1, \ldots, J-1, \\ &\boldsymbol{v}_0 = \alpha \boldsymbol{v}_J + (1-\alpha)\boldsymbol{u}_n^k. \end{aligned} \tag{4.28}$$

It is clear that the coarse solver reduces to the fine solver if $\alpha = 0$, and in this limit Parareal (4.26) converges in only one iteration, but without any speed-up because we have to solve (4.28) for $\mathcal{F}_\alpha^*(T_n, T_{n+1}, \boldsymbol{u}_n^k) = \boldsymbol{v}_J$ sequentially. For $\alpha \in (0, 1)$, we solve (4.28) in one shot by diagonalization, which is parallel for the J fine time points, and thus the computation time is approximately J times less than the fine solver $\mathcal{F}(T_n, T_{n+1}, \boldsymbol{u}_n^k)$. This Parareal variant has different convergence rates for parabolic and hyperbolic problems.

Theorem 4.8 (Gander and Wu 2020). For linear initial value problems $\boldsymbol{u}' = A\boldsymbol{u} + g$ with $\boldsymbol{u}(0) = \boldsymbol{u}_0$ and $A \in \mathbb{C}^{N_x \times N_x}$, let $\{\boldsymbol{u}_n^k\}$ be the kth iterate of the Parareal variant (4.26) and let $\{\boldsymbol{u}_n\}$ be the converged solution. Then, for any stable one-step Runge–Kutta method used for $\mathcal{F}$ and $\mathcal{F}_\alpha^*$, the global error

$$\boldsymbol{e}^k = \max_{n=1,2,\ldots,N_t} \|\boldsymbol{u}_n - \boldsymbol{u}_n^k\|_\infty$$

satisfies the estimate

$$\boldsymbol{e}^k \le \rho^k \boldsymbol{e}^0,$$

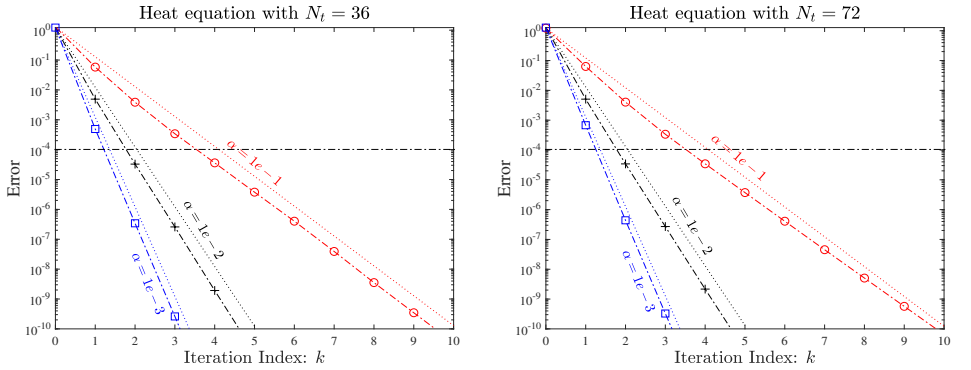

Figure 4.14. Error of the Parareal variant (4.26) for the heat equation. The dotted lines denote the error predicted by the theoretical convergence factor $\rho = \alpha$.

where the convergence factor ρ is given by

$$\rho = \begin{cases} \alpha, & \text{if } \sigma(A) \subset \mathbb{R}^-, \\ \dfrac{2\alpha N_t}{1+\alpha}, & \text{if } \sigma(A) \subset \mathrm{i}\mathbb{R}. \end{cases} \tag{4.29}$$

Here $\sigma(A)$ denotes the spectrum of A. When the matrix A arises from semi-discretizing the heat equation, i.e. $A \approx \Delta$, we have $\sigma(A) \subset \mathbb{R}^-$. In this case the convergence factor $\rho = \alpha$ implies that the Parareal variant (4.26) converges with a rate independent of N_t. For wave propagation problems, e.g. the second-order wave equation (2.7) and the Schrödinger equation, all the eigenvalues of the discrete matrix A are imaginary, i.e. $\sigma(A) \subset \mathrm{i}\mathbb{R}$. For this kind of problem, the convergence factor increases linearly in N_t. However, this does not necessarily imply that the convergence rate deteriorates, especially when α is relatively small and N_t is not too large.

We now illustrate the convergence of the Parareal variant (4.26) for the heat equation (2.3) with homogeneous Dirichlet boundary conditions and initial condition $u(x,0) = \sin^2(2\pi x)$ with $x \in (0,1)$. For both $\mathcal{F}$ and $\mathcal{F}_\alpha^*$, we use the trapezoidal rule and the discretization parameters $\Delta T = \frac{1}{12}$, $J = 10$, $\Delta x = \frac{1}{100}$. For two values of N_t and three parameters α, Figure 4.14 shows the measured error, where the error predicted by the convergence factor $\rho = \alpha$ is plotted as dotted lines. We see that the theoretical convergence factor is sharp, and the convergence rate is indeed independent of N_t.

We next consider the wave equation (2.7) with periodic boundary conditions and initial conditions $u(x,0) = \sin^2(2\pi x)$ and $\partial_t u(x,0) = 0$. After space discretization, the system of ODEs is given by

$$\boldsymbol{w}' = \boldsymbol{A}\boldsymbol{w}, \quad \boldsymbol{w}(0) = \begin{bmatrix} \sin^2(2\pi \boldsymbol{x}_h) \\ 0 \end{bmatrix}, \quad \boldsymbol{A} := \begin{bmatrix} & I_x \\ A & \end{bmatrix},$$

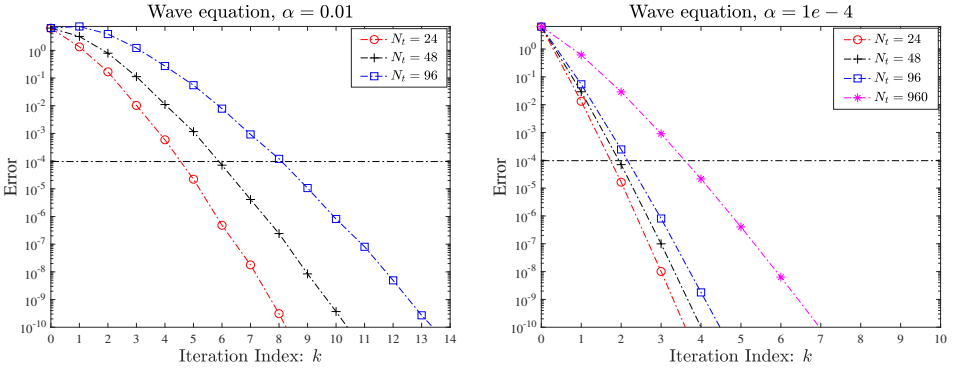

(a) (b)

Figure 4.15. Measured error of the Parareal variant (4.26) with two values of the parameter α for the wave equation.

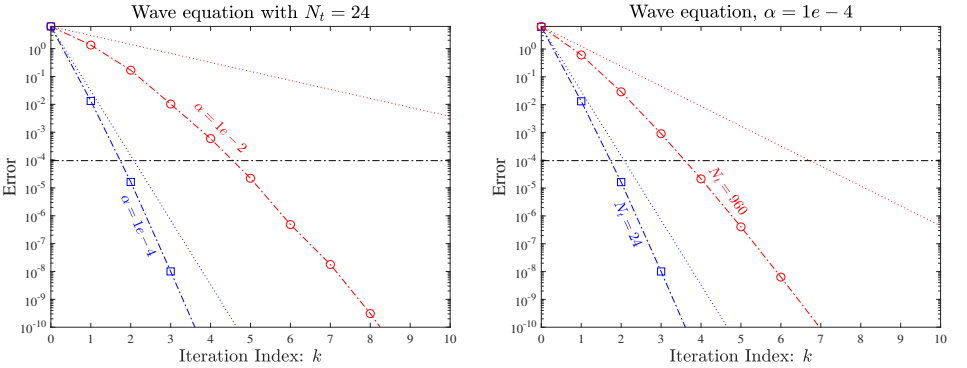

Figure 4.16. The convergence factor ρ (dotted line) for the wave equation gives quite a sharp bound on the measured error for small αN_t, while for large αN_t the bound is not sharp.

where $\boldsymbol{w} = (\boldsymbol{u}^\top, (\boldsymbol{u}')^\top)^\top$ and $A \approx \Delta$. All the eigenvalues of $\boldsymbol{A}$ are purely imaginary, and thus according to (4.29) the convergence rate of the Parareal variant (4.26) deteriorates as N_t grows. For relatively large α, e.g. $\alpha = 0.01$, this is indeed the case, as shown in Figure 4.15(a). However, for small α, the influence of N_t on the convergence rate becomes insignificant, as shown in Figure 4.15(b). For example, as N_t increases from 24 to 960, we only require an additional two iterations to reach the stopping tolerance, denoted by the horizontal line, i.e. the order of the discretization error $\max\{\Delta t^2, \Delta x^2\}$.

In contrast to the heat equation, for wave equations the convergence factor given in (4.29) is not always sharp, depending on the product αN_t. This is illustrated in Figure 4.16, where we consider three groups of (α, N_t). For a small product,

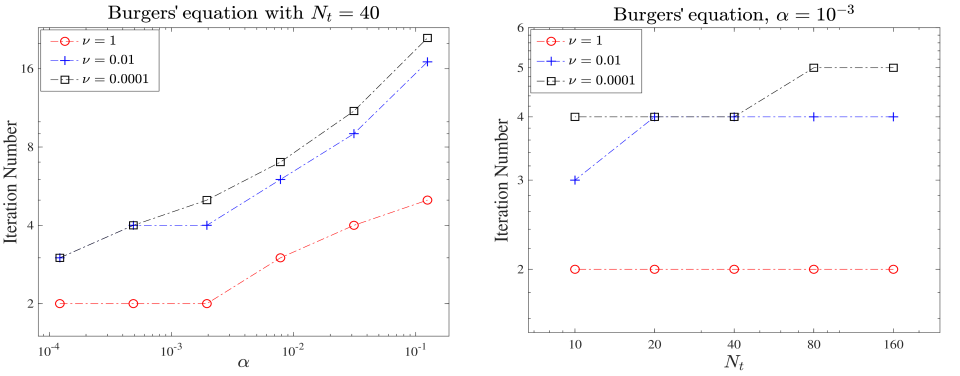

(a) (b)

Figure 4.17. Iteration numbers of the parareal variant (4.26) for Burgers' equation when the global error reaches 10^{-8}, with three values of the diffusion parameter ν.

i.e. $\alpha = 10^{-4}$ and $N_t = 24$, the convergence factor quite accurately predicts the measured error. For the other two values of (α, N_t), the linear bound is not sharp, and we observe superlinear convergence of the method.

For nonlinear problems, $\boldsymbol{u}' = f(\boldsymbol{u})$, the convergence analysis of the Parareal variant (4.26) can be found in Gander and Wu (2020, Section 4), under the assumption that the solution of the nonlinear all-at-once system (4.23) is solved exactly and that the nonlinear function f satisfies some Lipschitz condition. The main conclusion is that the method converges with a rate $\rho = O(\alpha)$ when α is small, which is similar to the result for the linear case. We illustrate this for Burgers' equation (2.6) with periodic boundary conditions and initial condition $u(x, 0) = \sin^2(2\pi x)$ for $x \in (0, 1)$. Let $\Delta T = 0.1$, $J = 10$ and $\Delta x = \frac{1}{100}$. Then, by fixing $N_t = 40$, in Figure 4.17(a) we show the iteration number for several values of α when the global error reaches 10^{-8}. Clearly a smaller α accelerates convergence. Concerning the influence of ν, it seems that for small α it has only a minor influence on the convergence rate, but for large α the convergence rate deteriorates when ν decreases. In Figure 4.17(b) we show the iteration numbers when $\alpha = 10^{-3}$ and N_t varies from 10 to 160, which indicates that the convergence rate is robust in terms of N_t.

The two Parareal variants (4.15) and (4.26) introduced in this section apply ParaDiag to standard Parareal in different ways. For the former, diagonalization is used for the N_t coarse time points, changing the CGC. For the second variant, diagonalization is used for each large time interval $[T_n, T_{n+1}]$ across the J fine time points, defining a special coarse solver while keeping the CGC as in the standard Parareal. These two variants have distinct scopes of application: the first, like the standard Parareal, works primarily for parabolic problems, while the second is effective for both parabolic and hyperbolic problems.

4.6. *Space–time multigrid (STMG)*

The final parallel method we wish to introduce is the space–time multigrid (STMG) method, which is based on using the multigrid (MG) method in both space and time. After early seminal contributions (Hackbusch 1984, Horton and Vandewalle 1995), it was recognized that block Jacobi smoothers in time are a crucial component (Gander and Neumüller 2016), leading to a method as effective as when MG is applied to Poisson problems, using only standard multigrid components in STMG. For the heat equation (2.3) or the advection–diffusion equation (2.5), the STMG method can be described as follows: using a spatial discretization with mesh size Δx results in a system of ODEs $\boldsymbol{u}' = A\boldsymbol{u} + \boldsymbol{f}$, to which we apply a one-step time-integrator,

$$r_1 \boldsymbol{u}_{n+1} = r_2 \boldsymbol{u}_n + \tilde{\boldsymbol{f}}_n, \quad n = 0, 1, \ldots, N_t - 1, \tag{4.30}$$

where $\boldsymbol{u}_0$ is the initial value, and r_1 and r_2 are matrix polynomials of $\Delta t A$ (see (3.57) for backward Euler and the trapezoidal rule). The matrix $A \in \mathbb{R}^{N_x \times N_x}$ is the discrete matrix of the Laplacian ∂_{xx} or the advection–diffusion operator $-\partial_x + \nu \partial_{xx}$ with mesh size Δx. As in ParaDiag described in Section 3.5, we collect the N_t difference equations in the all-at-once system

$$\underbrace{\begin{bmatrix} r_1 & & & \\ -r_2 & r_1 & & \\ & \ddots & \ddots & \\ & & -r_2 & r_1 \end{bmatrix}}_{:=\mathcal{K}} \underbrace{\begin{bmatrix} \boldsymbol{u}_1 \\ \boldsymbol{u}_2 \\ \vdots \\ \boldsymbol{u}_{N_t} \end{bmatrix}}_{:=\boldsymbol{U}} = \boldsymbol{b}, \tag{4.31}$$

where $\boldsymbol{b}$ is a suitable right-hand side vector.

STMG solves for $\boldsymbol{U}$ within a multigrid framework, using a damped block Jacobi iteration as smoother. Starting from an initial approximation $\boldsymbol{U}^{\text{ini}}$ of $\boldsymbol{U}$, the smoother $\mathcal{S}$ produces a new approximation $\boldsymbol{U}^{\text{new}}$ by computing

$$\boldsymbol{U}^{\text{new}} = \mathcal{S}_\eta(\boldsymbol{b}, \boldsymbol{U}^{\text{ini}}, s): \begin{cases} \boldsymbol{U}^0 = \boldsymbol{U}^{\text{ini}}, \\ \text{for } j = 0, 1, \ldots, s-1: \\ \quad (I_t \otimes r_1)\Delta \boldsymbol{U}^j = \eta(\boldsymbol{b} - \mathcal{K}\boldsymbol{U}^j), \\ \quad \boldsymbol{U}^{j+1} = \boldsymbol{U}^j + \Delta \boldsymbol{U}^j, \\ \boldsymbol{U}^{\text{new}} = \boldsymbol{U}^s, \end{cases} \tag{4.32}$$

where s is the number of smoothing iterations and η is the damping parameter. Since $I_t \otimes r_1$ is a block diagonal matrix, for each smoothing step the N_t subvectors of $\Delta \boldsymbol{U}^j$ can be solved in parallel, making this a parallel-in-time smoother. We also need restriction and prolongation operators in space and time. For illustration, we

show these two operators in space with $N_x = 7$,

$$P_x := \begin{bmatrix} \frac{1}{2} & & \\ 1 & & \\ \frac{1}{2} & \frac{1}{2} & \\ & 1 & \\ & \frac{1}{2} & \frac{1}{2} \\ & & 1 \\ & & \frac{1}{2} \end{bmatrix} \in \mathbb{R}^{7\times 3}, \quad R_x = \frac{1}{2}P_x^\top \in \mathbb{R}^{3\times 7}. \tag{4.33}$$

Similar notations apply to the other two operators P_t and R_t for the time variable. We can now define the two-level variant of STMG from iteration k to $k+1$ as

$$\begin{cases} \boldsymbol{U}^{k+1/3} = \mathcal{S}_\eta(\boldsymbol{b}, \boldsymbol{U}^k, s_1), \\ \boldsymbol{r} = \boldsymbol{b} - \mathcal{K}\boldsymbol{U}^{k+1/3}, \quad \boldsymbol{r}_c = [R_x \mathrm{Mat}(\boldsymbol{r})]R_t^\top, \\ \boldsymbol{e}_c = \mathcal{K}_c^{-1}\mathrm{Vec}(\boldsymbol{r}_c), \quad \boldsymbol{e} = [P_x \mathrm{Mat}(\boldsymbol{e}_c)]P_t^\top, \\ \boldsymbol{U}^{k+2/3} = \boldsymbol{U}^{k+1/3} + \mathrm{Vec}(\boldsymbol{e}), \\ \boldsymbol{U}^{k+1} = \mathcal{S}_\eta(\boldsymbol{b}, \boldsymbol{U}^{k+2/3}, s_2), \end{cases} \tag{4.34}$$

where 'Vec' denotes the vectorization operation from a matrix, and 'Mat' denotes the reverse operation, converting a vector to the corresponding matrix. In practice we use the `reshape` command in MATLAB. The matrix $\mathcal{K}_c$ is the all-at-once matrix obtained with larger space and time discretization parameters $\Delta T = 2\Delta t$ and $\Delta X = 2\Delta x$, that is,

$$\mathcal{K}_c = \underbrace{\begin{bmatrix} r_1^c & & & \\ -r_2^c & r_1^c & & \\ & \ddots & \ddots & \\ & & -r_2^c & r_1^c \end{bmatrix}}_{N_t^c \text{ blocks}},$$

where r_1^c and r_2^c are matrix polynomials of $\Delta T A_c$, with $A_c \in \mathbb{R}^{N_x^c \times N_x^c}$ being the *coarse* discrete matrix of the space derivative(s) with ΔX, for example,

$$\begin{cases} r_1^c = I_x^c - \Delta T A_c, \ r_2^c = I_x^c, & \text{backward Euler,} \\ r_1^c = I_x^c - \frac{1}{2}\Delta T A_c, \ r_2^c = I_x^c + \frac{1}{2}\Delta T A_c, & \text{trapezoidal rule.} \end{cases}$$

In practice we let $N_x = 2^{l_x} - 1$ and $N_t = 2^{l_t} - 1$, with $l_x, l_t \geq 2$ being integers, and thus $N_x^c = 2^{l_x - 1} - 1$ and $N_t^c = 2^{l_t - 1} - 1$. STMG is obtained naturally by applying the two-level variant recursively.

There is an important difference between STMG and the parabolic MG method proposed 40 years ago (Hackbusch 1984): for parabolic MG, we use a *pointwise*

Gauss–Seidel iteration as smoother, defined by

$$\boldsymbol{U}^{\text{new}} = \mathcal{S}_{\text{GS}}(\boldsymbol{b}, \boldsymbol{U}^{\text{ini}}, s): \begin{cases} \text{for } n = 0, 1, \ldots, N_t - 1 \\ \quad \boldsymbol{u}_{n+1}^0 = \boldsymbol{u}_{n+1}^{\text{ini}}, \\ \quad \text{for } j = 0, 1, \ldots, s - 1 \\ \quad\quad (D + L)\Delta \boldsymbol{u}_{n+1}^j = \tilde{\boldsymbol{f}}_n + r_2 \boldsymbol{u}_n^s - r_1 \boldsymbol{u}_{n+1}^j, \\ \quad\quad \boldsymbol{u}_{n+1}^{j+1} = \boldsymbol{u}_{n+1}^j + \Delta \boldsymbol{u}_{n+1}^j, \\ \quad \boldsymbol{u}_{n+1}^{\text{new}} = \boldsymbol{u}_{n+1}^s, \end{cases} \tag{4.35}$$

where $\boldsymbol{u}_0^s = \boldsymbol{u}_0$ and D and L represent the diagonal and upper triangular parts of r_1. Here $\boldsymbol{U}^{\text{ini}} := (\boldsymbol{u}_0^\top, (\boldsymbol{u}_1^{\text{ini}})^\top, \ldots, (\boldsymbol{u}_{N_t}^{\text{ini}})^\top)^\top$, and similarly $\boldsymbol{U}^{\text{new}}$ consists of the vectors $\boldsymbol{u}_0$ and $\boldsymbol{u}_1^{\text{new}}, \ldots, \boldsymbol{u}_{N_t}^{\text{new}}$. This smoother operates sequentially in time: we must complete the smoothing iteration at time-step n to obtain $\boldsymbol{u}_n^s$, which is necessary for performing the smoothing iteration at time-step $n + 1$. After smoothing, we restrict the residual $\boldsymbol{b} - \mathcal{K}\boldsymbol{U}^{\text{new}}$ in space–time, as in standard multigrid, to a coarser grid. There, we solve a coarse problem (and repeat this procedure recursively in practice). Hackbusch (1984) focused on coarsening in space for this method, and found that for the heat equation, parabolic MG converges very rapidly. Gander and Lunet (2024) examined the performance of a two-level version of the parabolic MG method that coarsens in both space and time, and found that it converges only slowly. Horton and Vandewalle (1995) improved upon this slow convergence by using special multigrid components adapted to the interpretation of the time direction as a strongly advective term; see also Janssen and Vandewalle (1996) and Van Lent and Vandewalle (2002) for multigrid waveform relaxation variants.

Returning to STMG (4.34), the smoother plays a crucial role in achieving good performance. The fundamental concept in designing an effective smoother is to eliminate as much of the high-frequency error components as possible within a minimal number of smoothing iterations. This allows the remaining low-frequency errors to be well-represented on the coarse grids and to be removed via coarse grid correction. A valuable tool for accomplishing this objective is *local Fourier analysis* (LFA), which involves neglecting the initial and boundary conditions of the problem and just focusing on how the finite difference stencil affects a given Fourier mode in the error,

$$u_{n,m}^j = C_{\omega,\xi}^j \mathrm{e}^{\mathrm{i}\omega n \Delta t} \mathrm{e}^{\mathrm{i}\xi m \Delta x}, \tag{4.36}$$

where $\boldsymbol{u}_n^j := (u_{n,1}^j, \ldots, u_{n,N_x}^j)^\top$ and $\mathrm{i} = \sqrt{-1}$. To apply LFA for the damped Jacobi iteration (4.32), we consider the one-dimensional heat equation (2.3) discretized using centred finite differences in space and backward Euler in time. In this case,

$$A = \frac{1}{\Delta x^2} \operatorname{Tri}(1, -2, 1), \quad r_1 = I_x - \Delta t A, \quad r_2 = I_x.$$

For each iteration j, the block Jacobi iteration (4.32) consists of the N_t difference equations

$$r_1\left(\boldsymbol{u}_{n+1}^{j+1}-\boldsymbol{u}_{n+1}^{j}\right)=-\eta\left(r_1\boldsymbol{u}_{n+1}^{j}-r_2\boldsymbol{u}_{n}^{j}\right), \tag{4.37}$$

where we set the right-hand side $\boldsymbol{b}$ in (4.32) to zero and consider $\boldsymbol{U}^j$ as the error at the jth iteration.

To apply LFA to (4.37), we first consider the result when the space discrete operator A acts on the Fourier mode $u_{n+1,m}^{l}$ (with $l=j,j+1$),

$$\begin{aligned} Au_{n+1,m}^{l} &= C_{\omega,\xi}^{l}\mathrm{e}^{\mathrm{i}\omega(n+1)\Delta t}\frac{\mathrm{e}^{\mathrm{i}\xi(m-1)\Delta x}-2\mathrm{e}^{\mathrm{i}\xi m\Delta x}+\mathrm{e}^{\mathrm{i}\xi(m+1)\Delta x}}{\Delta x^2} \\ &= C_{\omega,\xi}^{l}\mathrm{e}^{\mathrm{i}\omega(n+1)\Delta t}\mathrm{e}^{\mathrm{i}\xi m\Delta x}\frac{\mathrm{e}^{-\mathrm{i}\xi\Delta x}-2+\mathrm{e}^{\mathrm{i}\xi\Delta x}}{\Delta x^2} \\ &= \frac{2(\cos(\xi\Delta x)-1)}{\Delta x^2}C_{\omega,\xi}^{l}\mathrm{e}^{\mathrm{i}\omega(n+1)\Delta t}\mathrm{e}^{\mathrm{i}\xi m\Delta x}. \end{aligned} \tag{4.38}$$

Hence

$$r_1\left(\boldsymbol{u}_{n+1}^{j+1}-\boldsymbol{u}_{n+1}^{j}\right)=\left(1-\frac{2\Delta t(\cos(\xi\Delta x)-1)}{\Delta x^2}\right)\left(C_{\omega,\xi}^{j+1}-C_{\omega,\xi}^{j}\right)\mathrm{e}^{\mathrm{i}\omega(n+1)\Delta t}\mathrm{e}^{\mathrm{i}\xi\boldsymbol{x}_h},$$

and

$$\begin{aligned} r_1\boldsymbol{u}_{n+1}^{j}-r_2\boldsymbol{u}_{n}^{j} &= \boldsymbol{u}_{n+1}^{j}-\boldsymbol{u}_{n}^{j}-\Delta tA\boldsymbol{u}_{n+1}^{j} \\ &= \left(1-\mathrm{e}^{-\mathrm{i}\omega\Delta t}-\frac{2\Delta t(\cos(\xi\Delta x)-1)}{\Delta x^2}\right)C_{\omega,\xi}^{j}\mathrm{e}^{\mathrm{i}\omega(n+1)\Delta t}\mathrm{e}^{\mathrm{i}\xi\boldsymbol{x}_h}, \end{aligned}$$

where $\boldsymbol{x}_h=\mathrm{Vec}(m\Delta x)$. Now, from (4.37), we have

$$\begin{aligned} &\left(1-\frac{2\Delta t(\cos(\xi\Delta x)-1)}{\Delta x^2}\right)\left(C_{\omega,\xi}^{j+1}-C_{\omega,\xi}^{j}\right) \\ &\quad=\eta\left(1-\mathrm{e}^{-\mathrm{i}\omega\Delta t}-\frac{2\Delta t(\cos(\xi\Delta x)-1)}{\Delta x^2}\right)C_{\omega,\xi}^{j}, \end{aligned}$$

that is,

$$C_{\omega,\xi}^{j+1}=\rho(\omega,\xi,\eta)C_{\omega,\xi}^{j},$$

with ρ being the convergence factor given by

$$\rho(\omega,\xi,\eta)=1-\eta\left(1-\frac{\mathrm{e}^{-\mathrm{i}\omega\Delta t}}{1+\frac{2\Delta t}{\Delta x^2}(1-\cos(\xi\Delta x))}\right), \tag{4.39}$$

where $\omega\Delta t\in(-\pi,\pi)$ and $\xi\Delta x\in(-\pi,\pi)$. By calculating the maximum of ρ with respect to ξ and ω and then minimizing the maximum, the following result was proved in Gander and Lunet (2024, Chapter 4); see Gander and Neumüller (2016) for a comprehensive analysis for more general discretizations.

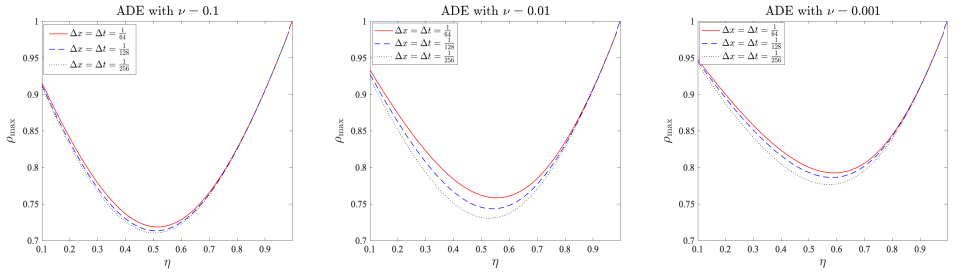

Figure 4.18. Maximum of the convergence factor over the high frequencies for the advection–diffusion equation (ADE) for three values of the diffusion parameter ν, i.e. $\rho_{\max} = \max_{(\Delta x\xi, \Delta t\omega)\in(-\pi,\pi)\times(\pi/2,\pi)} \rho(\omega, \xi, \eta)$.

Theorem 4.9. For the one-dimensional heat equation discretized with centred finite differences and backward Euler, the optimal choice of η used in the damped Jacobi smoother (4.32) always permitting time coarsening is $\eta = \frac{1}{2}$. With this choice, all high frequencies in time, $\omega \in \pm(\pi/(2\Delta t), \pi/\Delta t)$, are damped by a factor of at least $1/\sqrt{2}$. If in addition the mesh parameters satisfy $\Delta t/\Delta x^2 \geq 1/\sqrt{2}$, then the high frequencies in space, $\xi \in \pm(\pi/(2\Delta x), \pi/\Delta x)$, are also damped by a factor of at least $1/\sqrt{2}$, and we can do space coarsening as well.

A refined analysis concerning the optimality can be found in Chaudet-Dumas, Gander and Pogozelskyte (2024).

For the advection–diffusion equation (2.5), we can also apply LFA to two-level STMG. Here, the discrete matrix obtained from centred finite differences is

$$A = \frac{\nu}{\Delta x^2}\,\mathrm{Tri}(1, -2, 1) + \frac{1}{2\Delta x}\,\mathrm{Tri}(-1, 0, 1).$$

Similarly to (4.38), the result when the spatial discrete operator A acts on the Fourier mode $u^l_{n+1,m}$ (with $l = j, j+1$) is

$$\begin{aligned} Au^l_{n+1,m} &= \left[\frac{2\nu(\cos(\xi\Delta x) - 1)}{\Delta x^2} + \frac{\mathrm{e}^{\mathrm{i}\xi\Delta x} - \mathrm{e}^{-\mathrm{i}\xi\Delta x}}{2\Delta x}\right] C^l_{\omega,\xi}\,\mathrm{e}^{\mathrm{i}\omega(n+1)\Delta t}\,\mathrm{e}^{\mathrm{i}\xi m\Delta x} \\ &= \left[\frac{2\nu(\cos(\xi\Delta x) - 1)}{\Delta x^2} + \frac{\mathrm{i}\sin(\xi\Delta x)}{\Delta x}\right] C^l_{\omega,\xi}\,\mathrm{e}^{\mathrm{i}\omega(n+1)\Delta t}\,\mathrm{e}^{\mathrm{i}\xi m\Delta x}. \end{aligned}$$

From this, we obtain the convergence factor ρ in Fourier space as

$$\rho(\omega, \xi, \eta) = 1 - \eta\left(1 - \frac{\mathrm{e}^{-\mathrm{i}\omega\Delta t}}{1 + \frac{2\nu\Delta t}{\Delta x^2}(1 - \cos(\xi\Delta x)) + \mathrm{i}\frac{\Delta t}{\Delta x}\sin(\xi\Delta x)}\right). \tag{4.40}$$

Heuristically, we can still use $\eta = \frac{1}{2}$ as the damping parameter for coarsening in time; see Figure 4.18. The validity of the choice $\eta = \frac{1}{2}$ for the damping parameter is further illustrated in Figure 4.19 in a numerical experiment for the two-level variant of STMG: for both the heat equation and the advection–diffusion equation

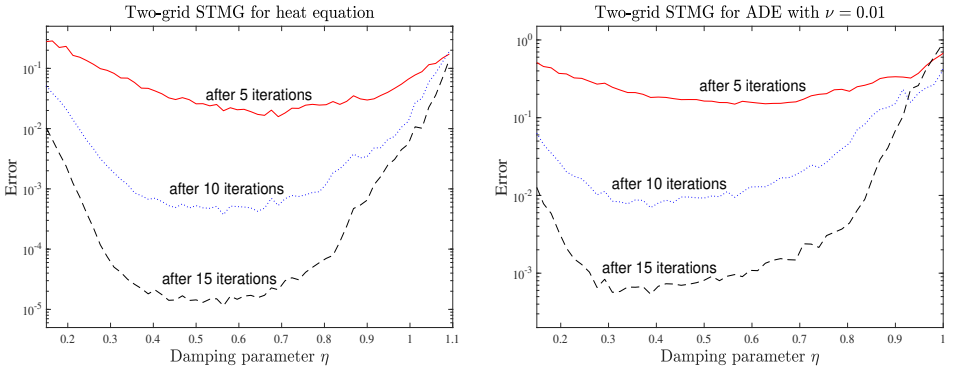

(a) (b)

Figure 4.19. Dependence of the two-level STMG error after $k = 5, 10, 15$ iterations on the choice of the damping parameter η: (a) heat equation, (b) advection–diffusion equation with $\nu = 0.01$. Here we use one block Jacobi smoothing iteration for STMG.

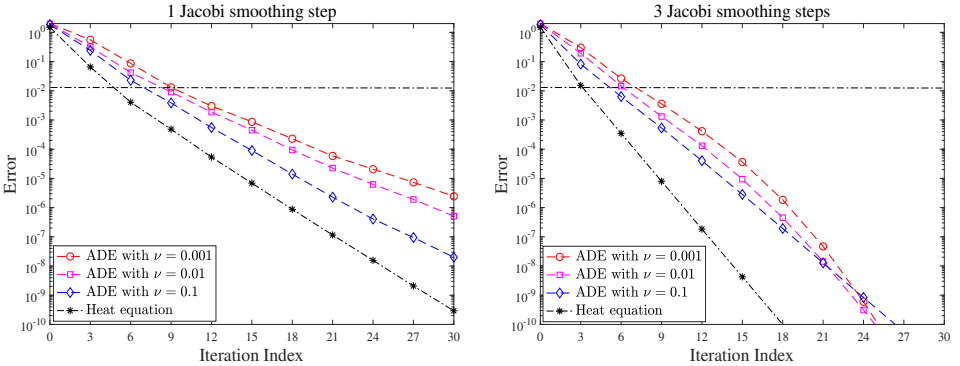

(a) (b)

Figure 4.20. Measured error of two-level STMG with one and three block Jacobi smoothing steps for the advection–diffusion equation (ADE) and the heat equation with damping parameter $\eta = \frac{1}{2}$.

(ADE), we show the errors after 5, 10 and 15 iterations for several values of η. Clearly, $\eta = \frac{1}{2}$ is a reasonable choice to minimize the error in two-level STMG for both equations.

In Figure 4.20 we show the convergence behaviour of two-level STMG for both the heat equation and the advection–diffusion equation with $\eta = \frac{1}{2}$ and three values of ν. For both equations, two-level STMG converges faster when the number of smoothing iterations is increased. Compared to the heat equation, the convergence rate is worse for the advection–diffusion equation, but interestingly it is less sensitive

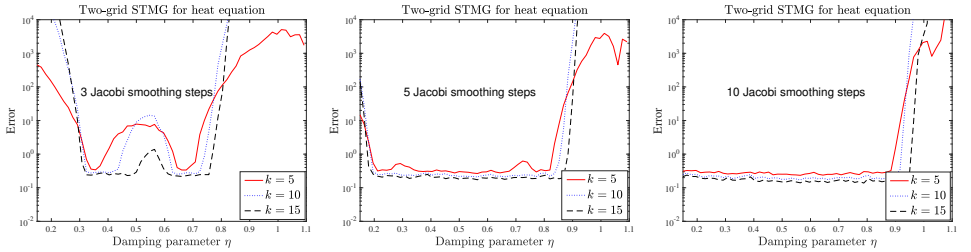

(a)

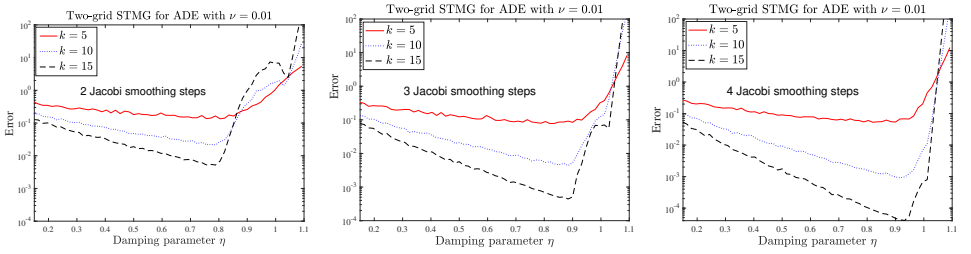

(b)

Figure 4.21. Error of STMG using the trapezoidal rule and different numbers of smoothing steps for $\eta \in [0.1, 1.1]$.

to ν when the number of smoothing iterations is large and a superlinear convergence mechanism sets in, as we see in Figure 4.20(b).

The convergence rate of STMG, however, depends on the choice of the time-integrator. The results in Figure 4.21 for two-level STMG reveal that using the trapezoidal rule as time-integrator results in a substantially poorer convergence rate compared to using backward Euler. In particular, for the heat equation, two-level STMG appears to have convergence problems regardless of the damping parameter adjustments, even with up to ten smoothing steps. Interestingly, two-level STMG converges for the advection–diffusion equation, and doing more smoothing steps enhances the convergence rate. Nonetheless, the optimal damping parameter is found to be $\eta \approx 0.8$, in contrast to $\eta = \frac{1}{2}$ we obtained for backward Euler.

In real large-scale parallel computations on today's supercomputers, excellent weak and strong scaling is achieved with the full STMG method, as shown in Table 4.1 for a three-dimensional heat equation model problem, taken from Gander and Neumüller (2016).

We next extend STMG to nonlinear problems of the form

$$\boldsymbol{u}' = f(\boldsymbol{u}), \quad \boldsymbol{u}(0) = \boldsymbol{u}_0, \quad t \in (0, T), \tag{4.41}$$

where $\boldsymbol{u} \in \mathbb{R}^{N_x}$ and $f : \mathbb{R}^{N_x} \to \mathbb{R}^{N_x}$ is defined by the discretization of a PDE in space. To describe the idea, we apply the linear-θ method to the nonlinear system

Table 4.1. Weak (left) and strong (right) scaling results of a modern space–time multigrid (STMG) method applied to a three-dimensional heat equation. Solution times of classical time-stepping with best possible parallelization in space only are also shown in the column 'Fwd. sub.'.

Cores	Time-steps	D.o.f.	Iter.	Time	Fwd. sub.	Time-steps	D.o.f.	Iter.	Time
1	2	59 768	7	28.8	19.0	512	15 300 608	7	7 635.2
2	4	119 536	7	29.8	37.9	512	15 300 608	7	3 821.7
4	8	239 072	7	29.8	75.9	512	15 300 608	7	1 909.9
8	16	478 144	7	29.9	152.2	512	15 300 608	7	954.2
16	32	956 288	7	29.9	305.4	512	15 300 608	7	477.2
32	64	1 912 576	7	29.9	613.6	512	15 300 608	7	238.9
64	128	3 825 152	7	29.9	1 220.7	512	15 300 608	7	119.5
128	256	7 650 304	7	29.9	2 448.4	512	15 300 608	7	59.7
256	512	15 300 608	7	30.0	4 882.4	512	15 300 608	7	30.0
512	1 024	30 601 216	7	29.9	9 744.2	524 288	15 667 822 592	7	15 205.9
1 024	2 048	61 202 432	7	30.0	19 636.9	524 288	15 667 822 592	7	7 651.5
2 048	4 096	122 404 864	7	29.9	38 993.1	524 288	15 667 822 592	7	3 825.3
4 096	8 192	244 809 728	7	30.0	81 219.6	524 288	15 667 822 592	7	1 913.4
8 192	16 384	489 619 456	7	30.0	162 551.0	524 288	15 667 822 592	7	956.6
16 384	32 768	979 238 912	7	30.0	313 122.0	524 288	15 667 822 592	7	478.1
32 768	65 536	1 958 477 824	7	30.0	625 686.0	524 288	15 667 822 592	7	239.3
65 536	131 072	3 916 955 648	7	30.0	1 250 210.0	524 288	15 667 822 592	7	119.6
131 072	262 144	7 833 911 296	7	30.0	2 500 350.0	524 288	15 667 822 592	7	59.8
262 144	524 288	15 667 822 592	7	30.0	4 988 060.0	524 288	15 667 822 592	7	30.0

of ODEs (4.41), leading to the all-at-once system

$$\underbrace{(B \otimes I_x)\boldsymbol{U} - \Delta t(\tilde{B} \otimes I_x) f(\boldsymbol{U})}_{:=\mathcal{K}(\boldsymbol{U})} = \boldsymbol{b}, \tag{4.42}$$

where $\boldsymbol{b} = (\boldsymbol{u}_0^\top + \Delta t(1-\theta) f^\top(\boldsymbol{u}_0), 0, \ldots, 0)^\top$, $\boldsymbol{U} = (\boldsymbol{u}_1^\top, \ldots, \boldsymbol{u}_{N_t}^\top)^\top$ and

$$B := \begin{bmatrix} 1 & & & \\ -1 & 1 & & \\ & \ddots & \ddots & \\ & & -1 & 1 \end{bmatrix}, \quad \tilde{B} := \begin{bmatrix} \theta & & & \\ 1-\theta & \theta & & \\ & \ddots & \ddots & \\ & & 1-\theta & \theta \end{bmatrix}, \quad f(\boldsymbol{U}) := \begin{bmatrix} \boldsymbol{u}_1 \\ \boldsymbol{u}_2 \\ \vdots \\ \boldsymbol{u}_{N_t} \end{bmatrix}.$$

To formulate STMG (4.42), similarly to (4.32), we first define a nonlinear block Jacobi smoother $\boldsymbol{U}^{\text{new}} = \mathcal{S}_{\text{non},\eta}(\boldsymbol{b}, \boldsymbol{U}^{\text{ini}}, s)$ by

$$\begin{cases} \tilde{\boldsymbol{U}}^0 = \boldsymbol{U}^{\text{ini}}, \\ \text{for } j = 0, 1, \ldots, s-1: \\ \quad \text{solve } \Delta\tilde{\boldsymbol{U}}^j - \Delta t\theta f(\Delta\tilde{\boldsymbol{U}}^j) = \eta(\boldsymbol{b} - \mathcal{K}(\tilde{\boldsymbol{U}}^j)), \\ \quad \tilde{\boldsymbol{U}}^{j+1} = \tilde{\boldsymbol{U}}^j + \Delta\tilde{\boldsymbol{U}}^j, \\ \boldsymbol{U}^{\text{new}} = \tilde{\boldsymbol{U}}^s, \end{cases} \tag{4.43}$$

where the correction term $\Delta\tilde{\boldsymbol{U}}^j$ is solved via an inner solver, e.g. Newton's iteration. However, we cannot obtain a theoretically optimized estimate for the damping parameter η in (4.43), since LFA cannot be used in the nonlinear case.

Following Brandt (1977), we now define a nonlinear STMG method for (4.42) using the full approximation scheme,

$$\begin{cases} \boldsymbol{U}^{k+1/3} = \mathcal{S}_{\text{non},\eta}(\boldsymbol{b}, \boldsymbol{U}^k, s_1), \\ \boldsymbol{r} = \boldsymbol{b} - \mathcal{K}\big(\boldsymbol{U}^{k+1/3}\big), \\ \boldsymbol{r}_{\text{c}} = [R_x \text{Mat}(\boldsymbol{r})] R_t^\top, \ \boldsymbol{U}_{\text{c}}^{k+1/3} = \big[R_x \text{Mat}\big(\boldsymbol{U}^{k+1/3}\big)\big] R_t^\top, \\ \text{Solve } \mathcal{K}_{\text{c}}\big(\boldsymbol{U}_{\text{c}}^{k+2/3}\big) = \boldsymbol{r}_{\text{c}} + \mathcal{K}_{\text{c}}\big(\boldsymbol{U}_{\text{c}}^{k+1/3}\big), \\ \boldsymbol{e}_{\text{c}} = \boldsymbol{U}_{\text{c}}^{k+2/3} - \boldsymbol{U}_{\text{c}}^{k+1/3}, \ \boldsymbol{e} = [P_x \text{Mat}(\boldsymbol{e}_{\text{c}})] P_t^\top, \\ \boldsymbol{U}^{k+2/3} = \boldsymbol{U}^{k+1/3} + \text{Vec}(\boldsymbol{e}), \\ \boldsymbol{U}^{k+1} = \mathcal{S}_{\text{non},\eta}\big(\boldsymbol{b}, \boldsymbol{U}^{k+2/3}, s_2\big). \end{cases} \tag{4.44}$$

In Figure 4.22 we show the measured error of this two-level STMG method for Burgers' equation (2.6) with conditions. We use two values of the diffusion parameter ν, and we see that the convergence is heavily dependent on this parameter: with enough diffusion, STMG works very well in the nonlinear setting too, whereas when the diffusion gets smaller, the convergence of STMG deteriorates, as in the linear case. Here, we used $\eta = \frac{1}{4}$ for the damping parameter, which was found to be the best choice in our numerical experiments.

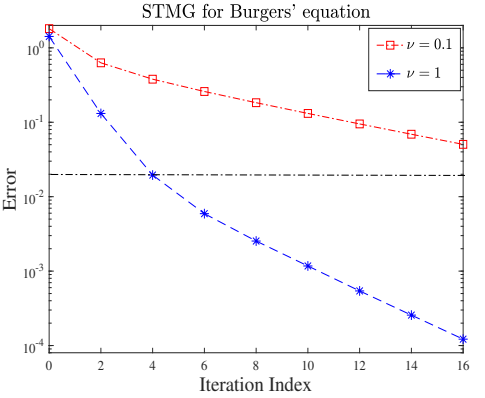

Figure 4.22. Measured error of STMG with two block Jacob smoothing steps for Burgers' equation.

For parabolic problems, STMG presented in this section stands out as by far the most effective time-parallel solver currently available, but it is intrusive in nature, unlike the Parareal algorithm. However, when dealing with hyperbolic problems, as shown in Figures 4.20 and 4.22, STMG appears to be less efficient, indicating that additional efforts are required in this domain. Furthermore, as highlighted in Figure 4.21(a), even for parabolic problems the convergence rate of STMG depends on the time-integrator used, and this dependence merits further investigation as well.

5. Conclusions

In this paper we have explained the important differences for time-parallel time integration, or PinT (parallel-in-time) methods, when applied to hyperbolic or parabolic problems. For parabolic problems, which tend to forget a lot of information in time and thus have solutions that are local in time, there are many very effective PinT techniques, such as Parareal, space–time multigrid (STMG), ParaExp and ParaDiag, and waveform relaxation (WR) techniques based on domain decomposition (DD). For hyperbolic problems, which retain very fine solution features over very long times, only some of these techniques are effective, such as ParaExp, ParaDiag and Schwarz waveform relaxation (SWR), especially in relation to tent pitching. For more information see the recent research monograph by Gander and Lunet (2024), which contains an up-to-date treatment of PinT methods, giving for each one the historical content, a simple but complete and self-contained convergence analysis, and also short MATLAB codes that can be directly executed. Codes used to produce the results in this paper are available from https://github.com/wushulin/ActaPinT.

References

X. Antoine and E. Lorin (2016), Lagrange–Schwarz waveform relaxation domain decomposition methods for linear and nonlinear quantum wave problems, *Appl. Math. Lett.* **57**, 38–45.

X. Antoine and E. Lorin (2017), An analysis of Schwarz waveform relaxation domain decomposition methods for the imaginary-time linear Schrödinger and Gross–Pitaevskii equations, *Numer. Math.* **137**, 923–958.

E. Audusse, P. Dreyfuss and B. Merlet (2010), Optimized Schwarz waveform relaxation for the primitive equations of the ocean, *SIAM J. Sci. Comput.* **32**, 2908–2936.

A. O. H. Axelsson and J. G. Verwer (1985), Boundary value techniques for initial value problems in ordinary differential equations, *Math. Comp.* **45**, 153–171.

L. Banjai and D. Peterseim (2012), Parallel multistep methods for linear evolution problems, *IMA J. Numer. Anal.* **32**, 1217–1240.

A. Bellen and M. Zennaro (1989), Parallel algorithms for initial-value problems for difference and differential equations, *J. Comput. Appl. Math.* **25**, 341–350.

D. Bennequin, M. J. Gander and L. Halpern (2009), A homographic best approximation problem with application to optimized Schwarz waveform relaxation, *Math. Comp.* **78**, 185–223.

D. Bennequin, M. J. Gander, L. Gouarin and L. Halpern (2016), Optimized Schwarz waveform relaxation for advection reaction diffusion equations in two dimensions, *Numer. Math.* **134**, 513–567.

C. Besse and F. Xing (2017), Schwarz waveform relaxation method for one-dimensional Schrödinger equation with general potential, *Numer. Algorithms* **74**, 393–426.

D. A. Bini, G. Latouche and B. Meini (2005), *Numerical Methods for Structured Markov Chains*, Oxford University Press.

M. Bjørhus (1995), On domain decomposition, subdomain iteration and waveform relaxation. PhD thesis, University of Trondheim, Norway.

K. Böhmer and H. J. Stetter (1984), *Defect Correction Methods, Theory and Applications*, Springer.

M. Bolten, D. Moser and R. Speck (2017), A multigrid perspective on the parallel full approximation scheme in space and time, *Numer. Linear Alg. Appl.* **24**, art. e2110.

M. Bolten, D. Moser and R. Speck (2018), Asymptotic convergence of the parallel full approximation scheme in space and time for linear problems, *Numer. Linear Alg. Appl.* **25**, art. e2208.

A. Bouillon, G. Samaey and K. Meerbergen (2024), Diagonalization-based preconditioners and generalized convergence bounds for ParaOpt, *SIAM J. Sci. Comput.* **46**, S317–S345.

A. Brandt (1977), Multi-level adaptive solutions to boundary-value problems, *Math. Comp.* **31**, 333–390.

L. Brugnano and D. Trigiante (2003), *Solving Differential Problems by Multistep Initial and Boundary Value Methods*, Gordon and Breach.

L. Brugnano, F. Mazzia and D. Trigiante (1993), Parallel implementation of BVM methods, *Appl. Numer. Math.* **11**, 115–124.

X.-C. Cai (1991), Additive Schwarz algorithms for parabolic convection–diffusion equations, *Numer. Math.* **60**, 41–61.

X.-C. Cai (1994), Multiplicative Schwarz methods for parabolic problems, *SIAM J. Sci. Comput.* **15**, 587–603.

R. H. Chan and M. K. Ng (1996), Conjugate gradient methods for Toeplitz systems, *SIAM Rev.* **38**, 427–482.
P. Chartier and B. Philippe (1993), A parallel shooting technique for solving dissipative ODEs, *Computing* **51**, 209–236.
B. Chaudet-Dumas, M. J. Gander and A. Pogozelskyte (2024), An optimized space–time multigrid algorithm for parabolic PDEs. Available at arXiv:2302.13881.
M. M. Chawla (1983), Unconditionally stable Noumerov-type methods for second order differential equations, *BIT* **23**, 541–542.
A. J. Christlieb, C. B. Macdonald and B. W. Ong (2010), Parallel high-order integrators, *SIAM J. Sci. Comput.* **32**, 818–835.
G. Ciaramella and M. J. Gander (2017), Analysis of the parallel Schwarz method for growing chains of fixed-sized subdomains, Part I, *SIAM J. Numer. Anal.* **55**, 1330–1356.
G. Ciaramella and M. J. Gander (2018*a*), Analysis of the parallel Schwarz method for growing chains of fixed-sized subdomains, Part II, *SIAM J. Numer. Anal.* **56**, 1498–1524.
G. Ciaramella and M. J. Gander (2018*b*), Analysis of the parallel Schwarz method for growing chains of fixed-sized subdomains, Part III, *Electron. Trans. Numer. Anal.* **49**, 201–243.
G. Ciaramella and M. J. Gander (2022), *Iterative Methods and Preconditioners for Systems of Linear Equations*, SIAM.
G. Ciaramella, M. J. Gander and I. Mazzieri (2023), Unmapped tent pitching schemes by waveform relaxation, in *Domain Decomposition Methods in Science and Engineering XXVII* (Z. Dostál *et al.*, eds), Vol. 149 of Lecture Notes in Computational Science and Engineering, Springer.
J. Cortial and C. Farhat (2009), A time-parallel implicit method for accelerating the solution of non-linear structural dynamics problems, *Internat. J. Numer. Methods Engrg* **77**, 451–470.
Y. Courvoisier and M. J. Gander (2013), Time domain Maxwell equations solved with Schwarz waveform relaxation methods, in *Domain Decomposition Methods in Science and Engineering XX* (R. Bank *et al.*, eds), Vol. 91 of Lecture Notes in Computational Science and Engineering, Springer, pp. 263–270.
F. Danieli and A. J. Wathen (2021), All-at-once solution of linear wave equations, *Numer. Linear Algebra Appl.* **28**, art. e2386.
F. Danieli, B. S. Southworth and A. J. Wathen (2022), Space–time block preconditioning for incompressible flow, *SIAM J. Sci. Comput.* **44**, A337–A363.
H. De Sterck, R. D. Falgout and O. A. Krzysik (2023*a*), Fast multigrid reduction-in-time for advection via modified semi-Lagrangian coarse-grid operators, *SIAM J. Sci. Comput.* **45**, A1890–A1916.
H. De Sterck, R. D. Falgout, S. Friedhoff, O. A. Krzysik and S. P. MacLachlan (2021), Optimizing multigrid reduction-in-time and Parareal coarse-grid operators for linear advection, *Numer. Linear Alg. Appl.* **28**, art. e2367.
H. De Sterck, R. D. Falgout, O. A. Krzysik and J. B. Schroder (2023*b*), Efficient multigrid reduction-in-time for method-of-lines discretizations of linear advection, *J. Sci. Comput.* **96**, art. 1.
P. Deuflhard (2004), *Newton Methods for Nonlinear Problems*, Springer.
V. A. Dobrev, T. V. Kolev, N. A. Petersson and J. B. Schroder (2017), Two-level convergence theory for multigrid reduction in time (MGRIT), *SIAM J. Sci. Comput.* **39**, S501–S527.

A. Dutt, L. Greengard and V. Rokhlin (2000), Spectral deferred correction methods for ordinary differential equations, *BIT* **40**, 241–266.

M. Emmett and M. L. Minion (2012), Toward an efficient parallel in time method for partial differential equations, *Commun. Appl. Math. Comput. Sci.* **7**, 105–132.

R. D. Falgout, S. Friedhoff, T. V. Kolev, S. P. MacLachlan and J. B. Schroder (2014), Parallel time integration with multigrid, *SIAM J. Sci. Comput.* **36**, C635–C661.

C. Farhat and M. Chandesris (2003), Time-decomposed parallel time-integrators: Theory and feasibility studies for fluid, structure, and fluid–structure applications, *Internat. J. Numer. Methods Engrg* **58**, 1397–1434.

C. Farhat, J. Cortial, C. Dastillung and H. Bavestrello (2006), Time-parallel implicit integrators for the near-real-time prediction of linear structural dynamic responses, *Internat. J. Numer. Methods Engrg* **67**, 697–724.

L. Fox (1954), A note on the numerical integration of first-order differential equations, *Quart. J. Mech. Appl. Math.* **7**, 367–378.

L. Fox and A. R. Mitchell (1957), Boundary-value techniques for the numerical solution of initial-value problems in ordinary differential equations, *Quart. J. Mech. Appl. Math.* **10**, 232–243.

M. J. Gander (1997), Analysis of parallel algorithms for time dependent partial differential equations. PhD thesis, Stanford University.

M. J. Gander (1999), A waveform relaxation algorithm with overlapping splitting for reaction diffusion equations, *Numer. Linear Algebra Appl.* **6**, 125–145.

M. J. Gander (2008), Schwarz methods over the course of time, *Electron. Trans. Numer. Anal.* **31**, 228–255.

M. J. Gander (2015), 50 years of time parallel time integration, in *Multiple Shooting and Time Domain Decomposition Methods* (T. Carraro *et al.*, eds), Vol. 9 of Contributions in Mathematical and Computational Sciences, Springer, pp. 69–113.

M. J. Gander (2017), Three different multigrid interpretations of the parareal algorithm and an adaptive variant, in *Workshop on Space–Time Methods for Time-Dependent Partial Differential Equations*.

M. J. Gander and S. Güttel (2013), ParaExp: A parallel integrator for linear initial-value problems, *SIAM J. Sci. Comput.* **35**, C123–C142.

M. J. Gander and E. Hairer (2008), Nonlinear convergence analysis for the parareal algorithm, in *Domain Decomposition Methods in Science and Engineering XVII* (O. B. Widlund and D. E. Keyes, eds), Vol. 60 of Lecture Notes in Computational Science and Engineering, Springer, pp. 45–56.

M. J. Gander and E. Hairer (2014), Analysis for parareal algorithms applied to Hamiltonian differential equations, *J. Comput. Appl. Math.* **259**, 2–13.

M. J. Gander and L. Halpern (2004), Absorbing boundary conditions for the wave equation and parallel computing, *Math. Comp.* **74**, 153–176.

M. J. Gander and L. Halpern (2007), Optimized Schwarz waveform relaxation methods for advection reaction diffusion problems, *SIAM J. Numer. Anal.* **45**, 666–697.

M. J. Gander and L. Halpern (2017), Time parallelization for nonlinear problems based on diagonalization, in *Domain Decomposition Methods in Science and Engineering XXIII* (C. O. Lee *et al.*, eds), Vol. 116 of Lecture Notes in Computational Science and Engineering, Springer, pp. 163–170.

M. J. Gander and T. Lunet (2020*a*), A Reynolds number dependent convergence estimate for the Parareal algorithm, in *Domain Decomposition Methods in Science and Engineering XXV* (R. Haynes *et al.*, eds), Vol. 138 of Lecture Notes in Computational Science and Engineering, Springer, pp. 277–284.
M. J. Gander and T. Lunet (2020*b*), Toward error estimates for general space–time discretizations of the advection equation, *J. Comput. Vis. Sci.* **23**, 1–14.
M. J. Gander and T. Lunet (2024), *Time Parallel Time Integration*, SIAM.
M. J. Gander and M. Neumüller (2016), Analysis of a new space–time parallel multigrid algorithm for parabolic problems, *SIAM J. Sci. Comput.* **38**, A2173–A2208.
M. J. Gander and D. Palitta (2024), A new ParaDiag time-parallel time integration method, *SIAM J. Sci. Comput.* **46**, A697–A718.
M. J. Gander and C. Rohde (2005), Overlapping Schwarz waveform relaxation for convection-dominated nonlinear conservation laws, *SIAM J. Sci. Comput.* **27**, 415–439.
M. J. Gander and A. M. Stuart (1998), Space–time continuous analysis of waveform relaxation for the heat equation, *SIAM J. Sci. Comput.* **19**, 2014–2031.
M. J. Gander and S. Vandewalle (2007), Analysis of the parareal time-parallel time-integration method, *SIAM J. Sci. Comput.* **29**, 556–578.
M. J. Gander and S.-L. Wu (2019), Convergence analysis of a periodic-like waveform relaxation method for initial-value problems via the diagonalization technique, *Numer. Math.* **143**, 489–527.
M. J. Gander and S.-L. Wu (2020), A diagonalization-based parareal algorithm for dissipative and wave propagation problems, *SIAM J. Numer. Anal.* **58**, 2981–3009.
M. J. Gander, S. Güttel and M. Petcu (2018*a*), A nonlinear ParaExp algorithm, in *Domain Decomposition Methods in Science and Engineering XXIV* (P. Bjørstad *et al.*, eds), Vol. 125 of Lecture Notes in Computational Science and Engineering, Springer, pp. 261–270.
M. J. Gander, L. Halpern and F. Nataf (1999), Optimal convergence for overlapping and non-overlapping Schwarz waveform relaxation, in *Eleventh International Conference of Domain Decomposition Methods* (C.-H. Lai *et al.*, eds), ddm.org.
M. J. Gander, L. Halpern and F. Nataf (2003), Optimal Schwarz waveform relaxation for the one dimensional wave equation, *SIAM J. Numer. Anal.* **41**, 1643–1681.
M. J. Gander, L. Halpern, F. Hubert and S. Krell (2020), Optimized Schwarz methods with general Ventcell transmission conditions for anisotropic diffusion with discrete duality finite volume discretizations, *Moroccan J. Pure Appl. Anal.* **7**, 182–213.
M. J. Gander, L. Halpern, F. Hubert and S. Krell (2021*a*), Discrete optimization of Robin transmission conditions for anisotropic diffusion with discrete duality finite volume methods, *Vietnam J. Math.* **49**, 1349–1378.
M. J. Gander, L. Halpern, J. Rannou and J. Ryan (2019), A direct time parallel solver by diagonalization for the wave equation, *SIAM J. Sci. Comput.* **41**, A220–A245.
M. J. Gander, L. Halpern, J. Ryan and T. T. B. Tran (2016*a*), A direct solver for time parallelization, in *Domain Decomposition Methods in Science and Engineering XXII* (T. Dickopf *et al.*, eds), Vol. 104 of Lecture Notes in Computational Science and Engineering, Springer, pp. 491–499.
M. J. Gander, F. Kwok and B. Mandal (2016*b*), Dirichlet–Neumann and Neumann–Neumann waveform relaxation algorithms for parabolic problems, *ETNA* **45**, 424–456.
M. J. Gander, F. Kwok and B. C. Mandal (2021*b*), Dirichlet–Neumann waveform relaxation methods for parabolic and hyperbolic problems in multiple subdomains, *BIT Numer. Math.* **61**, 173–207.

M. J. Gander, F. Kwok and H. Zhang (2018*b*), Multigrid interpretations of the parareal algorithm leading to an overlapping variant and MGRIT, *J. Comput. Vis. Sci.* **19**, 59–74.
M. J. Gander, J. Liu, S.-L. Wu, X. Yue and T. Zhou (2021*c*), ParaDiag: Parallel-in-time algorithms based on the diagonalization technique. Available at arXiv:2005.09158.
M. J. Gander, T. Lunet and A. Pogoželskytė (2023*a*), Convergence of Parareal for a vibrating string with viscoelastic damping, in *Domain Decomposition Methods in Science and Engineering XXVI* (S. C. Brenner *et al.*, eds), Vol. 145 of Lecture Notes in Computational Science and Engineering, Springer, pp. 435–442.
M. J. Gander, T. Lunet, D. Ruprecht and R. Speck (2023*b*), A unified analysis framework for iterative parallel-in-time algorithms, *SIAM J. Sci. Comput.* **45**, A2275–A2303.
M. J. Gander, S. B. Lunowa and C. Rohde (2023*c*), Non-overlapping Schwarz waveform-relaxation for nonlinear advection–diffusion equations, *SIAM J. Sci. Comput.* **45**, A49–A73.
M. J. Gander, M. Ohlberger and S. Rave (2024), A Parareal algorithm without coarse propagator? Available at arXiv:2409.02673.
E. Giladi and H. B. Keller (2002), Space–time domain decomposition for parabolic problems, *Numer. Math.* **93**, 279–313.
J. Gopalakrishnan, M. Hochsteger, J. Schöberl and C. Wintersteiger (2020), An explicit mapped tent pitching scheme for Maxwell equations, in *Spectral and High Order Methods for Partial Differential Equations (ICOSAHOM 2018)*, pp. 359–369.
J. Gopalakrishnan, J. Schöberl and C. Wintersteiger (2017), Mapped tent pitching schemes for hyperbolic systems, *SIAM J. Sci. Comput.* **39**, B1043–B1063.
X. M. Gu and S.-L. Wu (2020), A parallel-in-time iterative algorithm for Volterra partial integro-differential problems with weakly singular kernel, *J. Comput. Phys.* **417**, art. 109576.
D. Guibert and D. Tromeur-Dervout (2007), Parallel deferred correction method for CFD problems, in *Parallel Computational Fluid Dynamics 2006*, Elsevier, pp. 131–138.
W. Hackbusch (1984), Parabolic multi-grid methods, in *Computing Methods in Applied Sciences and Engineering VI* (R. Glowinski and J.-L. Lions, eds), North-Holland, pp. 189–197.
L. Halpern and J. Szeftel (2010), Optimized and quasi-optimal Schwarz waveform relaxation for the one-dimensional Schrödinger equation, *Math. Models Methods Appl. Sci.* **20**, 2167–2199.
B. Heinzelreiter and J. W. Pearson (2024), Diagonalization-based parallel-in-time preconditioners for instationary fluid flow control problems. Available at arXiv:2405.18964.
A. Hessenthaler, B. S. Southworth, D. Nordsletten, O. Röhrle, R. D. Falgout and J. B. Schroder (2020), Multilevel convergence analysis of multigrid-reduction-in-time, *SIAM J. Sci. Comput.* **42**, A771–A796.
N. J. Higham (2008), *Functions of Matrices: Theory and Computation*, SIAM.
G. Horton and S. Vandewalle (1995), A space–time multigrid method for parabolic partial differential equations, *SIAM J. Sci. Comput.* **16**, 848–864.
G. Horton, S. Vandewalle and P. Worley (1995), An algorithm with polylog parallel complexity for solving parabolic partial differential equations, *SIAM J. Sci. Comput.* **16**, 531–541.
A. J. Howse, H. D. Sterck, R. D. Falgout, S. MacLachlan and J. Schroder (2019), Parallel-in-time multigrid with adaptive spatial coarsening for the linear advection and inviscid Burgers equations, *SIAM J. Sci. Comput.* **41**, A538–A565.

J. Janssen and S. Vandewalle (1996), Multigrid waveform relaxation of spatial finite element meshes: The continuous-time case, *SIAM J. Numer. Anal.* **33**, 456–474.
G. L. Kooij, M. A. Botchev and B. J. Geurts (2017), A block Krylov subspace implementation of the time-parallel ParaExp method and its extension for nonlinear partial differential equations, *J. Comput. Appl. Math.* **316**, 229–246.
D. Kressner, S. Massei and J. Zhu (2023), Improved ParaDiag via low-rank updates and interpolation, *Numer. Math.* **155**, 175–209.
E. Lelarasmee, A. E. Ruehli and A. L. Sangiovanni-Vincentelli (1982), The waveform relaxation method for time-domain analysis of large scale integrated circuits, *IEEE Trans. CAD IC Syst.* **1**, 131–145.
X. L. Lin and M. Ng (2021), An all-at-once preconditioner for evolutionary partial differential equations, *SIAM J. Sci. Comput.* **43**, A2766–A2784.
J.-L. Lions, Y. Maday and G. Turinici (2001), A Parareal in time discretization of PDEs, *C.R. Acad. Sci. Paris, Ser. I* **332**, 661–668.
J. Liu and S.-L. Wu (2020), A fast block α-circulant preconditoner for all-at-once systems from wave equations, *SIAM J. Matrix Anal. Appl.* **41**, 1912–1943.
J. Liu and S.-L. Wu (2022), Parallel-in-time preconditioner for the Sinc-Nyström systems, *SIAM J. Sci. Comput.* **44**, A2386–A2411.
J. Liu, X.-S. Wang, S.-L. Wu and T. Zhou (2022), A well-conditioned direct PinT algorithm for first-and second-order evolutionary equations, *Adv. Comput. Math.* **48**, art. 16.
C. Lubich and A. Ostermann (1987), Multi-grid dynamic iteration for parabolic equations, *BIT* **27**, 216–234.
Y. Maday and O. Mula (2020), An adaptive parareal algorithm, *J. Comput. Appl. Math.* **377**, art. 112915.
Y. Maday and E. M. Rønquist (2008), Parallelization in time through tensor-product space–time solvers, *C.R. Math. Acad. Sci. Paris* **346**, 113–118.
V. Martin (2009), Schwarz waveform relaxation algorithms for the linear viscous equatorial shallow water equations, *SIAM J. Sci. Comput.* **31**, 3595–3625.
T. P. Mathew, M. Sarkis and C. E. Schaerer (2010), Analysis of block parareal preconditioners for parabolic optimal control problems, *SIAM J. Sci. Comput.* **32**, 1180–1200.
E. McDonald, J. Pestana and A. Wathen (2018), Preconditioning and iterative solution of all-at-once systems for evolutionary partial differential equations, *SIAM J. Sci. Comput.* **40**, A1012–A1033.
M. Merkel, I. Niyonzima and S. Schöps (2017), ParaExp using leapfrog as integrator for high-frequency electromagnetic simulations, *Radio Sci.* **52**, 1558–1569.
G. A. Meurant (1991), Numerical experiments with a domain decomposition method for parabolic problems on parallel computers, in *Proceedings of the Fourth International Symposium on Domain Decomposition Methods for Partial Differential Equations*, SIAM, pp. 394–408.
M. Minion (2011), A hybrid parareal spectral deferred corrections method, *Commun. Appl. Math. Comput. Sci.* **5**, 265–301.
M. L. Minion (2010), A hybrid parareal spectral deferred corrections method, *Commun. Appl. Math. Comput. Sci.* **5**, 265–301.
M. L. Minion, R. Speck, M. Bolten, M. Emmett and D. Ruprecht (2015), Interweaving PFASST and parallel multigrid, *SIAM J. Sci. Comput.* **37**, S244–S263.
W. L. Miranker and W. Liniger (1967), Parallel methods for the numerical integration of ordinary differential equations, *Math. Comp.* **91**, 303–320.

C. Moler and C. Van Loan (2003), Nineteen dubious ways to compute the exponential of a matrix, twenty-five years later, *SIAM Rev.* **45**, 3–49.
M. Neumüller and I. Smears (2019), Time-parallel iterative solvers for parabolic evolution equations, *SIAM J. Sci. Comput.* **41**, C28–C51.
O. Nevanlinna (1989), Remarks on Picard–Lindelöf iteration, Part I, *BIT* **29**, 328–346.
M. K. Ng (2004), *Iterative Methods for Toeplitz Systems*, Oxford Academic.
J. Nievergelt (1964), Parallel methods for integrating ordinary differential equations, *Commun. Assoc. Comput. Mach.* **7**, 731–733.
B. W. Ong and J. B. Schröder (2020), Applications of time parallelization, *J. Comput. Vis. Sci.* **23**, 1–15.
J. M. Ortega and W. C. Rheinboldt (2000), *Iterative Solution of Nonlinear Equations in Several Variables*, SIAM.
J. W. Pearson, M. Stoll and A. J. Wathen (2012), Regularization-robust preconditioners for time-dependent PDE-constrained optimization problems, *SIAM J. Matrix Anal. Appl.* **33**, 1126–1152.
P. Saha, J. Stadel and S. Tremaine (1997), A parallel integration method for solar system dynamics, *Astronom. J.* **114**, 409–415.
M. Schreiber, P. S. Peixoto, T. Haut and B. Wingate (2018), Beyond spatial scalability limitations with a massively parallel method for linear oscillatory problems, *Internat. J. High Performance Comput. Appl.* **32**, 913–933.
H. Schwarz (1870), Über einen Grenzübergang durch alternierendes Verfahren, *Vierteljahrsschrift der Naturforschenden Gesellschaft in Zürich* **15**, 272–286.
J. Simoens and S. Vandewalle (2000), Waveform relaxation with fast direct methods as preconditioner, *SIAM J. Sci. Comput.* **21**, 1755–1773.
R. Speck, D. Ruprecht, M. Emmett, M. Bolten and R. Krause (2014), A space–time parallel solver for the three-dimensional heat equation, in *Parallel Computing: Accelerating Computational Science and Engineering (CSE)*, Vol. 25 of Advances in Parallel Computing, IOS Press, pp. 263–272.
R. Speck, D. Ruprecht, R. Krause, M. Emmett, M. Minion, M. Winkel and P. Gibbon (2012), A massively space–time parallel N-body solver, in *SC'12: Proceedings of the International Conference on High Performance Computing, Networking, Storage and Analysis*, IEEE Computer Society Press, pp. 1–11.
G. Strang (1986), A proposal for Toeplitz matrix calculations, *Stud. Appl. Math.* **74**, 171–176.
S. Thery, C. Pelletier, F. Lemarié and E. Blayo (2022), Analysis of Schwarz waveform relaxation for the coupled Ekman boundary layer problem with continuously variable coefficients, *Numer. Algorithms* **89**, 1145–1181.
J. Van Lent and S. Vandewalle (2002), Multigrid waveform relaxation for anisotropic partial differential equations, *Numer. Algorithms* **31**, 361–380.
F. Van Loan, C and N. Pitsianis (1993), Approximation with Kronecker products, in *Linear Algebra for Large Scale and Real-Time Applications* (M. S. Moonen *et al.*, eds), Vol. 232 of NATO ASI Series, Springer, pp. 293–314.
S. Vandewalle and E. Van de Velde (1994), Space–time concurrent multigrid waveform relaxation, *Ann. Numer. Math* **1**, 347–363.
D. E. Womble (1990), A time-stepping algorithm for parallel computers, *SIAM J. Sci. Statist. Comput.* **11**, 824–837.

P. Worley (1991), Parallelizing across time when solving time-dependent partial differential equations, in *Proceedings of the Fifth SIAM Conference on Parallel Processing for Scientific Computing* (D. Sorensen, ed.), SIAM, pp. 246–252.

S.-L. Wu (2015), Convergence analysis of some second-order parareal algorithms, *IMA J. Numer. Anal.* **35**, 1315–1341.

S.-L. Wu (2017), Optimized overlapping Schwarz waveform relaxation for a class of time-fractional diffusion problems, *J. Sci. Comput.* **72**, 842–862.

S.-L. Wu (2018), Toward parallel coarse grid correction for the parareal algorithm, *SIAM J. Sci. Comput.* **40**, A1446–A1472.

S.-L. Wu and M. D. Al-Khaleel (2014), Semi-discrete Schwarz waveform relaxation algorithms for reaction diffusion equations, *BIT* **54**, 831–866.

S.-L. Wu and J. Liu (2020), A parallel-in-time block-circulant preconditioner for optimal control of wave equations, *SIAM J. Sci. Comput.* **42**, A1510–A1540.

S.-L. Wu and Y. Xu (2017), Convergence analysis of Schwarz waveform relaxation with convolution transmission conditions, *SIAM J. Sci. Comput.* **39**, A890–A921.

S.-L. Wu and T. Zhou (2015), Convergence analysis for three parareal solvers, *SIAM J. Sci. Comput.* **37**, A970–A992.

S.-L. Wu and T. Zhou (2019), Acceleration of the two-level MGRIT algorithm via the diagonalization technique, *SIAM J. Sci. Comput.* **41**, A3421–A3448.

S.-L. Wu and T. Zhou (2021*a*), Parallel implementation for the two-stage SDIRK methods via diagonalization, *J. Comput. Phys.* **428**, art. 110076.

S.-L. Wu and T. Zhou (2024), Convergence analysis of the parareal algorithm with non-uniform fine time grid, *SIAM J. Numer. Anal.* **62**, 2308–2330.

S.-L. Wu, C. M. Huang and T. Z. Huang (2012), Convergence analysis of the overlapping Schwarz waveform relaxation algorithm for reaction–diffusion equations with time delay, *IMA J. Numer. Anal.* **32**, 632–671.

S.-L. Wu, Z. Wang and T. Zhou (2023), PinT preconditioner for forward–backward evolutionary equations, *SIAM J. Matrix Anal. Appl.* **44**, 1771–1798.

S.-L. Wu, Z. H. Yang and T. Zhou (2025), Mixed precision iterative ParaDiag algorithm. Submitted.

S.-L. Wu, T. Zhou and Z. Zhou (2022), A uniform spectral analysis for a preconditioned all-at-once system from first-order and second-order evolutionary problems, *SIAM J. Matrix Anal. Appl.* **43**, 1331–1353.

S. N. Wu and Z. Zhou (2021*b*), A parallel-in-time algorithm for high-order BDF methods for diffusion and subdiffusion equations, *SIAM J. Sci. Comput.* **43**, A3627–A3656.

J. Yang, Z. M. Yuan and Z. Zhou (2023), Robust convergence of parareal algorithms with arbitrarily high-order fine propagators, *CSIAM Trans. Appl. Math.* **4**, 566–591.